Carbon dioxide removal and environmental impacts from the suspended sediment fraction of a mineral-based ocean alkalinity enhancement field trial

Chloe Leach[1], Jaclyn E.P. Cetiner[1*], Emilia Jankowska[1], Devon B. Cole[1], Thi Tran[1], Hailey Hayes[1], Cheyenne Moreau[1], M. Grace Andrews[1]

[1] Hourglass Climate, NGO, Montclair NJ, USA

Jaclyn E.P. Cetiner* jaclyn@hourglassclimate.org

Keywords: Ocean alkalinity enhancement, carbon dioxide removal, marine enhanced rock weathering, olivine, suspended sediment

Number of words: 11,649

Number of tables: 1

Number of figures: 7

Abstract

Mineral-based ocean alkalinity enhancement (OAE) is a promising marine carbon dioxide removal (mCDR) strategy whose efficacy and environmental impact depend strongly on whether feedstock is retained on the seafloor or transported in suspension. We investigated the suspended sediment fraction from the world's first nearshore field trial of mineral-based OAE, in which 9,645 tonnes of olivine-rich dunite rock was deployed off Duck, North Carolina, USA, in May–June 2024. ~25% of the feedstock (2,379 tonnes) entered suspension, with the remainder retained in nearshore berms. Combining placement-day monitoring with longer-term observations through April 2025, we quantified sedimentological, chemical, and biological responses: turbidity plumes were short-lived and localized, and olivine-associated trace metals (Ni, Co) rose transiently during placement but stayed well below EPA thresholds, with no other significant water quality or ecological effects detected. A coupled sediment transport–geochemical model, informed by field data, shows that elevated water column Ni and Co concentrations, relative to model predictions, indicate olivine dissolution rates higher than canonical values immediately post-placement. Sensitivity analysis shows hydrodynamic transport uncertainty outweighs geochemical conditions (temperature, pH) in controlling the suspended fraction's long-term CDR potential. Under representative site conditions, the suspended fraction is projected to remove 516 tonnes gross CO_2 within 20 years and 1,788 tonnes over its full 173-year dissolution lifetime. These findings show suspended feedstock is a quantitatively significant reservoir that must be explicitly tracked in mineral-based OAE deployments.

1. Introduction

Limiting global warming to within 2°C by 2100 will require large-scale carbon dioxide removal (CDR) (NASEM, 2019). Marine CDR (mCDR) shows significant promise given the ocean's capacity for long-term carbon storage (NASEM, 2022). One proposed approach, mineral-based Ocean Alkalinity Enhancement (OAE), adds alkaline minerals (e.g. olivine, brucite and lime) to seawater to dissolve and generate stable bicarbonate and carbonate ions, in turn enhancing the ocean's capacity to uptake atmospheric CO_2 while potentially mitigating ocean acidification locally (Kheshgi, 1995). Mineral-based OAE has gained growing attention as a scalable mCDR strategy (NASEM, 2022; Montserrat et al., 2017; Meysman and Montserrat, 2017) with olivine showing particular promise due to its rapid intrinsic weathering rate, abundance and high CO_2 uptake potential (Feng et al. 2017, Palmieri and Yool, 2024; Geerts et al. 2025). However, the real-world efficiency and environmental impacts of this CDR approach remain poorly constrained due to limited field studies.

Uncertainties in the efficiency and environmental impacts of mineral-based OAE are strongly linked to the transport fate of feedstock in natural environments, which controls the geochemical conditions under which mineral dissolution occurs, and therefore influences both dissolution behavior and environmental impacts. Transport fate reflects a balance between hydrodynamic transport processes, which dictate the mode and distance of particle transport, and the rate of mineral dissolution, such that particles may dissolve in-situ or be transported into different environments before complete dissolution. For olivine, dissolution timescale depends on factors such as grain size, temperature, and pH, with sand-sized particles typically requiring years to centuries to fully dissolve (Ramasamy et al., 2024). During this time, particles may be transported as suspended material (including washload, where a fraction of material remains in persistent suspension under given hydrodynamic conditions) or as bedload (particles transported along the seabed), or accumulate in sediments; this results in highly site- and time-dependent transport behavior. Grains may transition between transport modes as hydrodynamic conditions and particle properties change. If suspended in the water column, feedstock can be rapidly advected away from the release site by ambient currents, making its fate considerably more difficult to constrain than material on the seafloor, which generally exhibits slower transport rates (van Rijn, 1984b).

Carbon removal potential and environmental impacts depend strongly on whether feedstock resides in the water column or sediments, which represent distinct transport and geochemical regimes. Grains in the sediment column may dissolve faster due to lower porewater pH (often >0.3 pH units less than water column pH (e.g., Middelburg, Soetaert, Hagens, 2020)), and physical grinding due to seafloor sediment transport, but can also experience reduced CDR efficiency through burial or secondary mineral precipitation under low water:rock ratios (Geerts et al., 2025), and may be subject to the 'additionality problem' in which natural alkalinity generation is reduced as a function of an OAE deployment, thereby reducing the net impact of the OAE intervention (Bach, 2024). In contrast, suspended particles interact with continuously refreshed seawater and so may avoid such efficiency losses. However, carbon removal efficiency from suspended particles can be reduced if particles are transported into different environments (e.g., colder waters) as this can affect their dissolution rate. .

In addition to influencing CDR efficiency, feedstock transport and dissolution have important environmental implications. Particle release during OAE may elevate suspended sediment concentrations and turbidity, generating sediment plumes similar to those observed during beach nourishment (Warrick et al., 2025; Glueck and Schubert, 2024) and sediment disposal projects (Morris et

al., 2024). Such plumes have the potential to reduce light penetration and alter primary production. However, observations from coastal infrastructure projects suggest that increases in suspended sediment concentrations and turbidity are often short-lived (hours), localized (Morris et al., 2024; Van Dolah et al., 1994), and often remain within natural variability of the system (Roman-Sierra et al., 2011). Longer-lasting effects have occasionally been reported (Balch, 2009; Glueck and Schubert, 2024), with plume magnitude and persistence depending on hydrodynamics, feedstock volume, grain size distribution and background turbidity (Roman-Sierra et al., 2011, Balch, 2009; Glueck and Schubert, 2024). Beyond these physical effects, olivine dissolution releases alkalinity, silicic acid, iron, and trace metals that may influence phytoplankton growth and nutrient cycling (Hauck et al., 2016; Bach et al., 2019). Because silicic acid is an essential nutrient for diatoms (Tréguer and De La Rocha, 2013), olivine dissolution has the potential to stimulate diatom productivity and influence the biological carbon pump, although experimental studies report mixed responses ranging from enhanced growth to negligible ecosystem effects (Hutchins et al., 2023; Guo et al., 2024, Ferderer et al., 2024). Large-scale deployments could also increase concentrations of potentially toxic metals such as Ni, Cr, and Co, as well as drive longer-term sediment-water chemical changes, highlighting the importance of monitoring carbonate chemistry, nutrients, turbidity, and trace metals during OAE field trials (e.g. Bach et al., 2019).

Here, we investigate the suspended sediment fraction generated during the world's first nearshore application of mineral-based OAE. Specifically, we quantify the fraction of feedstock in suspension, assess suspended sediment dynamics during placement (~hours) and over the longer-term from March 2024 to April 2025, and evaluate associated changes in water-column chemistry and environmental impacts at, and adjacent to, the project site. To mechanistically interpret field observations and estimate alkalinity generation and carbon removal, we combine field measurements with a coupled sediment transport and geochemical model. Finally, we discuss the implications of our findings for the scalability, environmental safety, and Measurement, Reporting and Verification (MRV) of mineral-based OAE strategies.

2. Materials and Methods

2.1. Project Overview

In May and June 2024, Vesta PBC executed a mineral-based OAE field trial off the coast of Duck, North Carolina, USA (Figure 1), where 9645 tonnes of dunite sand was deposited. The bulk feedstock (hereafter “feedstock”) had a median grain size (D_{50}) of 163 µm and 8.28 wt% fines (<62.5 µm), and contained 88.6 wt% forsterite, 3.2 wt% orthopyroxene, 3.0 wt% chlorite, and 2.3 wt% talc, with minor contributions of 2:1 layer silicates, spinels, and periclase. XRD analysis of specific grain size fractions of the feedstock shows that the 0-45 µm fraction was distinct from the bulk composition, containing only 56.1 wt% forsterite with 20.9 wt% serpentine, 12.9 wt% 2:1 layer silicates, and 6.3 wt% chlorite. Throughout this manuscript, "feedstock" refers to the bulk material, while "olivine" refers specifically to its forsteritic olivine component of the feedstock. Native sediments at the project site were slightly coarser than the feedstock (D_{50}: 200 µm) and quartz-dominated (70.2-81.3 wt%). Detailed mineralogical, elemental and grain size data are provided in the Supplementary Material.

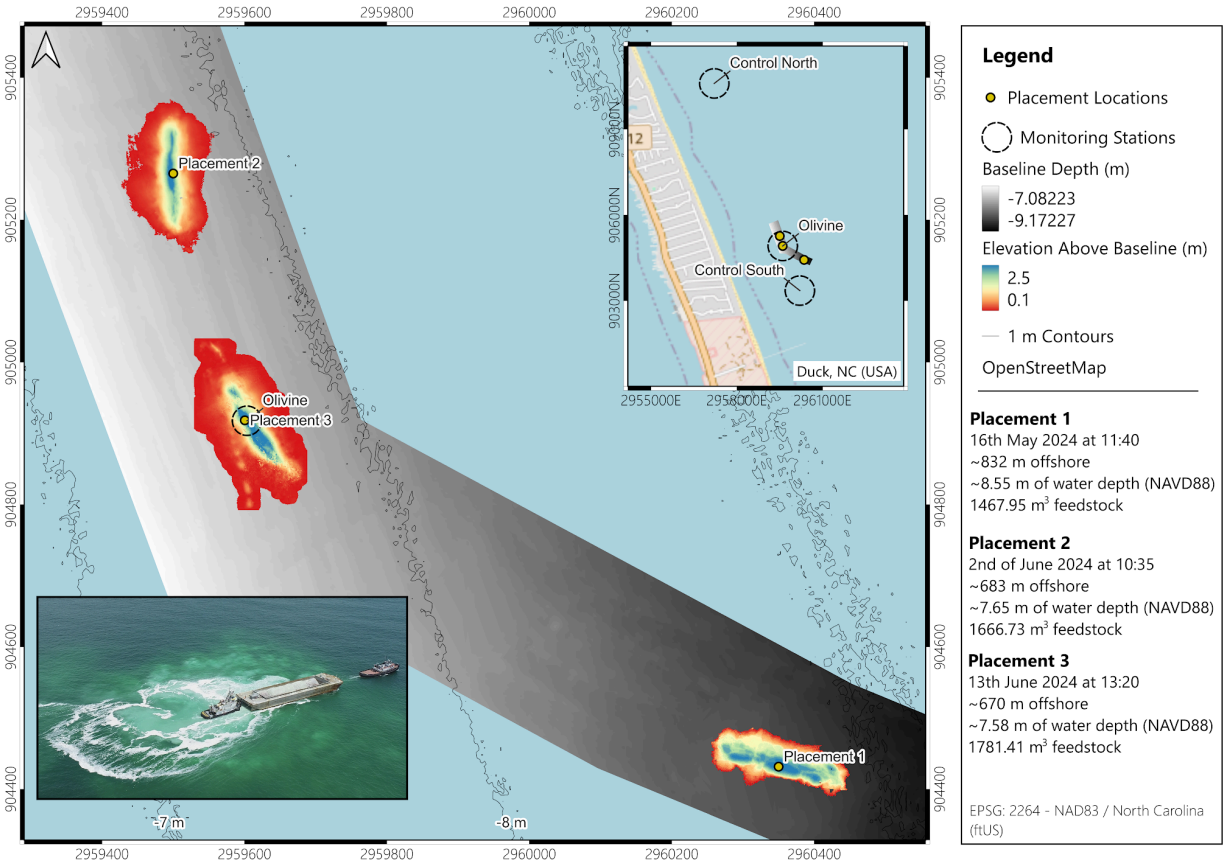


Figure 1. Field trial location and initial bathymetry following feedstock placement. Colored surfaces show the profile of each placement, baseline bathymetry is shown in greyscale. Inset: Aerial drone imagery showing the feedstock deployment and resulting turbidity plume, recorded during Placement 3 (+8 minutes). Photo Credit: Sean Charles and Hannah Sirianni

The feedstock was deployed as 3 nearshore berms across 3 days using a towed dump scow at depths of ~7.6–8.6 m (NAVD88) (Figure 1). The term “deployment” is used to refer to the entire project, and “placement” for individual berms. The volume of sediment released during each placement was calculated by Vesta’s coastal engineering contractor based on the reduction in drone-derived stockpile volume after loading each barge. During placements, material partitioned between washload, suspended load and bedload. Sediment-laden seasurface foam was also observed, which provided an additional vehicle for suspended sediment transport.

The project includes a multi-year monitoring program focused on carbon removal efficacy and environmental impacts at the deployment site and in the surrounding area. Here we present first-year results focused primarily on the water column. Baseline (“pre-deployment”) monitoring was conducted from March to May 2024, measurements were also collected immediately before (“pre-placement”) and after (“post-placement”) each berm placement, and post-deployment monitoring continued approximately monthly thereafter, with results through April 2025 reported here. Data analysis was divided into short-term responses capturing placement events and the long-term response spanning March 2024 to April 2025, excluding placement days. The experimental design for long-term monitoring included three stations: an Olivine station and two Control stations (Control North, Control South) (Figure 1; Supplementary Material).

2.2. Field Methods

2.2.1. Bathymetric Surveys

Multibeam bathymetric surveys were conducted pre- and post-placement to capture the location and extent of the nearshore berms. Survey lines were spaced 25 m apart, designed to ensure optimal swath overlap for full seafloor coverage. Data was collected using a Norbit 400 kHZ multibeam system; an all-in-one tightly integrated broadband multibeam system coupled with an Applanix WaveMaster inertial navigation system embedded into the unit. The multibeam data were processed using Qimera - QPS software, which adjusts for vessel motion (heading, heave, pitch, roll), sound velocity, and RTK GPS vertical corrections. A 0.50 m continuous grid was derived from the soundings with a vertical uncertainty of $\pm$ 10 cm, with depths relative to the North American Vertical Datum 1988 (NAVD88) via Geoid12B CONUS (USA).

2.2.2. Wave and Current Measurements

Wave and current measurements were sourced from U.S. Army Corps of Engineers (USACE) Field Research Facility (FRF) devices deployed off the Town of Duck, NC. Near real-time wave conditions were recorded by a Waverider buoy located approximately 3.7 km offshore in -17.8 m of water (Station ID: 44056). Observations were recorded at 30 minute intervals. Depth-averaged current speeds and directions were derived from a bottom mounted Nortek Signature1000 Acoustic Doppler Current Profiler (ADCP) located approximately 600 m offshore at a nominal depth of -6.7 m.

2.2.3. Sediment Cores

Sediment cores were collected at the Olivine station (Figure 1) on 12 March 2024 and 30 April 2024 (pre-deployment) and 8 July 2024 (post-deployment) to characterize native and post-deployment sediment properties respectively. Cores were sub-sampled using an incremental sediment core extruder and the upper 1-3 cm fraction was analyzed for this study. See Supplementary Material for sediment sample locations.

2.2.4. Water Quality

2.2.4.1. Short-Term Observations

A vertical array of 3 YSI EXO2 Sondes (the “fixed sonde array”) was installed prior to each placement at the target coordinate, recovered and re-installed on top of the berms after placement. The fixed sonde array was re-installed 170 minutes after Placement 1, 23 minutes after Placement 2, and 18 minutes after Placement 3. Data were collected continuously at 5 second intervals, including depth below surface (m) and turbidity (NTU; accuracy: ±2% of reading or ±0.3 NTU, whichever is greater; precision: ±0.01 NTU). It was tethered to a floating buoy, recording data below the water surface, in the mid-water column and on the seafloor; the exact depths varied for each placement and were also influenced by the presence of the berms (Supplementary Material). An AquaTROLL 500 sonde (the “mobile sonde”) was deployed from a monitoring vessel that followed the pathways of the suspended sediment plume generated during each placement. Measured parameters included turbidity, pH, dissolved oxygen, chlorophyll-a fluorescence, salinity, temperature, and conductivity; corresponding units, precision, and accuracy specifications are reported in Supplementary Material, as well as the sampling locations.

Discrete water column samples were collected intermittently at the surface and bottom of the water column. At 4-8 locations during each placement, 5 L of water were collected with Niskin bottles and filtered for discrete water column parameters: dissolved oxygen, salinity, trace metals, major cations, nutrients, pH, total alkalinity (TA), and Dissolved Inorganic Carbon (DIC). At 32-36 locations, 2 L of water were collected with Van Dorn samplers to measure Total Suspended Sediment (TSS) concentrations. At 8 locations, 5 L of water was collected for grain size and mineralogical analysis. Seasurface foam samples

were collected in Niskin bottles or HDPE jars. See Supplementary Material for water column sample locations.

2.2.4.2. Long-Term Observations

Mobile sonde surveys were conducted at and between the Olivine and Control stations (Figure 1), 1-3 times monthly, capturing 3-26 water quality snapshots primarily from bottom water (~1 m above seafloor). Water quality parameters (including depth, pressure, turbidity, pH, dissolved oxygen, chlorophyll-*a* fluorescence, salinity, and temperature; see Supplementary Material), were measured with an AquaTROLL 500 sonde (2024) or YSI EXO2 sonde (2025). The term "mobile sonde" is used to represent both instruments unless otherwise specified. In addition, discrete bottom water samples were collected with 5 L Niskin bottles at the Olivine and Control stations (Figure 1) at an approximately monthly cadence, and analyzed for salinity, pH, DIC, TA, trace metals, major cations, and nutrients.

2.3. Laboratory Methods

2.3.1. Bulk Sediment Samples

Sediment core samples were dried at 60°C and analyzed for mineralogy by x-ray diffraction (XRD) at QMineral (Leuven, Belgium) using a Bruker D8 Advance with XE-T detector and Cu-Kα radiation. The mineralogy of the bulk feedstock was also characterized, as well as four grain size fractions: 0-45 µm, 46-63 µm, 64-150 µm, and 151-250 µm. The elemental composition of the bulk feedstock was measured by ICP-MS at QMineral. All results are reported in Supplementary Material.

Native and post-deployment sediment core samples were characterized for grain size distribution using the image-based technology Instagrain (Sediment LLC, Greensboro, USA). Grain size analyses of the feedstock, which required higher resolution at the fine end of the size spectrum, were conducted by laser diffraction at QMineral. All results are reported in Supplementary Material.

2.3.2. Suspended Sediment Samples

Suspended sediment and foam samples collected for TSS, grain size, and mineralogy were filtered using 1 µm Sterlitech Corporation Glass Fiber Membrane Filters and utilized the entire sample collected in the field; no sub-sampling was performed. Mineralogical analyses were conducted using XRD and grain size using laser diffraction, as described above. Material was challenging to extract from the filters and required scraping, flushing with water and sonification in order to recuperate as much material as possible. Nevertheless, only a small quantity of material was produced for analysis, which likely influenced sample representativeness. Consequently, these samples should be considered indicative rather than definitive. All results are reported in Supplementary Material.

2.3.3. Water Chemistry

Discrete seawater samples were analyzed for trace metals, major cations, nutrients, pH, TA, and DIC. Trace metal and major cation samples were filtered to 0.45 µm, stored in acid-washed polypropylene bottles, preserved with HCl, and analyzed via ICP-MS at the University of Southern Mississippi Center for Trace Analysis, with percent error ranging from 5-20%. Trace metals analyzed were Cd, Pb, Al, Si, Cr, Mn, Fe, Co, Ni, Cu, and Zn. Major cations analyzed were Mg and Ca. Nutrient samples were filtered to 0.45 µm, stored in acid-washed polypropylene bottles, frozen, and analyzed via flow injection analysis at the Analytical Nutrient Lab at Moss Landing Marine Lab, with recovery rates ranging from 93-110%. Nutrients analyzed were PO_4^{3-}, NO_2^-, NO_3^- + NO_2^-, NH_4^+, and Si (molybdate reactive silica, primarily in the form of H_4SiO_4). Discrete pH samples were filtered to 0.45 µm and analyzed in-house on a Thermoscientific Orion Aquamate 8100 spectrophotometer using the unpurified m-cresol dye method of Douglas & Byrne (2017), with a long-term accuracy of 0.026 Δ pH units, precision of 0.006 pH units (1 SD) based on Tris buffer (n=17), precision of 0.004 pH units (1 SD) based on seawater samples (n=12). TA

samples were filtered to 0.45 µm, stored in borosilicate bottles, preserved with $HgCl_2$, and analyzed in-house via open-cell potentiometric titration using a Metrohm 855 Robotic Titrosampler with Metrohm 805 Dosimat and Metrohm Biotrode system following the method of Dickson et al. (2003), with a long-term accuracy of 0.18% and a precision of 4.93 µmol kg^{-1} (1 SD) based on repeated measurements of CRM Batch 219. DIC samples were filtered to 0.45 µm, stored in borosilicate bottles, preserved with $HgCl_2$, and analyzed in-house via Apollo SciTech AS-C5 Dissolved Inorganic Carbon Analyzer equipped with a Li-850 CO2/H2O Analyzer, with a long-term accuracy of 0.15% and precision of 4.8 µmol kg^{-1} (1 SD) based on repeated measurements of CRM Batch 219. The carbonate system was computed using CO2SYSv3 (Lewis and Wallace, 1998, Sharp et al., 2023) (MATLAB 2026a) with the input parameters of TA, DIC, and pH, with pH on the total scale, and K1, K2 constants from Hansson (1972, 1973) and Mehrbach et al. (1973), refit by Dickson and Millero (1987), with uncertainty of calculated parameters determined using the errors package in CO2SYSv3 (Orr et al., 2018). Finally, pigment samples were filtered on a 0.7 µm glass fiber filter and frozen at -20°C. Filters were extracted in 100% neutralized $MgCO_3$ and filtered ethanol for 30 minutes after 15 sec sonication. Extinctions at 632, 649, and 665 nm were measured spectrophotometrically and used to calculate chlorophyll-a concentrations using a trichroic equation from Ritchie (2008) with method precision of approximately 0.1%. Extinctions at 445 and 663 nm, corrected for absorbance at 750 nm were measured to calculate fucoxantin concentrations (Wang et al. 2018) with method precision of approximately 1-4.7%.

2.4. Data Processing

2.4.1. Berm Characterization

Morphological metrics for each placement (including berm area, height, width, length, and volume) were derived from differencing post- and pre-placement bathymetric surveys using the Raster Calculator tool in QGIS (version 3.26.2). The spatial extent of each berm was defined as the area where vertical change exceeded 10 cm, according to the multibeam's vertical accuracy. Maximum and average berm height, length and width were determined by extracting elevation data from transects through the long-axis of each berm. Berm volume was calculated by clipping the raster of difference to individual placement footprint vectors and using the Raster Surface Volume tool. Uncertainty associated with the berm volume is discussed in the Supplementary Material, including uncertainty due to survey accuracy, compaction of the seabed beneath the berms, sediment void ratios, and the potential exclusion of sediment deposited in thin layers beyond the main berm footprint.

2.4.2. Water Quality

2.4.2.1. Short-Term Observations

All statistical analyses were carried out in R (R version 4.4.1, R Core Team 2022) with significance assessed at a p-value of 0.05, unless otherwise stated. Turbidity data derived from the fixed sonde array were analyzed with a two-factor, non-parametric Aligned Rank Transform (ART) test with two factors: pre-/post- and depth group (surface, middle, bottom). Main-effect pair-wise contrasts were extracted from the ART linear model and evaluated with *emmeans* v1.10, using the Holm adjustment to control the family-wise error rate. A non-parametric Wilcoxon test was performed using the 'ranksum' function in MATLAB (version R2024b) to statistically compare turbidity values recorded by the fixed sonde array with those collected by the mobile sonde.

A mixed layer analysis concluded the seawater at this site is well-mixed, allowing for measurements and samples from all depths to be combined for statistical analyses (Supplementary Material). Mobile sonde data were divided into 5 turbidity-based groups to distinguish pre-placement baseline conditions (Cluster 1) from post-placement conditions (Clusters 2-5); this analysis was performed separately for

each placement to account for differences in baseline turbidity conditions. Post-placement data included both no-impact (Cluster 2) and impact (Clusters 3-5: low, medium and high impact) groups, using turbidity as a proxy. Cluster 2 was defined using an iterative thresholding method in which a turbidity threshold was identified such that the mean of Cluster 2 matched, within error, the mean of Cluster 1. Cluster 2 can therefore be considered outside of the turbidity plume, while Clusters 3-5 are considered inside the turbidity plume. The remaining post-placement data were partitioned using the *k*-means clustering function in MATLAB (version R2024b), with $k = 3$. Cluster quality was evaluated using the Silhouette score (S) (Kaufman and Rousseeuw, 2009). The resulting cluster labels were then applied to simultaneous sonde observations (pH, chlorophyll-*a*, dissolved oxygen). Discrete data were also assigned cluster numbers according to their proximity in space and time to mobile sonde measurements. Although the absolute values in the clusters vary across placement days, Clusters 3-5 collectively always represent the in-plume observations (i.e., statistically higher turbidity than each placement day's baseline), while Cluster 2 always represents post-deployment turbidity observations that are not statistically different from the Cluster 1 baseline (i.e., Cluster 2 is out-of-plume). This clustering approach enabled comparison of turbidity under contrasting hydrodynamic conditions and provided a common framework for analyzing additional measured parameters.

Outliers were removed from the mobile sonde data using the interquartile range (IQR) rule for non-parametric datasets (all chlorophyll-*a*, oxygen percent saturation from Placement 1 and 3). Further, turbidity influences chlorophyll-a measurements, and so where turbidity exceeded 30 NTU, chlorophyll-*a* data were excluded (Maciel et al., 2023). Measured dissolved oxygen was converted to oxygen percent saturation by calculating oxygen solubility via CSIRO Seawater Toolbox with inputs of measured salinity and temperature. Density was calculated via CSIRO Seawater Toolbox with inputs of measured pressure, salinity, and temperature.

A parametric one-way ANOVA test was applied for normally distributed data (Placement 1: oxygen percent saturation; Placement 2: chlorophyll-*a* and oxygen percent saturation), and a non-parametric Kruskall-Wallis test was applied for non-normally distributed data (Placement 1: chlorophyll-*a*; Placement 2: pH; Placement 3: pH, chlorophyll-*a*, oxygen percent saturation) with cluster as a factor. When significant effects were detected, a parametric Tukey or non-parametric Wilcoxon pairwise test was applied. To correct for the increased risk of Type I error due to multiple comparisons, p-values were adjusted using the Holm method for Wilcoxon rank-sum test.

Due to the small number of samples, statistical tests were performed on discrete data by binning all placement day data into Baseline (Clusters 1) versus Impact (Clusters 3-5) groups . Samples in Cluster 2 were omitted from these analyses due to their position outside of the turbidity plume. The Baseline and Impact groups were found to be normally distributed via the Shapiro-Wilk test, and the Welch's t-test was used to test for significance between Baseline and Impact groups for the three placements combined.

2.4.2.2. Long-Term Observations

The hypothesis that spatial variability in post-deployment water column measurements was influenced by proximity to the placement area (Olivine station) was evaluated using sonde data (Supplementary Material). A lack of significance led to combining all stations for long-term pre- and post-deployment analysis. The IQR rule was used to remove outliers as described above. A date-to-date comparison was performed using Wilcoxon pairwise tests with Holm method adjustment. Similarly, all parameters for discrete water column samples were statistically analyzed for date-to-date comparisons using the Wilcoxon pairwise test with Holm method adjustment.

2.5. CDR modeling

To mechanistically contextualize discrete field observations and quantify the magnitude and timescale of gross carbon dioxide removal from dissolution of suspended feedstock released during the trial, the empirical datasets were integrated with a numerical modeling framework. The model comprises two components, a sediment transport module and a geochemical module. The two modules are offline coupled, such that outputs from the sediment transport module provide boundary conditions for the geochemical module. See Supplementary Material for full description of model.

The sediment transport module estimates the threshold grain size for suspension under given hydrodynamic conditions using established sediment transport formulations, including the Rouse number (Rouse 1937), Shields parameter (Soulsby and Whitehouse 1997), and wave-current bed shear stresses (Soulsby 1997). Using this module, the mass of feedstock entrained in the water column and its corresponding grain size distribution is derived. Applying the grain size-dependent mineralogy of the feedstock, as determined by XRD, the sediment transport module calculates forsteritic olivine content at 1 µm increments across the suspended sediment grain size distribution. These parameters define the initial conditions for the geochemical module, which simulates dissolution of olivine, trace metal release (specifically Ni and Co), alkalinity generation, and the magnitude and timescale of gross carbon dioxide removal from suspended olivine in a 0d box model. Dissolution kinetics are resolved using literature dissolution rates (Rimstidt et al., 2012) and are implemented with a shrinking core model to account for decreasing particle size through time (e.g., Hangx and Spiers, 2009; Olsen and Rimstidt, 2007). The cumulative mass of dissolved olivine is converted to alkalinity production using a 4:1 alkalinity-to-olivine stoichiometric relationship. To estimate potential CDR, alkalinity production is further scaled by an air-sea gas exchange efficiency factor of 70.5%, the annual long-term efficiency near the site location (Zhou et al., 2025).

The model was run with two applications. First, the model was used to predict changes to water column chemistry (e.g. Ni, Co, and alkalinity concentrations) that would result from olivine dissolution during individual placements. Model inputs include the grain size distribution and mineralogy from TSS samples taken close in space and time to the discrete seawater samples, and pH and temperature of each placement day. Model outputs were ultimately compared to measured Ni, Co, and alkalinity concentrations from four discrete seawater samples, taken from both Placement 2 and 3 in medium- to high- impact areas (clusters 4 and 5), to evaluate key model assumptions about olivine dissolution, such as the validity of laboratory-derived olivine dissolution rates in the real-world. The model was not compared against Placement 1 discrete seawater samples because no samples were collected in the medium or high impact areas during this placement. In this application, the model was set up as a closed system with the full mass of olivine released during each placement dissolving in a fixed volume of seawater defined by the seafloor footprint of the placement. This simple approach provides an upper bound on possible Ni, Co, and alkalinity from olivine dissolution in the water column.

Second, because olivine dissolution is relatively slow and expected to occur over decadal to centennial timescales, potentially far from the project site, the model was configured to test the sensitivity of long-term gross carbon dioxide removal outcomes from the field trial under different hypothetical scenarios that vary environmental and physical conditions (Table 1, Supplementary Material). This analysis focused on two key time horizons: 20 years, corresponding to typical carbon crediting periods (Michaelowa et al., 2019), and the full olivine dissolution timeline. The CDR described here is gross CDR as it does not take into account project emissions.

3. Results

3.1. Short-Term Observations

3.1.1. Oceanographic Conditions

Placement 1 had notably different conditions compared to Placement 2 and 3 (Supplementary Material). Placement 1 experienced greater wave heights (0.85 m) than Placement 2 (0.39 m) and Placement 3 (0.59 m). The mean wave direction during Placement 1 was onshore with a slight southward inclination (61°), whereas Placement 2 and 3 had more northward-directed waves (122° and 120°, respectively). Wave periods also varied, measuring 7.8 s, 7.2 s and 5.6 s during Placement 1-3. The current was moving at a rate of 0.45 m s^{-1} towards the south (162°) during Placement 1. The currents were slower and directed northward during Placement 2 and 3, with speeds of 0.26 m s^{-1} towards 342° and 0.21 m s^{-1} towards 329° respectively.

3.1.2. Turbidity and Suspended Sediment

A turbidity plume was generated during each placement with peak responses generally occurring within the first few hours post-placement (Figure 2), although plume magnitude and spatial extent varied with hydrodynamic conditions. Placement 2 exhibited the highest turbidity across the deployment, followed by Placements 1 and 3. For Placements 2 and 3, maximum turbidity occurred away from the placement site, reflecting lower-energy conditions that promoted advective transport of a more concentrated plume. In contrast, maximum turbidity during Placement 1 was recorded over the berm, consistent with higher-energy conditions that promoted mixing, resuspension, and rapid plume dilution during transport.

Placement 1 generated an intense and sustained near-field turbidity plume that dispersed rapidly with transport away from the placement site under relatively high-energy conditions. Measurements over the berm showed significant post-placement turbidity increases at all depths ($p < 0.001$, Supplementary Material), with a strong near-bed response (pre: 12.84 $\pm$ 0.21 NTU, n = 1136; post: 32.70 $\pm$ 0.35 NTU, n = 1077; peak: 83.21 NTU at +202 minutes) (Supplementary Material). The mid-depth exhibited the largest relative increase (pre: 2.88 $\pm$ 0.03 NTU, n = 1136; post: 10.82 $\pm$ 0.23 NTU, n = 1077; +275%). Turbidity declined at both depths through time, but showed substantial variability and no sustained return to baseline during the placement monitoring day. Surface turbidity at the top of the water column generally increased through time throughout the monitoring day. The plume advected southeast on the dominant current with a diffuse and heterogenous structure. Cluster 2 conditions dominated following placement, with intermittent higher-intensity occurrences (Cluster 3-5, Figure 2A) that were short-lived (+102 and +203 minutes) and spatially discontinuous (121–654 m from the release site). Cluster 5 conditions were rare, with a single observation of 32.85 NTU at +126 minutes and 288 m (Supplementary Material). TSS concentrations reflected a similar dispersed plume structure, with the majority of values below the baseline mean (9.2 $\pm$ 1.3 mg l^{-1}; Supplementary Material). Occasional elevated concentrations occurred after +190 minutes at varying distance from the placement site (154-454 m), reaching a maximum of 44.1 mg l^{-1}.

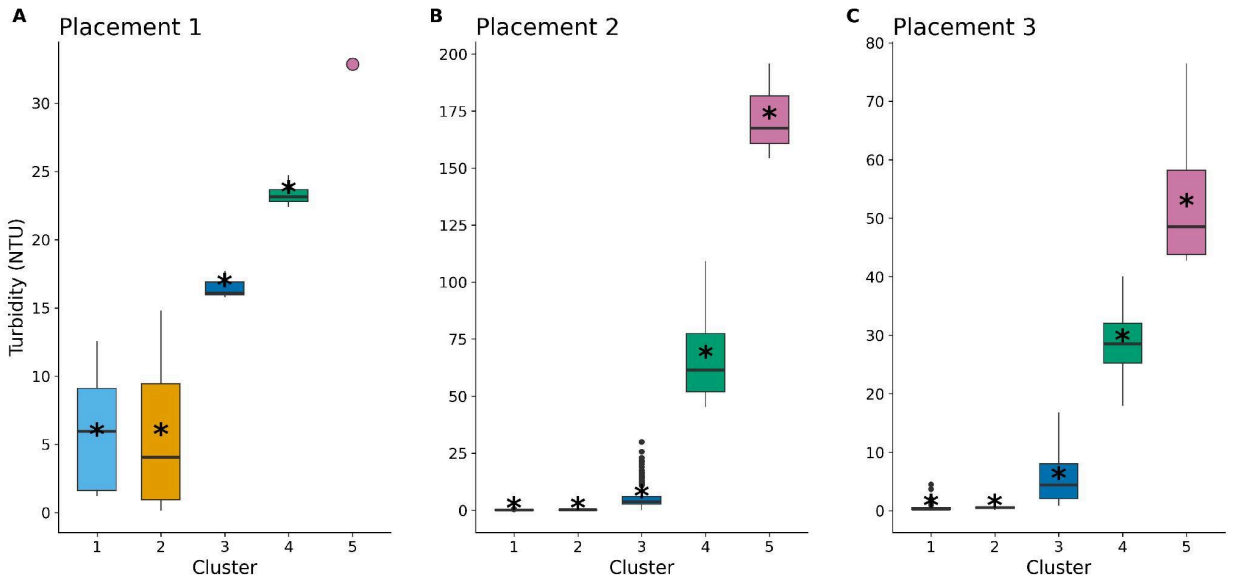


Figure 2 Turbidity concentrations (NTU) for each placement as recorded by the mobile sonde, discretized by cluster number. Mean (asterisks), median (center line), 25th and 75th percentiles (box), minimum and maximum value (vertical lines), outliers (dots) are presented. Note the differing y-axis scales.

In contrast to Placement 1, Placement 2 generated a weaker and shorter-lived turbidity response over the berm; these lower-energy conditions coincided with a more spatially concentrated plume away from the placement site. There was a depth-dependent response over the berm, with an increase in turbidity mid-depth (pre: 0.14 ± 0.01 NTU, n = 43; post: 0.53 ± 0.01 NTU, n = 78), and a decrease at the surface (pre: 1.69 ± 0.01 NTU, n = 43; post: 1.28 ± 0.02 NTU, n = 80) (Supplementary Material). The bottom sensor failed pre-placement, however, post-placement measurements showed an initial peak of 52.36 NTU at +23 minutes, declining to 1.37 ± 0.04 NTU (n = 60) after +61 minutes. The plume advected northwest with the dominant current, with the highest cluster intensities across all placements. Turbidity rapidly increased from moderate-impact (Cluster 3: 11.92 + 2.32 NTU, n = 9) to peak impact (Cluster 4: 70.07 + 11.25 NTU, n = 3; Cluster 5: 164.48 + 9.49 NTU, n = 5), reaching a maximum of 195.49 NTU (Figure 2B). These higher-intensity clusters (4-5) were short-lived (+20-23 minutes) and confined to the proximal plume field (59-84 m of the placement site). After +63 minutes, turbidity declined to predominantly Cluster 2-3 conditions; Cluster 3 was observed over 2 km from the site, indicating sustained advective plume transport. TSS concentrations exceeded the baseline mean (4.7 ± 0.7 mg l^{-1}, n = 5) and broadly reflected the cluster-defined concentrated plume structure, reaching a maximum of 97.7 mg l^{-1} at +26 minutes and 48 m from the release site . However, TSS exhibited greater spatio-temporal variability than turbidity, likely reflecting heterogeneous suspended sediment concentrations and the discrete nature of sampling (Supplementary Material).

Compared to Placement 2, Placement 3 generated a moderate turbidity signal over the berm and less concentrated advected plume under higher energy conditions that promoted dispersion. The berm showed significant post-placement turbidity increases at surface and mid-depths ($p < 0.001$, Supplementary Material), with the highest intensity and pre-post increase found at the latter (pre: 1.38 ± 0.03 NTU, n = 41; post: 4.16 ± 0.72 NTU, n = 52; +202%; peak: 23.73 NTU at 22 minutes) (Supplementary Material). Surface turbidity peaked at 11.15 NTU after +26 min but by +34 min, 61% of values fell below baseline. The bottom sensor failed pre-placement, but post-placement turbidity peaked at 56.45 NTU after +22 minutes, then declined to 1.63 ± 0.09 NTU (n = 39) after +42 minutes. The plume advected northwest with the dominant current, with moderate cluster intensities. Following placement, a rapid

onset of Cluster 4-5 conditions occurred within +20 minutes and 100 m of the placement site (Cluster 4: 30.27 ± 0.97 NTU, n = 13; Cluster 5: 57.73 ± 4.24 NTU, n = 7) (Figure 2C). Peak plume conditions reached a maximum of 76.32 NTU at +17 minutes and 64 m northwest of the placement site. Elevated Cluster 4-5 conditions persisted intermittently until approximately +35 minutes, to a maximum distance of 202 m. Thereafter, Cluster 3 conditions (4.70 ± 0.36 NTU, n = 85) dominated the plume field with occurrences of Cluster 2 conditions (0.52 ± 0.03 NTU, n = 35). Both cluster states were advected over 500 m from the placement site, although Cluster 2 conditions extended over a greater spatial range than Cluster 3, indicating progressive dilution and recovery during plume transport. TSS reflected a similar plume structure, with a peak of 87.2 mg l^{-1} within +18 minutes and 69 m of the placement site (Supplementary Material). TSS decreased significantly with distance from the placement site ($r = -0.61$, $p < 0.01$). Two TSS samples were analyzed from Placement 2 for grain size distribution and mineralogy, while three TSS samples were similarly analyzed from Placement 3 (Supplementary Material). Each placement showed progressive decreases in grain size (Placement 2: D50 from 130µm to 50µm; Placement 3: D50 from 74µm to 0.39 µm) and olivine content (Placement 2: 93.6 wt% to 33.7 wt%; Placement 3: 73 wt% to 57 wt%) with increasing time and distance from the placement site. Satellite imagery collected the following day (14 June 2024) showed no visible plume, only the footprint of Placement 2 and 3 viewed through the water column (Supplementary Material).

3.1.3. Mobile sonde pH, oxygen and Chl-A

During Placement 1, the pH sensor on the mobile sonde malfunctioned, resulting in no data. During Placement 2, pH ranged from 7.96 - 8.03. During Placement 3, pH ranged from 8.03 - 8.06. These values are within the error of the pH sensor (± 0.1), rendering significance tests inconclusive, however the data are consistent with variability observed in North Carolina coastal and estuarine systems. For example, measurements from the Neuse River Estuary, Pamlico Sound, and Onslow Bay show pH values typically ranging from ~7.7 to 8.2 in surface waters, with variability driven by biological activity, mixing, and freshwater inputs (BCO-DMO, 2024).

Chlorophyll-*a* values presented differences among clusters for all three placements, however the pattern was not consistent across the placements. Placement 1 had the highest values across placements; means ranged from 0.10 - 2.00 RFU (Figure 3A). Cluster 1 (0.11 ± 0.03 RFU, n = 9) and Cluster 2 (0.10 ± 0.02 RFU, n = 18) were statistically the same ($p > 0.05$) and both statistically lower ($p < 0.05$, Supplementary Material) than Cluster 3 (1.09 ± 0.81 RFU, n = 3) and Cluster 4 (2.00 ± 1.0 RFU, n = 5), showing an increase in chlorophyll-*a* with turbidity. Overall lower chlorophyll-*a* values were reported during Placement 2 as compared to Placement 1; cluster means ranged from 0.04 to 0.08 RFU (Figure 3B). Cluster 1 (0.08 ± 0.00 RFU, n = 39) was statistically higher ($p < 0.05$) than Cluster 2 (0.04 ± 0.00 RFU, n = 18) and Cluster 3 (0.05 ± 0.00 RFU, n = 239), showing a decrease in chlorophyll-*a* after placement. Similar chlorophyll-*a* values were reported during Placement 3 as compared to Placement 2; means ranged from 0.07 - 0.09 RFU (Figure 3C). Cluster 1 (0.07 ± 0.00 RFU, n = 72) had significantly lower chlorophyll-*a* values than Cluster 3 (0.09 ± 0.00 RFU, n = 96, $p < 0.005$). For both Placement 2 and 3, Clusters 4 and 5 were affected by turbidity levels exceeding 30 NTU which obscure sensor measurements and therefore no statistical comparison was performed. No discrete water samples for chlorophyll-*a* were collected during placements.

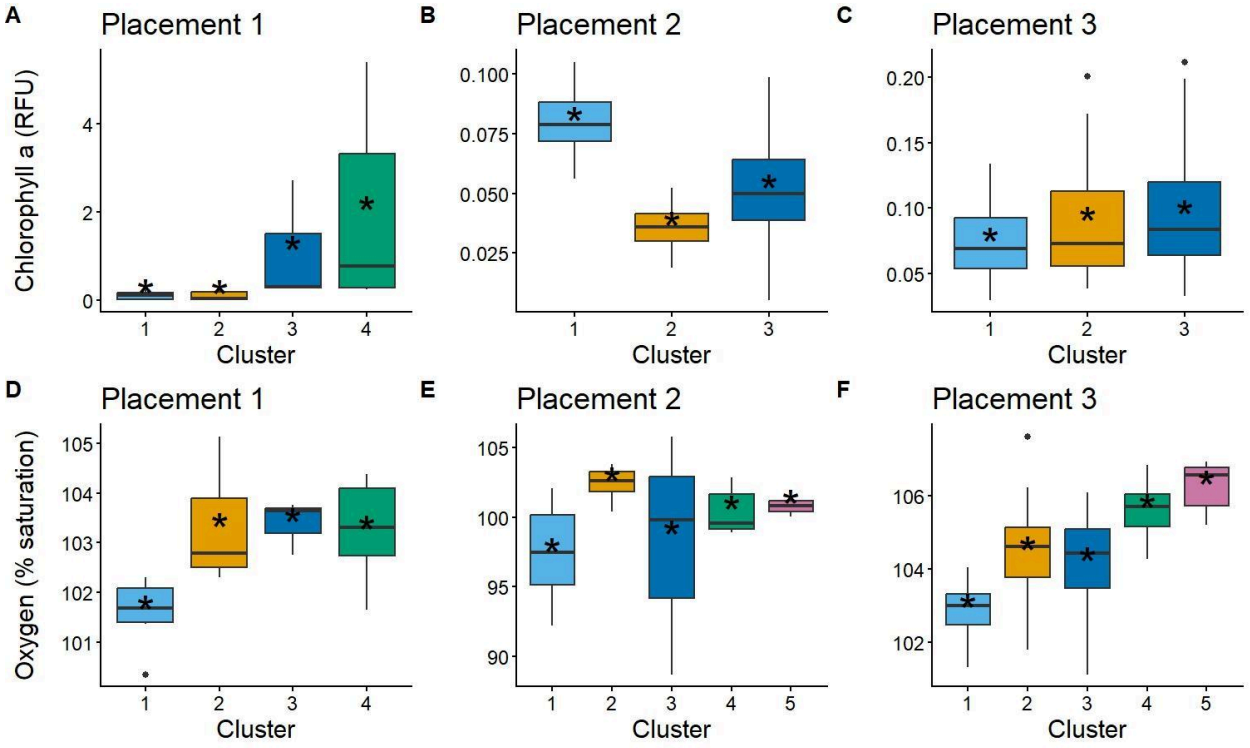


Figure 3 A-C) Chlorophyll-*a* fluorescence (RFU) and D-F) oxygen percent saturation (%) measured by the sonde during placement days, categorized by clusters. Mean (asterisks), median (center line), 25th and 75th percentiles (box), minimum and maximum value (vertical lines), outliers (dots) are presented.

Similarly, oxygen percent saturation presented differences among clusters for all three placements, however the pattern was not consistent across the placements. During Placement 1, the cluster means ranged from 101.6 - 103.4 % O_2 (Figure 3D). Cluster 1 (101.6 ± 0.3 % O_2, n = 7) was statistically lower ($p < 0.05$, Supplementary Material) than Cluster 2 (103.1 ± 0.2 % O_2, n = 13), Cluster 3 (103.4 ± 0.3 % O_2, n = 3), and Cluster 4 (103.2 ± 0.5 % O_2, n = 5), showing an increase in oxygen percent saturation after placement. No other pairs of clusters were significantly different from each other. During Placement 2, the oxygen percent saturation cluster means ranged from 97.3 - 102.4 % O_2 (Figure 3E). Cluster 2 (102.4 ± 0.2 % O_2, n = 18) was statistically higher ($p < 0.05$) than Cluster 1 (97.3 ± 0.5 % O_2, n = 40) and Cluster 3 (98.6 ± 0.3 % O_2, n = 243). No other pairs of clusters were significantly different from each other. During Placement 3, the oxygen percent saturation cluster means ranged from 102.9 - 106.2 % O_2 (Figure 3F). Cluster 1 was significantly lower than all clusters ($p<0.05$, 102.9 ± 0.1 % O_2, n = 71), showing an increase in oxygen percent saturation after placement. Cluster 2 (104.4 ± 0.2 % O_2, n = 33) and Cluster 3 (104.2 ± 0.1 % O_2, n = 96) were statistically the same, and significantly lower than both Cluster 4 (105.6 ± 0.1 % O_2, n = 30) and Cluster 5 (106.2 ± 0.2 % O_2, n = 12, $p < 0.05$).

3.1.4. Discrete water chemistry

Out of all discrete seawater chemistry parameters (metals: Ni, Co, Cd, Cr, Cu, Fe, Mn, Si, Zn; carbonate chemistry: discrete pH, DIC, TA, pCO_2, staturate state of aragonite ($\Omega_{aragonite}$); major cations: Ca, Mg; nutrients: NO_2^-, NH_4^+, NO_3^- + NO_2^-, SiO_2), the placement day impact analysis showed only Ni and Co had statistically significant ($p < 0.05$) increases between the Baseline (Clusters 1) and Impact groups (Clusters 3-5) (Figure 4). Ni increased from 0.007 ± 0.000 µmol kg^{-1} in the Baseline to 0.015 ± 0.003 µmol kg^{-1} in the Impact group ($p < 0.01$). Co increased from 0.0005 ± 0.0000 µmol kg^{-1} in the Baseline to 0.0009 ± 0.0000 µmol kg^{-1} in the Impact group ($p < 0.01$). Samples were analyzed for Pb and Al in addition to metals above, but were below detection limits (0.00014 µmol kg^{-1} and 0.25 µmol kg^{-1}, respectively) in all

but one sample, so their values are not reported. Similarly, PO_4^{3-} remained below the detection limit (0.00 µmol kg^{-1}) both during and after all the placements. We note that $\Omega_{aragonite}$ remained well below thresholds previously seen to promote secondary carbonate precipitation in OAE experiments (e.g., Hashim et al., 2025, Moras et al., 2022). Finally, freshwater inputs at this nearshore site present a potential confounding variable that could obscure OAE-induced signals. A statistically significant alkalinity-salinity relationship derived from the annual dataset confirmed that observed alkalinity was impacted by freshwater mixing; however, the difference between salinity-normalization Baseline and Impact placement groups remained statistically insignificant (Supplementary Material).

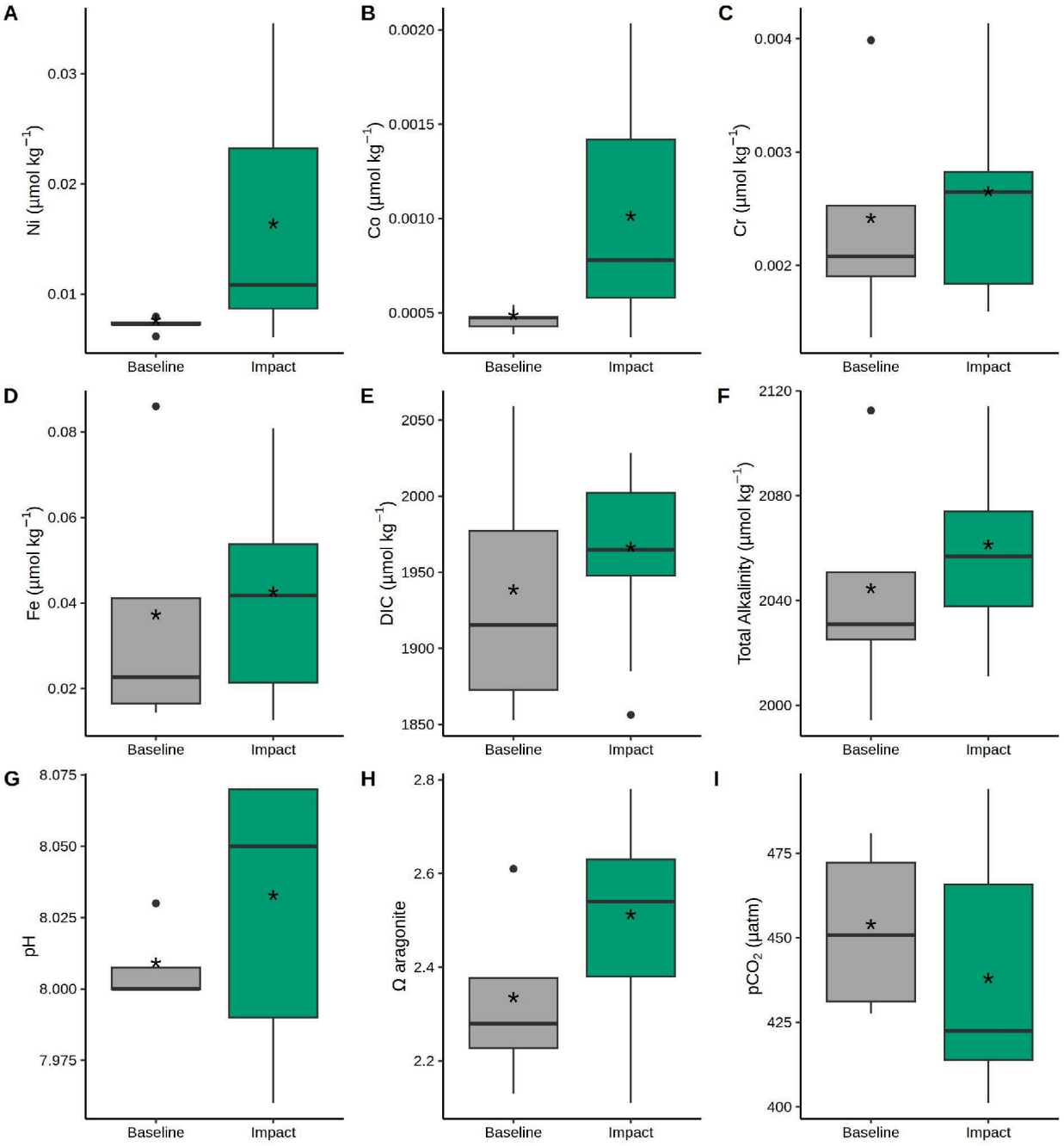


Figure 4 Trace metal concentrations (A-D) as well as carbonate chemistry parameters (E - I) of discrete seawater samples from Baseline (Cluster 1) and Impact clusters (Clusters 3-5), combined for all placements. Mean (asterisks), median (center line), 25th and 75th percentiles (box), minimum and

maximum value (vertical lines), outliers (dots) are presented. $\Omega_{aragonite}$ was calculated with CO2SYS using DIC and pH.

3.2. Long-Term Observations

3.2.1. Oceanographic Conditions

Oceanographic conditions at the study site are highly dynamic. From April 2024 to 2025, data showed significant wave heights of 0.98 ± 0.46 m (mean ± SE), peak wave periods of 8.37 ± 2.76 s, and current speeds of 0.18 ± 0.13 ms^{-1}. Currents dominantly flowed from north to south (58.8%), whilst waves had a south to north dominance (58.7%); in both cases, directional preference was relatively weak.

3.2.2. Turbidity and Suspended Sediment

Pre-deployment, baseline turbidity values (mean ± SE) demonstrate substantial variability across the study region with a range (8.22 ± 1.67 NTU) comparable to that observed across post-deployment surveys (5.78 ± 1.41 NTU). The majority of pairwise comparisons between April 2024 and April 2025 showed no significant differences in turbidity values between consecutive surveys ($p > 0.05$; Figure 5A). No significant difference was found between turbidity on 30th April 2024 and 8th July 2024, either side of the deployment.

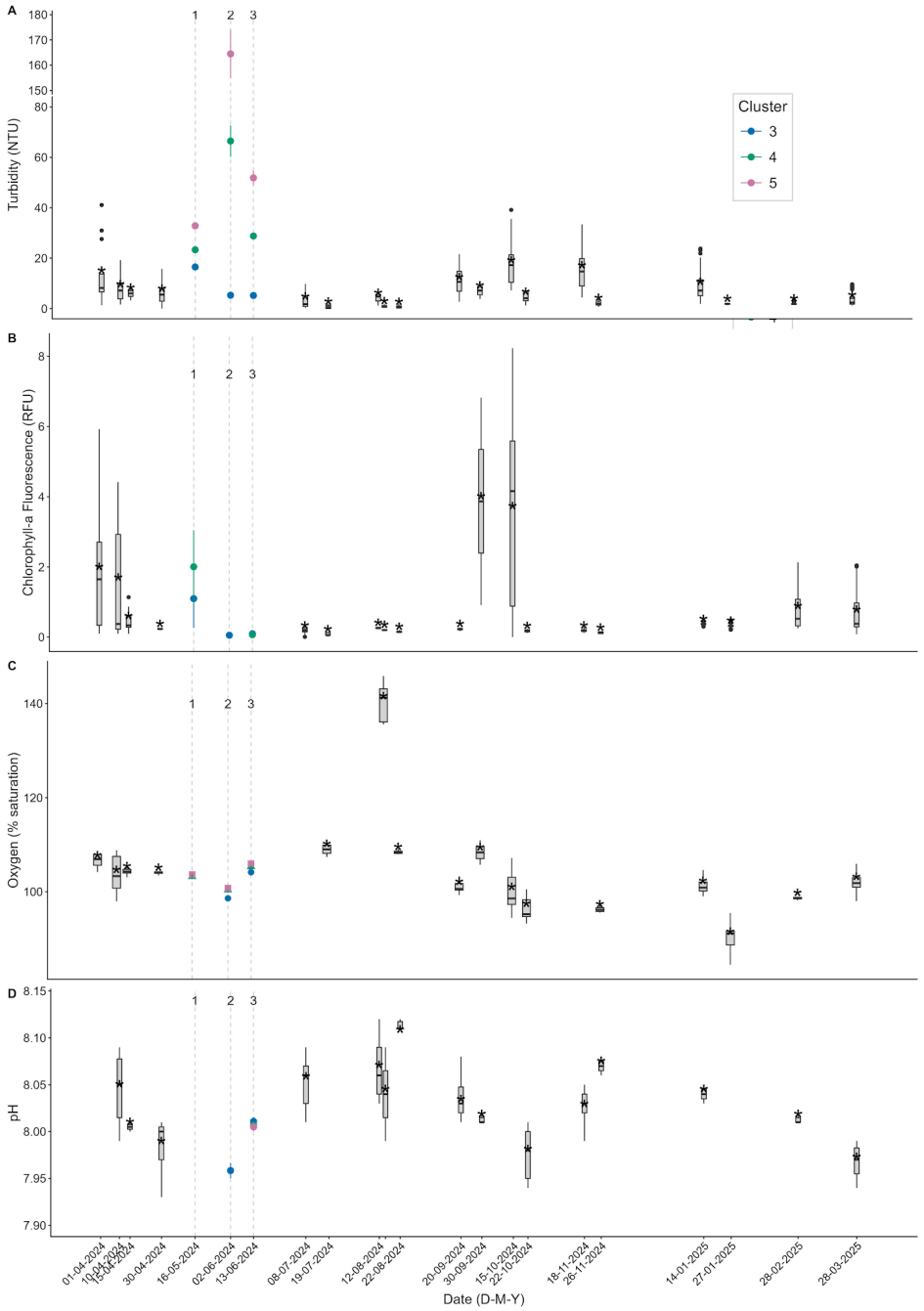


Figure 5 A) Turbidity (NTU), B) Chlorophyll-*a* (RFU), C) oxygen % saturation, and D) pH recorded before and after the deployment with the sonde. Mean (asterisks), median (center line), 25th and 75th percentiles (box), minimum and maximum value (vertical lines), outliers (dots) are presented. Placements are marked with a dashed line, and labeled 1, 2, and 3 accordingly. The mean and standard error (coloured dot and vertical line) for each placement day (derived from Impact clusters) has been plotted for reference. The date 15-08-2024 falls between 12-08-2024 and 22-08-2024 but is omitted from the x-axis to prevent label overlap.

Significant differences in turbidity were observed between 3 out of 19 pairs of surveys: 22nd August 2024 (0.69 ± 0.13 NTU, n = 18) and 20th September 2024 (10.44 ± 1.51 NTU, n = 14; $p < 0.001$), 18th (15.14 ± 1.42 NTU, n = 33) and 26th (2.20 ± 0.74 NTU, n = 4; $p < 0.01$) November 2024, 14th (8.54 ± 0.35

NTU, n = 178) and 27th (1.88 ± 0.04 NTU, n = 39; $p < 0.001$) January 2025 (Figure 5A, Supplementary Material).

3.2.3. Mobile sonde Chl-A, oxygen, and pH

Pre-deployment, baseline chlorophyll-*a,* percent oxygen saturation, and pH values (mean ± SE) similarly demonstrate substantial variability across the study region with ranges comparable to that observed across post-deployment surveys (Chl-A was 1.02 ± 0.4 RFU vs 0.78 ± 0.34 RFU, pre- vs post-deployment, respectively, percent oxygen saturation was 104.65 ± 0.69 % O_2 vs 101.06 ± 1.75 % O_2, respectively and pH was 8.01 ± 0.018 vs 8.03 ± 0.012, respectively).

Mean chlorophyll-*a* values were statistically similar ($p > 0.05$, Supplementary Material) either side of the deployment (30th April 2024: 0.23 ± 0.01 RFU, n = 12; 8th July 2024: 0.18 ± 0.01 RFU, n = 33). Significant differences were observed in 6 out of 19 month-to-month pair post-deployment (Figure 5B). The few discrete chlorophyll-*a* samples presented a similar range of values for pre- and post-deployment surveys: 1.12-3.03 µg L^{-1} for 13th of March 2024, and from 1.39 to 3.45 µg L^{-1} for 3 post-deployment surveys (12th August, 18th November 2024, 28th February 2025). The fucoxanthin pigment presents a similar pattern, although the post-deployment surveys had a higher range of values: 1.29-1.93 µg L^{-1} for 13th of March 2024, and 0.59-2.05 µg L^{-1} for 3 post-deployment surveys (12th August, 18th November 2024, 28th February 2025).

All percent oxygen saturation values reported pre- and post-deployment were near or above saturation (100%; Figure 5C). Mean percent oxygen saturation was statistically similar ($p > 0.05$, Supplementary Material) either side of the deployment (30th April 2024: 104.11 ± 0.13 % O_2, n = 6; 8th July 2024: 112.70 ± 0.85 % O_2, n = 37). Significant differences were observed in 4 out of 19 month-to-month pair post deployment.

Sonde pH data were compared month-to-month for pairwise comparisons. All pairwise differences between April 2024 and April 2025 were within the error of the pH sensor (± 0.1), rendering the significance tests inconclusive (Figure 5D), but similarly to short-term results, remained within natural variability of the study's system (BCO-DMO, 2024).

3.2.4. Discrete seawater chemistry

Of all trace metals measured (Ni, Co, Cd, Cr, Cu, Fe, Mn, Si, Zn), only Mn and Cu concentrations were statistically different on either side of the deployment ($p < 0.05$, Supplementary Material). Mn increased from 13 March 2024 (0.0096 ± 0.0006 µmol kg^{-1}, n = 3) to 25 June 2024 (0.0511 ± 0.0008 µmol kg^{-1}, n = 4), whereas Cu decreased over the same period (13 March 2024: 0.0092 ± 0.0005 µmol kg^{-1}, n = 3; 25 June 2024: 0.0046 ± 0.0000 µmol kg^{-1}, n = 4). Co (Figure 6B), Cd, and Si showed significant differences in at least one month-to-month comparison post deployment ($p<0.05$, Supplementary Material). Conversely, Ni (Figure 6A), Cr, Fe, Mn, Cu and Zn showed no significant differences across any month-to-month comparisons post deployment ($p>0.05$). Samples were also analyzed for Pb and Al, but were found to be below detection limits (0.00014 µmol kg^{-1} and 0.25 µmol kg^{-1}, respectively) in all but one and six samples, respectively, so their values are not reported.

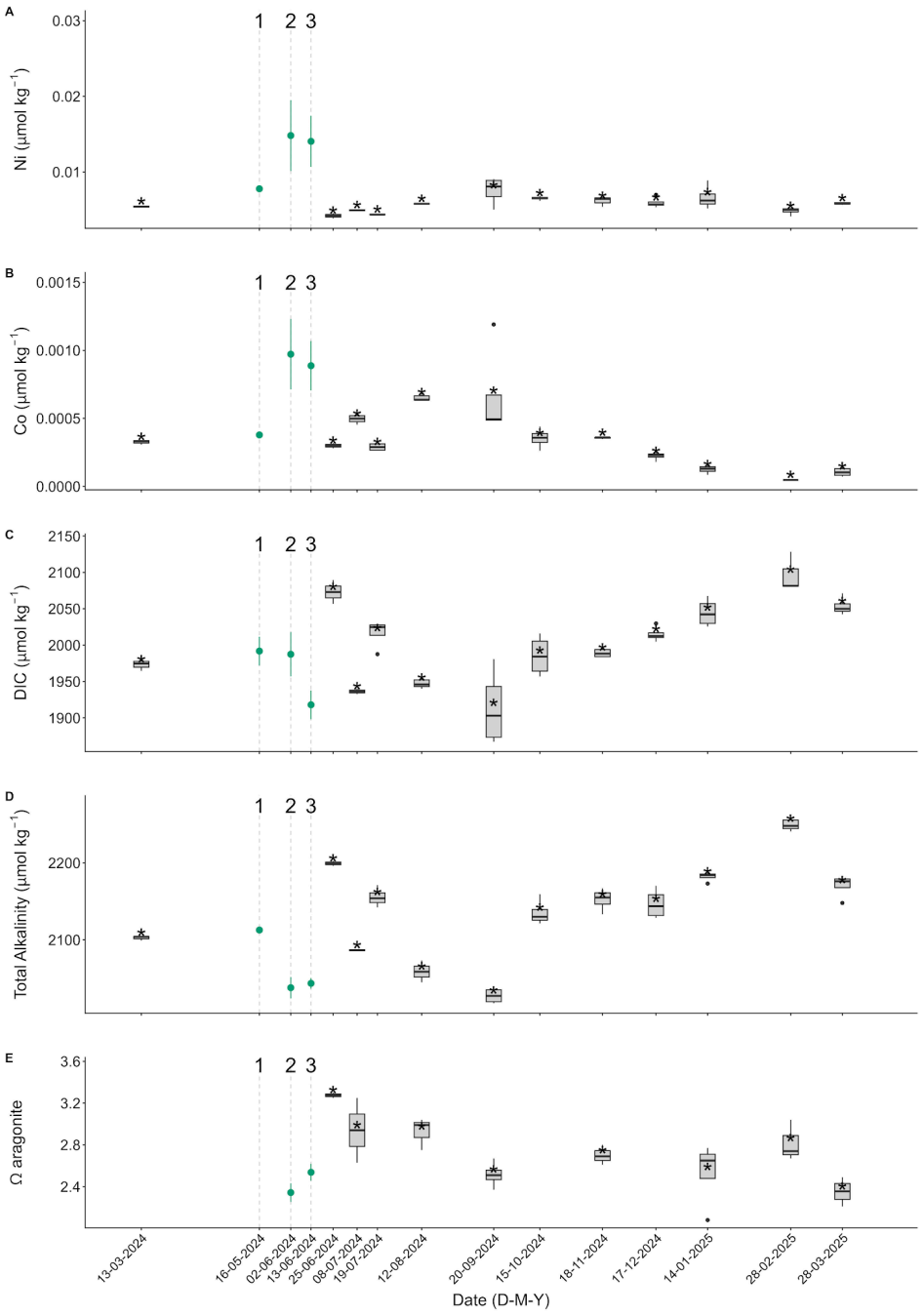


Figure 6 Discrete trace metal and carbonate chemistry seawater samples from March 2024 to March 2025: (A) Ni, (B) Co, C) DIC, D) Total Alkalinity, E) $\mathbf{\Omega}_{aragonite}$. Sample counts ranged from 3-4 samples per survey day. Mean (asterisk), median (horizontal line), 25th and 75th percentile (box), minimum and maximum value (vertical line), and outliers (dots) are presented. The mean and SD (green point and vertical line) derived from Impact Clusters (Clusters 3–5) for each Placement (1, 2, 3) has been plotted for reference. $\mathbf{\Omega}_{aragonite}$ (E) was calculated with CO2SYS using DIC and pH; $\mathbf{\Omega}_{aragonite}$ is missing from the first survey due to a sonde malfunction in which pH was not recorded

Major cations (Ca and Mg) exhibited statistically significant differences on either side of the deployment ($p < 0.000$, Supplementary Material). Both increased from 13th March 2024 (Ca: 9.20 ± 0.05 mmol kg^{-1}, n=3; Mg: 45.87 ± 0.13 mmol kg^{-1}, n = 4) to 25th June 2024 (Ca: 9.88 ± 0.02 mmol kg^{-1}, n=3; Mg: 49.08 ±

0.27 mmol kg^{-1}, n = 4). Statistically significant differences were also reported for 9 of 12 the month-to-month pairs ($p < 0.05$, Supplementary Material).

Of the four nutrients measured (NO_2^-, NH_4^+, NO_3^- and NO_2^-, SiO_2), none reported significant differences on either side of the deployment ($p > 0.05$). NO_2^-, NH_4^+ and SiO_2 exhibited statistically significant differences in at least one month-to-month pair post deployment ($p < 0.05$, Supplementary Material). PO_4^{3-} was below the detection limit (0.00 µmol kg^{-1}) for 9 of 12 surveys, and therefore was not analyzed for statistical significance.

Out of the carbonate chemistry parameters (discrete pH, DIC, TA, pCO2, $\Omega_{aragonite}$) DIC and TA were statistically different on either side of the deployment ($p < 0.05$, Figure 6C-E, Supplementary Material). DIC significantly increased from 13 March 2024 (1973.5 ± 8.1 µmol kg^{-1}, n = 3) to 25 June 2024 (2073.1 ± 23.1 µmol kg^{-1}, n = 2). TA significantly increased from 13 March 2024 (2102.5 ± 3.1 µmol kg^{-1}, n = 3) to 25 June 2024 (2199.3 ± 4.5 µmol kg^{-1}, n = 2). Moreover, all measured and calculated carbonate chemistry parameters exhibited statistically significant differences in at least one month-to-month pair post-deployment ($p < 0.05$, Figure 6E, Supplementary Material). The $\mathbf{\Omega}_{aragonite}$ over the year remains well below thresholds previously seen to promote secondary carbonate precipitation in OAE experiments (e.g., Hashim et al., 2025, Moras et al., 2022) (Figure 6E).

4. Discussion

4.1. Environmental Impact

Overall, environmental impacts from the project were negligible and, where present, short-lived and localized. Across all scales (temporal, spatial), perturbations either remained within natural variability or dissipated rapidly, and in both instances, did not translate into measurable biological effects. This is true for all major pathways in which OAE could impact coastal ecosystems: (1) turbidity and associated light limitation, (2) release of nutrients and trace metals (Bach et al., 2019; Flipkens et al., 2021), and (3) changes in carbonate chemistry (Montserrat et al., 2017; Geerts et al., 2025). Together, these processes are linked to key concerns around phytoplankton blooms, plankton community shifts, and oxygen depletion (Dai et al., 2023). For example, Hutchins et al. (2023) showed that diatoms can utilize Si and Fe from olivine leachate to support near-maximal growth, whereas Guo et al. (2024) observed no stimulation, likely due to nitrogen limitation. Extensive bloom formation can lead to hypoxia through microbial decomposition of organic matter (Dai et al., 2023). Thus, OAE-induced turbidity, nutrient and trace metal release, and carbonate chemistry changes could influence ecosystem oxygen dynamics.

During placements, the observed environmental impacts were confined to short-term physical and chemical perturbations. Placement 2 and 3 turbidity peaked at 195.49 and 76.32 NTU respectively, but showed progressive dilution of the turbidity plume during day-of-monitoring with no- to low-impact (Cluster 2-3) conditions becoming dominant 63 minutes and 35 minutes after placement respectively (Figure 2A). Placement 1 turbidity peaked at 83.21 NTU and showed a less coherent pattern, with turbidity showing no sustained return to baseline at the placement site and short-lived, spatially discontinuous peaks in turbidity across the plume field during the placement day (Figure 2A). No persistent plume was detected in satellite imagery the days following placements (Supplementary Material). Longer-term monitoring showed no lasting impact, with turbidity remaining within baseline variability through April 2025 (Figure 5A). A single exception occurred on 15 October 2024 (17.14 ± 1.59 NTU), likely linked to a regional chlorophyll-*a* increase in Chesapeake Bay and associated plume transport (CoastWatch, 2025). Most evidence from beach nourishment studies indicates that turbidity

and its ecological impact from release sediment in the nearshore is localized and short-lived under energetic hydrodynamic conditions (Roman-Sierra et al., 2011). Usually, plumes peak (up to ~200 NTU) and dissipate within minutes to hours (Nichols et al., 1978; Van Dolah et al., 1994; Roman-Sierra et al., 2011; USACE, 2001a). This agrees with the current study, suggesting that project effects are broadly similar to native sand placements for beach nourishment in the nearshore setting.

Similarly, trace metal responses were minimal and short-lived, but did provide a resolvable signal of olivine dissolution during placements as only Ni and Co showed transient increases during placement days (Ni: 0.5-1.1 μg L^{-1}; Co: 0.02-0.07 μg L^{-1}). Ni and Co are commonly highlighted as potential concerns for olivine-based OAE but Ni concentrations remained around one order of magnitude below chronic US EPA water quality guidelines (8.2 μg L^{-1}) (Supplementary Material). In contrast, Cr, also frequently cited as a concern for olivine-based OAE, showed no increase. This likely reflects its presence primarily in chromite ($FeCr_2O_4$) rather than within the olivine structure, and the relatively low reactivity and dissolution rate of chromite under seawater conditions (e.g., Oze et al., 2007; Rimstidt et al., 2012). In month-to-month comparisons, including immediately pre- and post- deployment, the key metals associated with olivine (Ni, Co, Cr, Fe) showed little to no statistical differences. This suggests that the olivine deployment did not meaningfully alter water column concentrations of these metals over longer timescales. .. Nutrient concentrations remained mostly below detection limit (PO_4^{3-}, $NO_3^- + NO_2^-$), or low and within typical coastal ranges (NH_4^+, SiO_2, Garcia et al., 2019; Mallin et al., 2005) (Supplementary Material).

Carbonate system parameters were not significantly impacted on placement days and fluctuated substantially month-to-month post-deployment with ranges similar to other long-term studies of coastal North Carolina (Johnson et al., 2013) and the larger Mid-Atlantic Bight (Xu et al., 2020, Wright-Fairbanks et al., 2020). Even after decoupling the freshwater signal, no OAE-induced alkalinity signal could be resolved (Supplementary Material). Similarly, month-to-month alkalinity variation remained consistent with other studies after salinity normalization (Supplementary Material). Taken together, these findings suggest that the carbonate system was not significantly impacted by the olivine deployment on either short or long timescales and observed changes were instead driven by natural variability. Importantly, the lack of observable signal in carbonate system parameters expected from olivine dissolution does not preclude olivine dissolution, but may be due to rapid dilution in this energetic environment and the relatively small deployment size.

Ultimately, no measurable impacts were observed in biological responses. No consistent changes were detected in chlorophyll-*a*, phytoplankton pigments (including fucoxanthin), or dissolved oxygen (Fig. 5). A transient chlorophyll-*a* increase during one placement remained within natural variability and could not be distinguished from physical drivers such as advection or mixing (Rippy et al., 2013), while later seasonal peaks are likely linked to regional bloom dynamics rather than the deployment. For example, chlorophyll-*a* peaked on 15 October 2024, outside the pre- and immediate post-deployment periods. This peak is likely driven by natural variability (e.g., currents, phytoplankton blooms, and advection from Chesapeake Bay), as it showed no correlation with carbonate chemistry, nutrients, or trace metals. A phytoplankton bloom was reported in Chesapeake Bay a few days earlier (CoastWatch, 2025), and prevailing hydrodynamic conditions suggest southward transport of chlorophyll-rich waters toward the study site. Oxygen concentrations remained within typical coastal ranges both during placements and post-deployment, indicating no bloom-driven respiration or hypoxia (Fusi et al., 2023). Together, these findings indicate that neither turbidity-induced light limitation nor metal release resulted in phytoplankton bloom stimulation, one of the key ecological risk associated with OAE (Dai et al., 2023; Hutchins et al., 2023; Guo et al., 2024).

In addition, the project placement generated transient seasurface foam, representing a previously underexplored impact for mineral-based OAE. Foam may influence ecosystems in ways analogous to turbidity, including reducing light penetration and physically affecting pelagic organisms and filter feeders. The foam likely resulted from hydrophobic minerals within the feedstock (e.g., talc and serpentine) interacting with entrained air during placement, creating conditions similar to mineral flotation processes (Bazar et al., 2021; Wani et al., 2024). The mineralogical composition of discrete foam samples supports this interpretation (Supplementary Material). The foam was not detectable in satellite imagery the following day after deployment as it moved with prevailing currents (Supplementary Material). Foam formation should be explicitly incorporated into future OAE risk assessment, mitigation, and monitoring strategies.

Taken together, these results show that observable impacts were restricted to short-lived physical disturbance and minor, transient chemical signals, while no downstream ecological or biogeochemical effects were detected within, or adjacent to, the project area. Olivine addition projects at this scale, conducted in energetic coastal conditions, appear to pose limited environmental risk for the water column ecosystem. An important limitation of the study was the limited baseline characterization of discrete environmental parameters, for which only one pre-deployment survey was available. This was primarily due to logistical and operational constraints (e.g., acquisition of permit) that restricted opportunities for earlier field sampling. Consequently, the available baseline data does not fully capture natural temporal variability for discrete parameters in particular, limiting our ability to distinguish potential deployment-related changes in these parameters from background fluctuations. Future mERW field trials should prioritize multiple pre-deployment surveys, ideally covering different seasons and environmental conditions, to establish a more representative empirical baseline and strengthen the attribution of observed changes to treatment effects.

4.2. Carbon Dioxide Removal Impact

4.2.1. CDR model evaluation & in-situ olivine dissolution rates

The trace metal signals observed during the field trial provide a rare opportunity to evaluate whether olivine dissolution in a dynamic water column aligns with established laboratory dissolution kinetics. The statistically significant increase in Ni and Co concentrations for Impact samples, relative to Baseline samples, indicates that olivine dissolution began immediately upon placement, however the magnitude of these signals suggests that reactivity in the field is more complex than canonical dissolution rates.

The measured water column Ni and Co concentrations for Impact samples were higher (3-7 times higher for Ni, 4-9 times higher for Co) than those predicted by the model using literature-based olivine dissolution rates (Rimstidt et al., 2012). There is experimental precedent for initial dissolution rates up to an order of magnitude higher than the steady state due to surface roughness, mineral defects, and/or the presence of highly reactive fine-grained dust coating larger grains that is not accounted for in grain size analyses (Fuhr et al., 2022). In particular, the treatment of surface roughness, defined as the ratio of BET to geometric surface area, is a key uncertainty. Empirical measurements of the feedstock's BET surface area would likely be misleading because clay minerals within a feedstock can substantially increase BET surface area (Fisher et al., 2023) while contributing minimally to the CDR potential. The bulk feedstock in this trial consisted of 7.2 wt% clays, while the 0-45 µm size fraction consisted of 41.9 wt% clays (Supplementary Material). However, applying a literature-average roughness factor for forsterite of ~5 (compiled from 22 studies, Rimstidt et al., 2012) would largely reconcile modeled results with observed trace metal concentrations.

Additionally, the discrepancy between the relative concentrations of Ni and Co (3-7x versus 4-9x, respectively) predicted by the model relative to the field data suggests the possibility of secondary adsorption/desorption processes and/or the dissolution of other minerals besides olivine in the feedstock with different elemental stoichiometry (e.g. serpentine, pyroxene). In either case, this highlights a complication with the use of trace metal concentrations as a quantitative tracer of olivine dissolution.

Alkalinity concentrations for water column Impact samples were not statistically different from Baseline samples. Nevertheless, the model predicts that olivine dissolution will result in an alkalinity increase of 27-38 µmol kg^{-1} when a surface roughness factor of 5 is applied. Broadly consistent with this, the placement day analysis showed that the mean alkalinity concentration for the Impact group was higher than Baseline by approximately this magnitude, particularly for salinity-normalized alkalinity (26.3 µmol kg^{-1} higher). Nevertheless, the lack of statistical significance highlights the need for higher sample counts to improve conclusions regarding alkalinity production from olivine dissolution.

Despite these nuances, we find that our model is consistent with field observations particularly in the context of evidence for high initial dissolution rates of similar material (e.g., Fuhr et al., 2022). While our findings suggest that the application of a surface roughness factor may therefore be appropriate in modeling that seeks to predict initial (hours to days) olivine dissolution in field trials, we emphasize that this choice may not be appropriate for longer timescale dissolution (10s to 100s of years) (Fuhr et al., 2022). In such modeling below, we revert to the more traditional and conservative approach and leverage the dissolution rate of Rimstidt (2012).

4.2.2. Model sensitivity analysis and CDR potential

A central challenge for OAE approaches that rely on minerals such as olivine is that fine-grained suspended material dissolves over annual to decadal timelines and basin-scale domains, rendering near-field observations insufficient to constrain true carbon removal potential. To resolve this, it is necessary to move beyond kinetic modeling and evaluate feedstock dissolution within the context of competing environmental and hydrodynamic uncertainties. Here, our CDR model was used to examine the sensitivity of long-term gross carbon dioxide removal outcomes from the field trial under a range of scenarios including varying temperature, pH, and physical transport regimes (Table 1, Supplementary Material). Our results quantify a distinct hierarchy of controls, geochemical and physical, that determine the magnitude and timing of CDR from suspended material. In parallel, we examine how project design choices, particularly deployment location, influence these outcomes and overall carbon removal efficiency.

Table 1 Summary of model scenario configurations and results.

Scenario	Initial seawater temperature (C); warming rate (C yr^{-1})	Initial seawater pH (pH units); acidification rate (pH units yr^{-1})	Grain size thresholds for feedstock suspension (µm)	Portion of feedstock suspended (tonne); (%)	Dissolved olivine (tonne)	Time to full olivine dissolution (year)	CDR in 20 years (tonne CO_2)	Lifetime CDR (tonne CO_2)
1: Default	15.8; 0.049	8.04; -0.0059	111	2579; 27	2100	173	516	1788

2	15.8; 0.049	8.04; -0.0059	111	2579; 27	19	0.4	16	16
3	15.8; 0.049	8.04; -0.0059	76	1189; 12	887	139	319	755
4a	15.8; 0.049	8.04; -0.0059	42	435; 5	244	95	166	208
4b	15.8; 0.049	8.04; -0.0059	138	3772; 39	3140	194	646	2674

A default scenario (Scenario 1) was configured that assumed all suspended feedstock remained in the nearshore surface ocean and was subject to typical physical transport (e.g., sheer velocity) and geochemical (i.e., mean annual pH and temperature) conditions at the field site. Geochemical conditions were projected over long-term timescales using IPCC business-as-usual rates of ocean warming and acidification (Fox-Kemper et al., 2021). In this scenario, the sediment transport module predicted a suspension threshold grain size of 111 µm and a washload threshold of 76 µm. The mass of grains below the suspension threshold equated to approximately 27% of the feedstock. These model results were consistent with bathymetric survey estimates indicating that 22–28% of the released material was not retained within the mapped berm footprints and was assumed therefore to be transported away from the site in suspension (Supplementary Material). The bathymetry-derived estimate was used only as an order-of-magnitude comparison with the modeled suspended fraction, rather than as a quantitative estimate of the suspended sediment plume. The model results were also consistent with post-placement field samples in which suspended sediments exhibited D_{50} values ≤74 µm, while seafloor sediments had a D_{50} of ~200 µm (Supplementary Material). With 27% of the feedstock suspended, the geochemical module predicted that nearly one third of the suspended olivine will dissolve in the first 20 years with complete dissolution in 173 years, ultimately resulting in 1788 tonnes CO_2 removed (Figure 7). Geochemical sensitivity analyses revealed initial geochemical conditions (namely temperature and pH) are much more impactful than future rates of ocean warming and acidification in determining total dissolution timescales and CDR potential (Supplementary Material).

However, favorable geochemical conditions alone are insufficient to maximize CDR efficiency if the physical transport regime removes feedstock from the ocean's surface mixed layer (Burger et al., 2026). In Scenario 2, the transport module simulated cross-shore transport, which resulted in entrainment of suspended material into the Gulf Stream and sinking into deeper waters after several months (Supplementary Material), effectively halting carbon removal on relevant timescales. This truncated time limited CDR to 16 tonnes (Figure 7A, inset). Such rapid sinking and subduction effectively decouples mineral dissolution from atmospheric exchange, as the resulting alkalinity is generated in deeper water masses that may require timescales of global ocean ventilation (i.e., 1,000 to 2,000 years; Broecker et al., 1984) to ultimately remove atmospheric CO_2. This highlights a critical geographic constraint for OAE with minerals characterized by longer dissolution timelines such as olivine: deployment of minerals in regions characterized by short surface residence times (on the order of decades or less) should be avoided to ensure that alkalinity production can meaningfully contribute to atmospheric CO_2 drawdown.

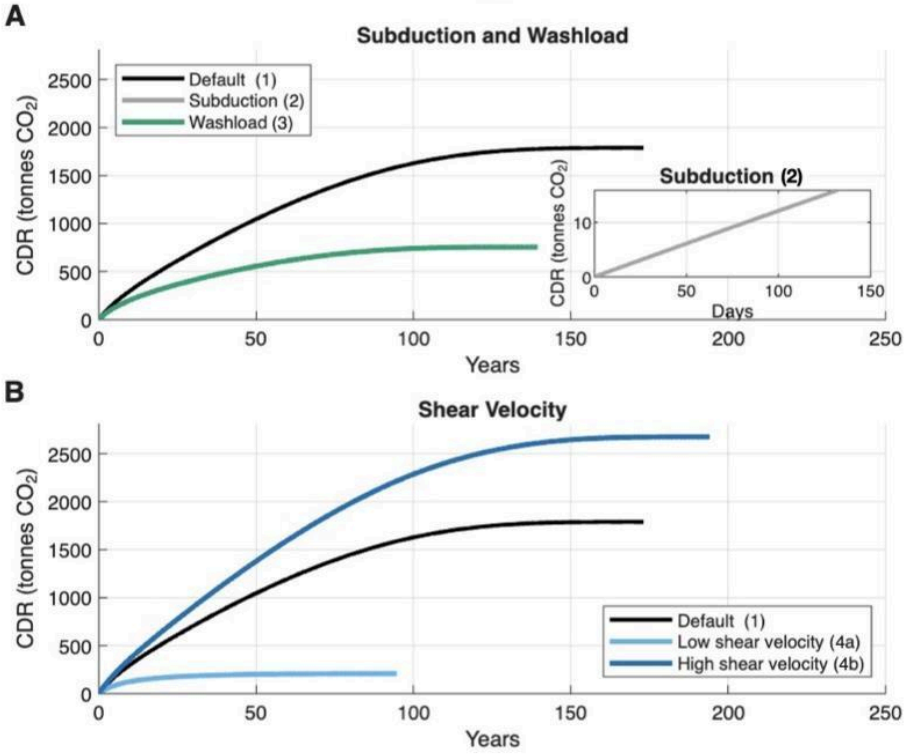


Figure 7. Sensitivity analysis of coupled sediment transport and geochemical modeling, assessing geochemical and physical influences on CDR potential. Abbreviated scenario descriptions and scenario numbers in legends.

In contrast to the default scenario, Scenario 3 examined the effect of only considering the washload as suspended. The bedload fraction, which transports along the seafloor, was excluded from dissolution. This scenario resulted in only 12% of the total feedstock suspended long-term, rather than 27% in the default scenario. Here, 887 tonnes of olivine dissolved and removed just 755 tonnes of CO_2 over its lifetime (Figure 7A). This underscores the importance of rigorously defining which mineral particles are subject to seawater (versus sediment) geochemical conditions in mineral dissolution and CDR quantification models.

Additionally, the sensitivity of CDR outcomes to variation in shear velocity was explored by using the 10th and 90th percentile shear velocity values recorded at the field site throughout 2024 to represent plausible upper and lower bounds. Low shear velocity (Scenario 4a) restricted the suspended fraction to the finest grain sizes, limiting total dissolution to 5% of the deployed material. Conversely, high shear velocity (Scenario 4b) permitted the suspension of coarser fractions, increasing the total mass available for water column dissolution to 39% of the total deployment. This resulted in substantial differences in CDR potential; the high shear velocity scenario produced 1186% more CDR than the low shear velocity over the lifetime of the suspended material (Figure 7B). This demonstrates the importance of accurately resolving hydrodynamic conditions for CDR quantification, yet also illustrates a critical challenge as conditions vary substantially across spatial and temporal scales. Future work should prioritize the development of monitoring and modeling approaches capable of resolving the transport pathways of suspended material on the timescales relevant to the dissolution of those particles. Overall, results from Scenarios 2 and 4 indicate that the duration of particle suspension is a more impactful determinant of

CDR efficiency than geochemical conditions (i.e., seawater temperature and pH; Scenario 1 and geochemical sensitivity analyses (Supplementary Material)).

Finally, the sensitivity to particle fate presents an important trade-off for OAE deployment design. Under more energetic hydrodynamic conditions, coarser grains can remain suspended, reducing the need for intensive feedstock grinding which may provide cost and emission-related advantages. However, higher-energy environments may also enhance transport rates, reducing particle fate predictability, increasing monitoring complexity and cost, and increasing uncertainty on CDR quantification which could lead to fewer verifiable carbon credits. Conversely, lower-energy environments may provide longer residence times and improved monitoring capability, but require finer feedstock to achieve comparable suspended fractions. These constraints on particle transport should therefore be explicitly considered when aligning site selection and deployment design with objectives such as rigorous and quantifiable MRV, optimized techno-economic analysis, and carbon credit maximization.

4.3. Implications for Measurement, Reporting and Verification (MRV) Protocols

Robust MRV methodologies are essential for ensuring that CDR claims from mineral-based OAE are rigorously quantifiable (Halloran et al., 2025; Ho et al., 2023). Our study highlights several monitoring and modeling approaches that can support MRV development for the suspended fraction of mineral-based OAE. Although focused on olivine, these approaches are broadly applicable to other mineral feedstocks and systems that may generate secondary mineral phases in the water column (e.g. brucite) (Ringham et al., 2024; Varliero et al., 2024) and provide a framework for considering chemical and physical processes at timescales relevant to feedstock dissolution rates.

A key finding of this study is that robust baselines are essential for distinguishing OAE-driven changes from natural variability. Baseline monitoring should capture seasonal and interannual variability, particularly for alkalinity and dissolved trace metals that are rarely included in conventional coastal monitoring programs, and include sufficient temporal coverage for robust statistical analysis. Longer pre-deployment monitoring and additional pre-placement samples would have improved characterization of background variability and fine-scale heterogeneity in this study. While high-resolution sampling improves characterization of background conditions, its practicality is limited. We therefore recommend prioritizing targeted discrete measurements supported by autonomous sensors to improve spatio-temporal coverage. Control stations also provide a means of distinguishing OAE-driven changes from natural variability, and although the control stations in this study did not show statistically significant differences relative to the olivine station, they should remain an important component of monitoring design, and should be selected a priori based on predicted sediment transport pathways that can be guided by modeling or tracer experiments (Subhas et al., 2025).

In this study, feedstock mass was estimated from stockpile volume derived from aerial imagery, which is sensitive to assumptions regarding pile geometry, compaction, image resolution, material properties and loss of material during handling. These uncertainties could be reduced through direct mass accounting (e.g. vessel displacement), or by combining high-resolution aerial photogrammetry with discrete sampling. Characterizing the suspended feedstock was challenging due to plume heterogeneity and changing hydrodynamic conditions. A combined approach using aerial imagery, bathymetric surveys, fixed and mobile sondes, and discrete seawater samples proved effective. Future monitoring would benefit from expanded autonomous and spatially distributed observations, including multiple fixed sensor arrays (Stewart, 2025), drifting buoys (Subhas et al., 2025), UAVs and satellite imagery (Lu et al.,

2021), dye tracers (Subhas et al., 2025), backscatter measurements (Balch et al., 2009; Morris et al., 2024) and co-located sampling devices to improve temporal alignment between measurements.

Resolving post-release partitioning between deposited and suspended sediment requires both field observations and modeling. In this study, modeled suspended sediment mass and cumulative CDR were highly sensitive to hydrodynamic conditions. Bathymetric surveys and discrete water samples provided partial validation, but observations alone were insufficient to resolve transient sediment dynamics. Numerical modeling of hydrodynamics and sediment transport are therefore essential for predicting plume transport, informing monitoring design, supporting adaptive sampling during deployment, and interpolating sparse post-deployment observations. Such numerical modeling paired with biogeochemical models for predicting water chemistry changes should play a key role in MRV for mineral-based OAE. They can be used a priori to predict suspended sediment concentrations, plume transport and water chemistry changes under representative deployment and hydrodynamic scenarios. The results can be used to inform sampling duration, cadence, spatial coverage, and control-site selection. During deployment, near-real-time modeling can support adaptive monitoring by predicting plume trajectories and guiding sampling. Post-deployment, models constrained by field observations can interpolate sparse measurements and predict particle transport, fate, and associated CDR processes relevant to environmental impact assessment and carbon removal accounting. These results highlight the need for integrated sediment and geochemical modeling along with field-based approaches for MRV.

Seawater samples were used to characterize suspended material and water chemistry for carbon removal estimates and assessment of environmental impacts. Sampling design should reflect plume extent, monitoring duration, and analytical requirements but is often constrained by field sampling capacity and time-sensitive processing. Monitoring is typically limited by the time consuming nature of collecting and processing discrete samples, and these limitations will continue to hinder rigorous field-based quantification of OAE deployments until new technology is developed. These limitations highlight the need for more sensor-based MRV methodologies. Trace metal monitoring would benefit from development of sensors specific for elements such as Ni, which is common in OAE feedstocks (e.g. olivine, brucite, steel slag), occur at low natural concentrations in seawater, and was detectable in the water column in this study. An Ni-specific sensor would allow for orders of magnitude higher frequency sampling compared to discrete measurements. Such sensors exist for the detection of iron in marine environments (Liu et al., 2023). Emerging alkalinity sensors (Briggs et al., 2017) could improve the statistical robustness of carbon-removal quantification by providing alkalinity measurements at much higher temporal resolution than is possible with discrete samples.

Post-deployment monitoring is essential for detecting delayed or long-term responses to mineral addition and requires high temporal resolution to distinguish effects from natural variability. In this study, high-energy conditions limited continuous measurements (e.g. anchored water quality sonde) resulting in reliance on monthly vessel-based sampling that limited detection of feedstock-driven effects. This highlights the need for more robust (e.g. bottom mounted sensors) or autonomous monitoring systems.

4.4. Conclusions

Overall, the deployment of 9645 tonnes of ground olivine-rich feedstock off the coast of Duck, North Carolina resulted in 2379 tonnes of suspended sediment, with the remaining 7266 tonnes deposited on the seafloor as nearshore berms. Due to the significant fraction of feedstock that was transported as

suspended sediment (estimated 25% of total material), this reservoir should not be overlooked in assessing project outcomes. Suspended sediment can drive fundamentally different environmental impacts from deposited sediment, and experience radically different geochemical conditions and physical transport processes which influence its carbon removal potential. Thus, the two reservoirs of material should be considered separately when assessing the outcomes of mineral-based OAE projects.

Here, the field trial produced no measurable adverse water quality impacts during project placement or in the following nine months. Ni and Co concentrations, trace metals found in olivine, temporarily increased in the water column on placement days but remained well below EPA water quality guidelines. Moving forward, environmental responses are likely to vary with project scale and local hydrodynamic conditions and as such, rigorous short- and long-term environmental monitoring is nevertheless essential. Although this study was not designed to quantify phytoplankton community responses, future trials should incorporate metagenomic and taxonomic approaches to better assess ecological effects.

Measurable increases in water column Ni and Co concentrations on feedstock placement days provided evidence for immediate in-situ olivine dissolution and therefore a unique opportunity to assess the applicability of laboratory-derived olivine dissolution rates under field conditions, a major uncertainty in OAE modeling. We developed a coupled sediment transport and geochemical model to estimate trace metal release and carbon removal from the suspended sediment fraction of the field trial. When the model was configured for placement days, we found that modeled Ni, Co, and alkalinity concentrations largely agreed with measured water column values after applying a grain surface roughness factor of 5 to literature-derived, steady-state olivine dissolution rates. This provides evidence of olivine dissolution rates higher than canonical rates in the immediate hours after placement, consistent with published laboratory studies.

Finally, because suspended olivine is expected to dissolve over annual to decadal timescales, during which time it can be transported across basin (or larger) spatial scales, the model was run to estimate carbon removal from the suspended sediment fraction of the field trial over these spatiotemporal scales. Assuming average, site-specific hydrodynamic conditions, geochemical conditions, and a long-term air-sea gas exchange efficiency factor, as well as IPCC business-as-usual ocean warming and acidification rates, the model suggested that the suspended fraction could remove approximately 516 tonnes of CO_2 (gross removal) in the first 20 years post-deployment, contributing to a total CDR potential of approximately 1788 tonnes of gross carbon removal over its estimated 173 year lifetime, equivalent to 0.69 tonnes CO_2/tonnes suspended sediment. However, sensitivity analyses demonstrated that the CDR potential can vary dramatically depending on the physical transport conditions and that uncertainty in these conditions play an outsized role in CDR outcomes, as compared to uncertainty in geochemical conditions. Rigorous carbon removal quantification will require modeling capable of resolving sediment transport pathways and particle residence time in the surface ocean. Overall, this study provides a practical framework for monitoring suspended fractions of future mineral-based OAE deployments and supports the development of rigorous MRV protocols for such projects.

Acknowledgements

The authors would like to acknowledge Vesta, PBC, as well as their coastal engineering partner, Coastal Protection Engineering, for development of the field trial including design, permitting, and build. We thank Matthew Balazik from the USACE for his support during placement day monitoring. From the USACE Field Research Facility and Engineering with Nature, we thank Patrick Dickhudt, Michael Forte, Nicholas Cohn, Justin Shawler, Robert Mitchell, and Christopher Thoburn for their invaluable support in

establishing the field monitoring program and executing the fieldwork. We thank Sean Charles and Hannah Sirianni from the Coastal Studies Institute for their assistance collecting images by drone during the project build. The authors thank the following researchers for their helpful discussions and insight on carbonate chemistry: Professor Andrew Dickson, Dr. Ellen Briggs, Dr. Abby Lunstrum, Nick Rollins, and Professor Will Berelson. We thank Evan Goldstein from Sediment for providing Instagrain analyses. We thank Ted Conroy, Bonnie Chang, Marcus Garland, Matthew Casari, Grace Schellinger, and April Eason for their support in methodology, field sample collection, and sample processing. Finally, we thank the Town of Duck, NC for their support of the field trial. The text of this article was edited by Claude version 1.26832.0 (056ee2).

Funding Statement

This work was funded by the Grantham Foundation for the Protection of the Environment, awarded to Hourglass Climate.

References

Bach, L.T., Gill, S.J., Rickaby, R.E., Gore, S., and Renforth, P. (2019). CO2 removal with enhanced weathering and ocean alkalinity enhancement: potential risks and co-benefits for marine pelagic ecosystems. *Front. Clim.* 1:476698.

Bach, L.T. (2024). The additionality problem of ocean alkalinity enhancement. *Biogeosciences* 21, 261–277.

Balch, W.M., Plueddemann, A.J., Bowler, B.C., and Drapeau, D.T. (2009). Chalk-Ex—fate of CaCO3 particles in the mixed layer: evolution of patch optical properties. *J. Geophys. Res. Oceans* 114:C7.

Bazar, J.A., Rahimi, M., Fathinia, S., Jafari, M., Chipakwe, V., and Chehreh Chelgani, S. (2021). Talc flotation—an overview. *Minerals* 11:662.

Biological and Chemical Oceanography Data Management Office (BCO-DMO) (2024). Hydrologic data from field sampling sites in the Neuse River Estuary, Pamlico Sound, and Onslow Bay in the coastal North Atlantic offshore from North Carolina (USA) in 2021 and 2022. Dataset version 1. Available at: https://www.bco-dmo.org/dataset/935794

Bertagni, M.B., and Porporato, A. (2022). The carbon-capture efficiency of natural water alkalinization: implications for enhanced weathering. *Sci. Total Environ.* 838:156524. doi: 10.1016/j.scitotenv.2022.156524

Bopp, L., Resplandy, L., Orr, J.C., Doney, S.C., Dunne, J.P., Gehlen, M., et al. (2013). Multiple stressors of ocean ecosystems in the 21st century: projections with CMIP5 models. *Biogeosciences* 10, 6225–6245.

Briggs, E.M., Sandoval, S., Erten, A., Takeshita, Y., Kummel, A.C., and Martz, T.R. (2017). Solid state sensor for simultaneous measurement of total alkalinity and pH of seawater. *ACS Sens.* 2, 1302–1309.

Broecker, W.S., Mix, A., Andrée, M., and Oeschger, H. (1984). Radiocarbon measurements on coexisting benthic and planktonic foraminifera shells: potential for reconstructing ocean ventilation times over the past 20,000 years. *Nucl. Instrum. Methods Phys. Res. B* 5, 331–339.

Burger, F.A., Hofmann Elizondo, U., Grosselindemann, H., and Frölicher, T.L. (2026). Subsurface dissolution reduces the efficiency of mineral-based open-ocean alkalinity enhancement. *Biogeosciences* 23, 3279–3298.

Churakova, Y., Aguilera, A., Charalampous, E., Conley, D.J., Lundin, D., Pinhassi, J., et al. (2023). Biogenic silica accumulation in picoeukaryotes: novel players in the marine silica cycle. *Environ. Microbiol. Rep.* 15, 282–290.

CoastWatch (2025). Chesapeake and Delaware Bays satellite data. Available at: https://eastcoast.coastwatch.noaa.gov/region_cd.php#dmv (Accessed November 18, 2025).

Dai, M., Zhao, Y., Chai, F., Chen, M., Chen, N., Chen, Y., et al. (2023). Persistent eutrophication and hypoxia in the coastal ocean. *Cambridge Prisms Coast. Futures* 1:e19.

Dickson, A.G., and Millero, F.J. (1987). A comparison of the equilibrium constants for the dissociation of carbonic acid in seawater media. *Deep Sea Res. Part A* 34, 1733–1743.

Dickson, A.G., Afghan, J.D., and Anderson, G.C. (2003). Reference materials for oceanic CO2 analysis: a method for the certification of total alkalinity. *Mar. Chem.* 80, 185–197.

Douglas, N.K., and Byrne, R.H. (2017). Achieving accurate spectrophotometric pH measurements using unpurified meta-cresol purple. *Mar. Chem.* 190, 66–72.

Feng, E.Y., Koeve, W., Keller, D.P., and Oschlies, A. (2017). Model-based assessment of the CO2 sequestration potential of coastal ocean alkalinization. *Earth's Future* 5, 1252–1266.

Ferderer, A., Schulz, K.G., Riebesell, U., Baker, K.G., Chase, Z., and Bach, L.T. (2024). Investigating the effect of silicate- and calcium-based ocean alkalinity enhancement on diatom silicification. *Biogeosciences* 21, 2777–2794.

Fisher, B.A., Yoo, K., Aufdenkampe, A.K., Naer, E.A., Feinberg, J.M., and Nyquist, J.E. (2023). Mineral surface area in deep weathering profiles reveals the interrelationship of iron oxidation and silicate weathering. *Earth Surf. Dyn.* 11, 51–69.

Flipkens, G., Blust, R., and Town, R.M. (2021). Deriving nickel (Ni(II)) and chromium (Cr(III)) based environmentally safe olivine guidelines for coastal enhanced silicate weathering. *Environ. Sci. Technol.* 55, 12362–12371.

Fox-Kemper, B., Hewitt, H.T., Xiao, C., Aðalgeirsdóttir, G., Drijfhout, S.S., Edwards, T.L., et al. (2021). "Ocean, cryosphere and sea level change," in *Climate Change 2021: The Physical Science Basis. Contribution of Working Group I to the Sixth Assessment Report of the Intergovernmental Panel on Climate Change*, eds. V. Masson-Delmotte, P. Zhai, A. Pirani, S.L. Connors, C. Péan, et al. (Cambridge, United Kingdom and New York, NY, USA: Cambridge University Press), 1211–1362. doi: 10.1017/9781009157896.011

Fuhr, M., Geilert, S., Schmidt, M., Liebetrau, V., Vogt, C., Ledwig, B., et al. (2022). Kinetics of olivine weathering in seawater: an experimental study. *Front. Clim.* 4:831587.

Fusi, M., Rigaud, S., Guadagnini, G., Barausse, A., Marasco, R., Daffonchio, D., et al. (2023). Ideas and perspectives: the fluctuating nature of oxygen shapes the ecology of aquatic habitats and their biogeochemical cycles—the aquatic oxyscape. *Biogeosciences Discuss.* 2023, 1–33.

Garcia, H.E., Weathers, K.W., Paver, C.R., Smolyar, I., Boyer, T.P., Locarnini, R.A., et al. (2019). *World Ocean Atlas 2018, Volume 4: Dissolved Inorganic Nutrients (Phosphate, Nitrate and Nitrate+Nitrite, Silicate)*. NOAA Atlas NESDIS 84. Silver Spring, MD: NOAA.

Geerts, L.J., Hylén, A., and Meysman, F.J. (2025). Review and syntheses: ocean alkalinity enhancement and carbon dioxide removal through marine enhanced rock weathering using olivine. *Biogeosciences* 22, 355–384.

Glueck, D., and Schubert, H. (2024). "Suspended particle dynamics during sand nourishments and storm events: a comparative analysis," in *Sediment Transport Research – Further Recent Advances* (IntechOpen).

Guo, J.A., Strzepek, R.F., Swadling, K.M., Townsend, A.T., and Bach, L.T. (2024). Influence of ocean alkalinity enhancement with olivine or steel slag on a coastal plankton community in Tasmania. *Biogeosciences* 21, 2335–2354.

Halloran, P.R., Bell, T.G., Burt, W.J., Chu, S.N., Gill, S., Henderson, C., et al. (2025). Seawater carbonate chemistry based carbon dioxide removal: towards commonly agreed principles for carbon monitoring, reporting, and verification. *Front. Clim.* 7:1487138.

Hangx, S.J.T., and Spiers, C.J. (2009). Coastal spreading of olivine to control atmospheric CO2 concentrations: a critical analysis of viability. *Int. J. Greenhouse Gas Control* 3, 757–767.

Hansson, I. (1972). *An Analytical Approach to the Carbonate System in Sea Water*. Ph.D. thesis, University of Gothenburg, Sweden.

Hansson, I. (1973). A new set of pH-scales and standard buffers for sea water. *Deep-Sea Res.* 20, 479–491.

Hashim, M.S., Marx, L., Klein, F., Dean, C.L., Burdige, E., Hayden, M., et al. (2025). Mineral formation during shipboard ocean alkalinity enhancement experiments in the North Atlantic. *Biogeosciences* 22, 7149–7165.

Hatje, V., Payne, T.E., Hill, D.M., McOrist, G., Birch, G.F., and Szymczak, R.J.E.I. (2003). Kinetics of trace element uptake and release by particles in estuarine waters: effects of pH, salinity, and particle loading. *Environ. Int.* 29, 619–629.

Hauck, J., Köhler, P., Wolf-Gladrow, D., and Völker, C. (2016). Iron fertilisation and century-scale effects of open ocean dissolution of olivine in a simulated CO2 removal experiment. *Environ. Res. Lett.* 11:024007.

Ho, D.T., Bopp, L., Palter, J.B., Long, M.C., Boyd, P., Neukermans, G., et al. (2023). Monitoring, reporting, and verification for ocean alkalinity enhancement. *State Planet Discuss.* 2023, 1–15.

Hutchins, D.A., Fu, F.X., Yang, S.C., John, S.G., Romaniello, S.J., Andrews, M.G., et al. (2023). Responses of globally important phytoplankton species to olivine dissolution products and implications for carbon dioxide removal via ocean alkalinity enhancement. *Biogeosciences* 20, 4669–4682.

Johnson, Z.I., Wheeler, B.J., Blinebry, S.K., Carlson, C.M., Ward, C.S., and Hunt, D.E. (2013). Dramatic variability of the carbonate system at a temperate coastal ocean site (Beaufort, North Carolina, USA) is regulated by physical and biogeochemical processes on multiple timescales. *PLoS ONE* 8:12.

Kaufman, L., and Rousseeuw, P.J. (2009). *Finding Groups in Data: An Introduction to Cluster Analysis*. Hoboken, NJ: John Wiley & Sons.

Kheshgi, H.S. (1995). Sequestering atmospheric carbon dioxide by increasing ocean alkalinity. *Energy* 20, 915–922.

Komar, P.D. (2007). The entrainment, transport and sorting of heavy minerals by waves and currents. *Dev. Sedimentol.* 58, 3–48.

Lasaga, A.C. (1984). Chemical kinetics of water-rock interactions. *J. Geophys. Res.* 89, 4009–4025.

Lewis, E., and Wallace, D. (1998). Program developed for CO2 system calculations. *Environmental System Science Data Infrastructure for a Virtual Ecosystem.*

Liu, Y., Lu, H., and Cui, Y. (2023). A review of marine in situ sensors and biosensors. *J. Mar. Sci. Eng.* 11:1469.

Lu, Q., Si, W., Wei, L., Li, Z., Xia, Z., Ye, S., and Xia, Y. (2021). Retrieval of water quality from UAV-borne hyperspectral imagery: a comparative study of machine learning algorithms. *Remote Sens.* 13:3928.

Maciel, F.P., Haakonsson, S., Ponce de León, L., Bonilla, S., and Pedocchi, F. (2023). Challenges for chlorophyll-a remote sensing in a highly variable turbidity estuary, an implementation with sentinel-2. *Geocarto Int.* 38:2160017.

Mallin, M.A., Cahoon, L.B., and Durako, M.J. (2005). Contrasting food-web support bases for adjoining river-influenced and non-river influenced continental shelf ecosystems. *Estuar. Coast. Shelf Sci.* 62, 55–62.

Mehrbach, C., Culberson, C.H., Hawley, J.E., and Pytkowicz, R.M. (1973). Measurement of the apparent dissociation constants of carbonic acid in seawater at atmospheric pressure. *Limnol. Oceanogr.* 18, 897–907.

Meysman, F.J., and Montserrat, F. (2017). Negative CO2 emissions via enhanced silicate weathering in coastal environments. *Biol. Lett.* 13:20160905.

Michaelowa, A., Shishlov, I., Hoch, S., Bofill, P., and Espelage, A. (2019). *Overview and Comparison of Existing Carbon Crediting Schemes*. Helsinki: Nordic Environment Finance Corporation (NEFCO).

Middelburg, J.J., Soetaert, K., and Hagens, M. (2020). Ocean alkalinity, buffering and biogeochemical processes. *Rev. Geophys*. 58, 1-28.

Montserrat, F., Renforth, P., Hartmann, J., Leermakers, M., Knops, P., and Meysman, F.J. (2017). Olivine dissolution in seawater: implications for CO2 sequestration through enhanced weathering in coastal environments. *Environ. Sci. Technol.* 51, 3960–3972.

Moras, C.A., Bach, L.T., Cyronak, T., Joannes-Boyau, R., and Schulz, K.G. (2022). Ocean alkalinity enhancement—avoiding runaway CaCO3 precipitation during quick and hydrated lime dissolution. *Biogeosciences* 19, 3537–3557.

Morris, J.T., McDowell, S.E., Pinckard, N.C., Fredette, T.J., and Kincaid, C.R. (2024). "Monitoring of sediment plumes generated by the subaqueous disposal of dredged material" [Conference presentation]. 25th Annual WEDA Conference, Tampa, FL, United States. Available at:

https://westerndredging.org/index.php/education-portal/presentations-library/126-dredging-summit-expo-s/47-2024-conference-in-tampa-fl/49-25th-annual-weda-conference?download=414:1-morris-monitoring-of-sediment-plumes-generated-by-the-subaqueous-disposal-of-dredged-material

National Academies of Sciences, Engineering, and Medicine (NASEM) (2019). *Negative Emissions Technologies and Reliable Sequestration: A Research Agenda*. Washington, DC: The National Academies Press. doi: 10.17226/25259

National Academies of Sciences, Engineering, and Medicine (NASEM) (2022). "Ocean alkalinity enhancement," in *A Research Strategy for Ocean-Based Carbon Dioxide Removal and Sequestration* (Washington, DC: The National Academies Press). doi: 10.17226/26278

Nichols, M.M., Thompson, G.S., and Faas, R.W. (1978). *A Field Study of Fluid Mud Dredged Material: Its Physical Nature and Dispersal*. Technical Report D-78-40. Vicksburg, MS: U.S. Army Engineer Waterways Experiment Station.

Olsen, A.A., and Rimstidt, J.D. (2007). Using a mineral lifetime diagram to evaluate the persistence of olivine on Mars. *Am. Mineral.* 92, 598–602.

Orr, J.C., Epitalon, J.-M., Dickson, A.G., and Gattuso, J.-P. (2018). Routine uncertainty propagation for the marine carbon dioxide system. *Mar. Chem.* 207, 84–107.

Oze, C., Bird, D.K., and Fendorf, S. (2007). Genesis of hexavalent chromium from natural sources in soil and groundwater. *Proc. Natl. Acad. Sci. U.S.A.* 104, 6544–6549.

Palmiéri, J., and Yool, A. (2024). Global-scale evaluation of coastal ocean alkalinity enhancement in a fully coupled Earth system model. *Earth's Future* 12:e2023EF004018.

Pit, I.R., Dekker, S.C., Kanters, T.J., Wassen, M.J., and Griffioen, J. (2017). Mobilisation of toxic trace elements under various beach nourishments. *Environ. Pollut.* 231, 1063–1074.

R Core Team (2022). *R: A Language and Environment for Statistical Computing*. Vienna, Austria: R Foundation for Statistical Computing. Available at: https://www.R-project.org/

Ramasamy, M., Amann, T., and Moosdorf, N. (2024). Regional potential of coastal ocean alkalinization with olivine within 100 years. *Environ. Res. Lett.* 19:064030.

Rickert, D. (2000). *Dissolution Kinetics of Biogenic Silica in Marine Environments = Lösungskinetik von Biogenem Opal in Marinen Systemen*. Ph.D. thesis. Berichte zur Polarforschung (Reports on Polar Research) 351.

Rimstidt, J.D., Brantley, S.L., and Olsen, A.A. (2012). Systematic review of forsterite dissolution rate data. *Geochim. Cosmochim. Acta* 99, 159–178.

Ringham, M.C., Hirtle, N., Shaw, C., Lu, X., Herndon, J., Carter, B.R., et al. (2024). An assessment of ocean alkalinity enhancement using aqueous hydroxides: kinetics, efficiency, and precipitation thresholds. *Biogeosciences* 21, 3551–3570. doi: 10.5194/bg-21-3551-2024

Rippy, M.A., Franks, P.J.S., Feddersen, F., Guza, R.T., and Warrick, J.A. (2013). Beach nourishment impacts on bacteriological water quality and phytoplankton bloom dynamics. *Environ. Sci. Technol.* 47, 6146–6154. doi: 10.1021/es400572k

Ritchie, R.J. (2008). Universal chlorophyll equations for estimating chlorophylls a, b, c, and d and total chlorophylls in natural assemblages of photosynthetic organisms using acetone, methanol, or ethanol solvents. *Photosynthetica* 46, 115–126.

Roman-Sierra, J., Navarro, M., Muñoz-Perez, J.J., and Gomez-Pina, G. (2011). Turbidity and other effects resulting from Trafalgar sandbank dredging and Palmar beach nourishment. *J. Waterw. Port Coast. Ocean Eng.* 137, 332–343.

Rouse, H. (1937). Modern conceptions of the mechanics of fluid turbulence. *Trans. Am. Soc. Civ. Eng.* 102, 463–541.

Sharp, J.D., Pierrot, D., Humphreys, M.P., Epitalon, J.-M., Orr, J.C., Lewis, E.R., et al. (2023). CO2SYSv3 for MATLAB (Version v3.2.1). Zenodo. doi: 10.5281/zenodo.3950562

Sharples, J., Moore, M.C., Rippeth, T.P., Holligan, P.M., Hydes, D.J., Fisher, N.R., et al. (2001). Phytoplankton distribution and survival in the thermocline. *Limnol. Oceanogr.* 46, 486–496.

Shih, C.H., Kuo, Y.Y., Chu, T.J., Chou, W.C., Chang, W.T., and Lee, Y.C. (2011). Eco-environmental impact assessment of pre-leisure beach nourishment on the benthic invertebrate community at Anping coast. *China Ocean Eng.* 25, 215–236.

Soulsby, R.L. (1997). *Dynamics of Marine Sands*. London: Thomas Telford.

Soulsby, R.L., and Whitehouse, R.J. (1997). "Threshold of sediment motion in coastal environments," in *Pacific Coasts and Ports '97: Proceedings of the 13th Australasian Coastal and Ocean Engineering Conference and the 6th Australasian Port and Harbour Conference*, Vol. 1 (Christchurch, NZ: University of Canterbury), 145–150.

Stewart, T., Regier, P., Hinson, K., Torrez Sanchez, C., Mackay, Q., Ward, N.D., et al. (2025). Assessing the limitations of commercial sensors and models for supporting marine carbon dioxide removal (mCDR) monitoring: a case study. *Front. Clim.* 7:1649723.

Subhas, A.V., Rheuban, J.E., Wang, Z.A., McCorkle, D.C., Michel, A.P., Marx, L., et al. (2025). A tracer study for the development of in-water monitoring, reporting, and verification (MRV) of ship-based ocean alkalinity enhancement. *Biogeosciences* 22, 5511–5534.

Tréguer, P.J., and De La Rocha, C.L. (2013). The world ocean silica cycle. *Annu. Rev. Mar. Sci.* 5, 477–501.

U.S. Army Corps of Engineers (USACE) (2001a). *The New York District's Biological Monitoring Program for the Atlantic Coast of New Jersey, Asbury Park to Manasquan Section Beach Erosion Control Project*. Final report. Vicksburg, MS: Waterways Experiment Station.

Varliero, S., Buono, A., Caserini, S., Raos, G., and Macchi, P. (2024). Chemical aspect of ocean liming for CO2 removal: dissolution kinetics of calcium hydroxide in seawater. *ACS Eng. Au* 4:4, 422-431.

van Dolah, R.F., Martore, R.M., Lynch, A.E., Levisen, M.V., Wendt, P.H., Whitaker, D.J., et al. (1994). *Final Report: Environmental Evaluation of the Folly Beach Nourishment Project*. Charleston, SC: U.S. Army Corps of Engineers, Charleston District.

van Rijn, L.C. (1984a). Sediment transport, part I: bed load transport. *J. Hydraul. Eng.* 110, 1431–1456.

van Rijn, L.C. (1984b). Sediment transport, part II: suspended load transport. *J. Hydraul. Eng.* 110, 1613–1641.

Warrick, J.A., Stevens, A.W., and Tehranirad, B. (2025). Coastal fine-grained sediment plumes from beach nourishment near Santa Barbara, California. *Coast. Eng. J.* 1–25.

Wang, L.J., Fan, Y., Parsons, R.L., Hu, G.R., Zhang, P.Y., and Li, F.L. (2018). A rapid method for the determination of fucoxanthin in diatom. *Mar. Drugs* 16:33.

Wani, O.B., Khan, S., Shoaib, M., da Costa Gonçalves, C., Chen, Z., Zeng, H., et al. (2024). Processing of low-grade ultramafic nickel ores: a critical review. *Miner. Eng.* 218:108976.

Wentworth, C.K. (1922). A scale of grade and class terms for clastic sediments. *J. Geol.* 30, 377–392.

Wright-Fairbanks, E.K., Miles, T.N., Cai, W., Chen, B., and Saba, G.K. (2020). Autonomous observation of seasonal carbonate chemistry dynamics in the Mid-Atlantic Bight. *JGR Oceans* 125:11.

Xu, Y., Cai, W., Wanninkhof, R., Salisbury, J., Reimer, J., and Chen, B. (2020). Long-term changes of carbonate chemistry variables along the North American East Coast. *JGR Oceans* 125:7.

Zhou, M., Tyka, M.D., Ho, D.T., Yankovsky, E., Bachman, S., Nicholas, T., et al. (2025). Mapping the global variation in the efficiency of ocean alkalinity enhancement for carbon dioxide removal. *Nat. Clim. Chang.* 15, 59–65.

Supplementary Material

1 Supplementary Methods & Results 3
1.1 Feedstock Characterization 3
1.1.1 Feedstock Mineralogy 3
1.1.2 Feedstock Grain Size Distribution 4
1.1.3 Feedstock Elemental Composition 5
1.2 Native Sediment Characterization 8
1.2.1 Native Sediment Mineralogy 8
1.2.2 Native Sediment Grain Size Distribution 9
1.2.3 Native Sediment Elemental Composition 10
1.3 Post-Deployment Seafloor Sediment Grain Size Distribution 12
1.4 Total Suspended Sediment Mineralogy and Grain Size Distribution 13
1.5 Surface Foam Mineralogy and Grain Size Distribution 18
1.6 Field Trial Monitoring 21
1.6.1 Mixed Layer Statistical Analysis 22
1.6.2 Statistical Analysis of Pre- & Post-Deployment Monitoring Station Differentiation 23
1.6.3 Oceanographic Conditions During Placements 24
1.6.4 Water Quality Monitoring 25
1.6.4.1 Fixed Aquatroll Array Depths 25
1.6.4.2 AquaTROLL 500 Sonde and YSI EXO2 Sonde Parameters 26
1.6.4.3 Water Quality Sampling Locations: Placements 27
1.6.4.4 Water Quality Sampling Locations: Pre- and Post-Deployment 28
1.6.4.5 Detailed Turbidity Data (Fixed Sonde Array) During Placements 29
1.6.4.6 Detailed Turbidity (Mobile Sonde) and TSS Data Summary During Placements 31
1.6.4.7 Detailed Mobile Sonde Water Quality Parameters During Placements 33
1.6.4.8 Detailed Discrete Water Chemistry During Placements 34
1.6.4.9 Detailed Sonde and Discrete Water Chemistry Data Pre- & Post-Deployment 36
1.6.4.10 Reconciliation of Discrete Sample Carbonate System 47
1.6.4.11 Water Quality Guidelines 48
2 CDR Model 49
2.1 Quantification of Suspended Sediment Volume 49
2.2 CDR Model Setup and Validation 53
2.2.1 Sediment Motion Threshold Module 53
2.2.1.1 Motion Threshold Model Equations 53
2.2.1.2 Motion Threshold Parameterization 55
2.2.1.3 Motion Threshold Model Testing 57
2.2.1.4 Mass and Mineralogy of Sediment in Motion 58
2.2.2 Geochemical Module 58
2.2.2.1 Set Up: Model Evaluation and In-situ Olivine Dissolution Rates 58
2.2.2.2 Set Up: Sensitivity Analysis and CDR Potential 59

2.3 Model Evaluation and In-Situ Olivine Dissolution Rates 59
2.4 Sensitivity Analysis and CDR Potential Model Runs 61
2.4.1 Scenario 1 62
2.4.2 Scenario 2 63
2.4.3 Scenario 3 63
2.4.4 Scenario 4 63
3 References 64

1 Supplementary Methods & Results

1.1 Feedstock Characterization

A total of 9,645 tonnes of dunite sand was placed during the field trial, which was mined and ground by Sibelco (Aaheim, Norway). After unloading the material at port in the US, a 70 lb bag of the feedstock material was set aside for characterization. It was subsampled using a Humboldt sediment sample splitter with a 0.25 inch chute width to divide the bulk sediment into smaller, representative portions for analyses. To ensure representative splitting, the chute width was at least three times the diameter of the largest particle in the sample (Gilson, 2024), minimizing the risk of particles bridging or blocking the chutes, which can introduce sampling bias. The diameter of the 99th percentile grain (D99) was used to evaluate whether the selected splitter was appropriate. Since analyses focus on the olivine fraction of the material, the D99 was calculated for the olivine grains. The sample was first sieved to remove particles larger than the D99, ensuring that the material being split was compatible with the splitter chute width. The sieved material was then passed through the sediment splitter repeatedly and an aliquot was sent to QMineral for analysis (see below).

1.1.1 Feedstock Mineralogy

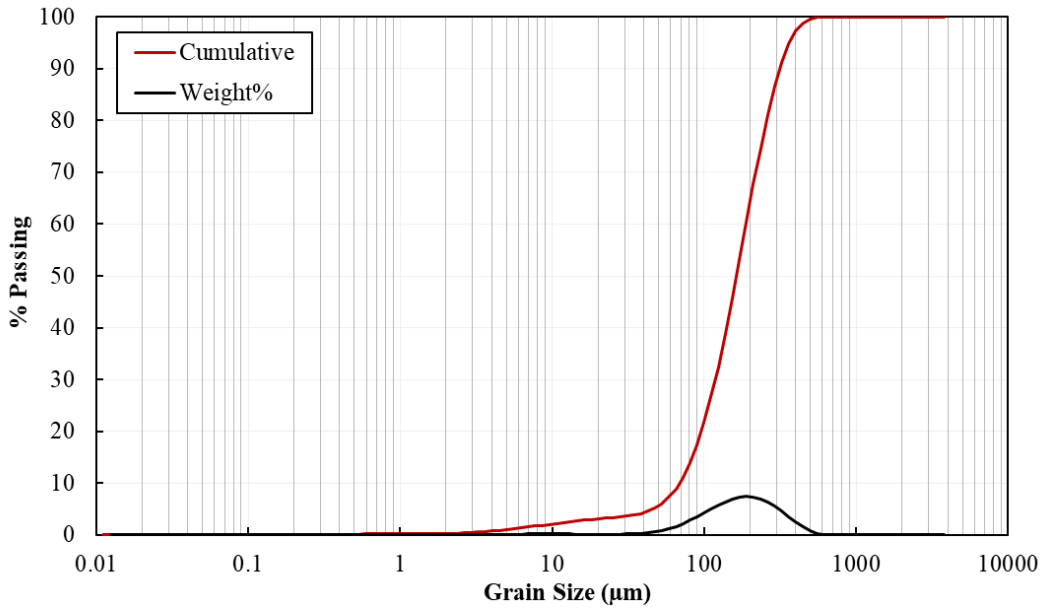
The feedstock was analyzed for mineralogy by X-ray diffraction (XRD) at QMineral (Leuven, Belgium) using a Bruker D8 Advance with XE-T detector and Cu-Kα radiation. The bulk feedstock was characterized, as well as four grain size fractions: 0-45 µm, 45-63 µm, 63-150 µm, and 150-250 µm (Supplementary Table S1). The results showed that feedstock is 88.6 wt% forsterite, 3.2 wt% orthopyroxene, 3.0 wt% chlorite, and 2.3 wt% talc, with minor contributions of 2:1 layer silicates, spinels, and periclase, totaling to 7.2 wt% clays in the bulk feedstock. Of the four grain size bins analyzed separately, only 0-45 µm was distinct from the bulk composition. This fraction contained only 56.1 wt% forsterite with 20.9 wt% serpentine, 12.9 wt% 2:1 layer silicates, 6.3 wt% chlorite, and minor contributions of talc, orthopyroxene, and spinels, totaling to 41.9 wt% clays in this size fraction.

Supplementary Table S1. Mineralogy of bulk feedstock and multiple size fractions.

Mineral	Bulk (wt%)	0-45 µm Fraction (wt%)	45-63 µm Fraction (wt%)	63-150 µm Fraction (wt%)	150-250 µm Fraction (wt%)
Forsterite	88.6	56.1	86.2	87.2	89.8
Orthopyroxene	3.2	1.3	3.4	4.0	3.9
2:1 layer silicates (mica)	1.8	12.9	0.0	0.0	0.0
Chlorite	3.0	6.3	2.4	3.8	3.0
Serpentine	0.0	20.9	2.2	0.0	0.0
Talc	2.3	1.8	3.5	3.1	2.4
Spinel-type minerals	0.8	0.7	2.0	1.4	0.6
Periclase	0.2	0.0	0.3	0.5	0.3
Total non-clays	92.8	58.1	92.0	93.1	94.5
Total clays	7.2	41.9	8.0	6.9	5.5

1.1.2 Feedstock Grain Size Distribution

Grain size analyses were conducted by laser diffraction at QMineral. The feedstock had a median grain size (D_{50}) of 163 µm and a fines content (<62.5 µm) of 8.28% (Supplementary Figure S1). It had a D_{10} of 69 µm and D_{90} of 315 µm.



Supplementary Figure S1. Grain size distribution of the feedstock.

1.1.3 Feedstock Elemental Composition

The elemental composition of the feedstock was determined by Sample Fusion Inductively Coupled Plasma Mass Spectrometry (ICP-MS) at QMineral (Supplementary Table S2). Samples were mixed with a flux of lithium metaborate and lithium tetraborate and fused in an induction furnace. The melts were poured into a solution of 5% nitric acid containing an internal standard, and mixed continuously until completely dissolved. Loss on ignition (LOI) was measured on the fused samples. Measurements were performed using a Thermo Jarrell-Ash ENVIRO II ICP and at least 3 CRM standards were included per measurement batch.

Supplementary Table S2. Elemental composition of the feedstock.

Analyte	wt% or ppm	Detection Limit
SiO2	41.56%	0.01
Al2O3	0.47%	0.01
Fe2O3(T)	7.46%	0.01
MnO	0.10%	0.005
MgO	49.02%	0.01
CaO	0.09%	0.01
Na2O	0.06%	0.01
K2O	0.02%	0.01
TiO2	0.01%	0.001
P2O5	< 0.01%	0.01

LOI	0.07%	-
Sc	5.0 ppm	1
Be	< 1 ppm	1
V	17.0 ppm	5
Ba	9.0 ppm	2
Sr	12.0 ppm	2
Y	1.0 ppm	1
Zr	47.0 ppm	2
Cr	3320.0 ppm	20
Co	119.0 ppm	1
Ni	2810.0 ppm	20
Cu	10.0 ppm	10
Zn	40.0 ppm	30
Ga	< 1 ppm	1
Ge	< 1 ppm	1
As	< 5 ppm	5
Rb	< 2 ppm	2
Nb	< 1 ppm	1
Mo	< 2 ppm	2
Ag	< 0.5 ppm	0.5
In	< 0.2 ppm	0.2
Sn	< 1 ppm	1
Sb	< 0.5 ppm	0.5
Cs	< 0.5 ppm	0.5
La	< 0.2 ppm	0.2
Ce	0.4 ppm	0.1
Pr	< 0.05 ppm	0.05
Nd	0.2 ppm	0.1
Sm	< 0.1 ppm	0.1
Eu	< 0.05 ppm	0.05

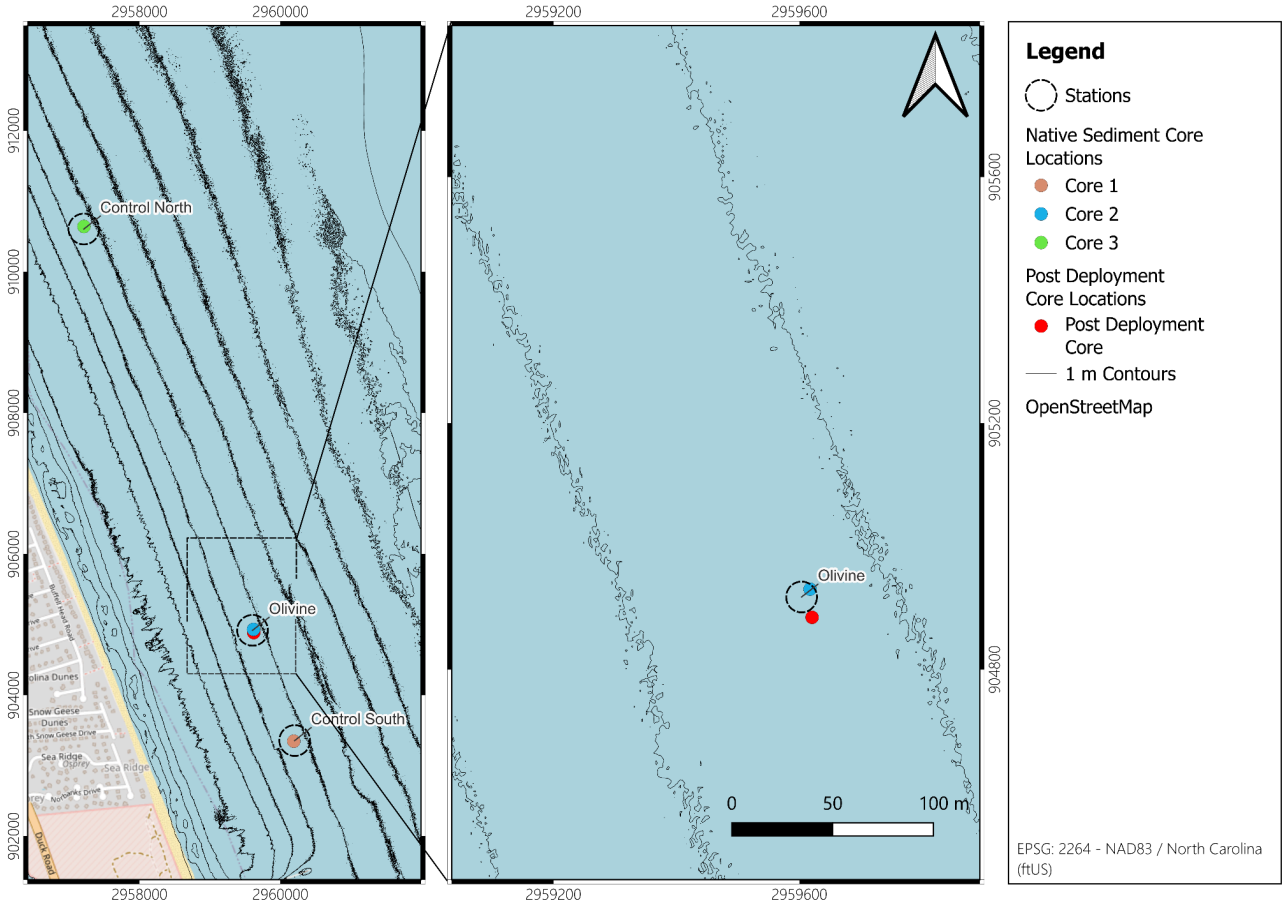
Gd	< 0.1 ppm	0.1
Tb	< 0.1 ppm	0.1
Dy	< 0.1 ppm	0.1
Ho	< 0.1 ppm	0.1
Er	< 0.1 ppm	0.1
Tm	< 0.05 ppm	0.05
Yb	< 0.1 ppm	0.1
Lu	< 0.01 ppm	0.01
Hf	1.0 ppm	0.2
Ta	< 0.1 ppm	0.1
W	< 1 ppm	1
Tl	< 0.1 ppm	0.1
Pb	< 5 ppm	5
Bi	< 0.4 ppm	0.4
Th	< 0.1 ppm	0.1
U	< 0.1 ppm	0.1

1.2 Native Sediment Characterization

1.2.1 Native Sediment Mineralogy

Native sediment mineralogy was characterized from 3 sediment cores collected at the Olivine, Control South, and Control North stations in March and April, 2024 (i.e. prior to feedstock deployment) (Supplementary Figure S2). Cores were subsampled using an incremental sediment core extruder, dried at 60°C, and two sections from each core were analyzed (1-3 cm, 15-20 cm) by X-ray diffraction (XRD) at QMineral (Leuven, Belgium) using a Bruker D8 Advance with XE-T detector and Cu-Kα radiation.

Based on the three cores (6 subsamples), the native sediment was predominantly quartz (76.3 ± 1.8 wt%, 1SE) with 10.7 ± 1.0 wt % (1SE) plagioclase, 5.5 ± 0.4 wt% (1SE) K-feldspar, 4.0 ± 0.2 wt% (1SE) 2:1 layer silicates, 1.0 ± 0.1 wt% (1SE) amphibole, and trace quantities (< 1 wt%) of chlorite, calcite, aragonite, dolomite/ankerite, halite, rutile, anatase, ilmenite, and spinel-type minerals. In sum, 4.7 ± 0.2 wt% (1SE) of the native sediment were clay minerals while 0.8 ± 0.1 wt% (1SE) of the native sediment were carbonate minerals.

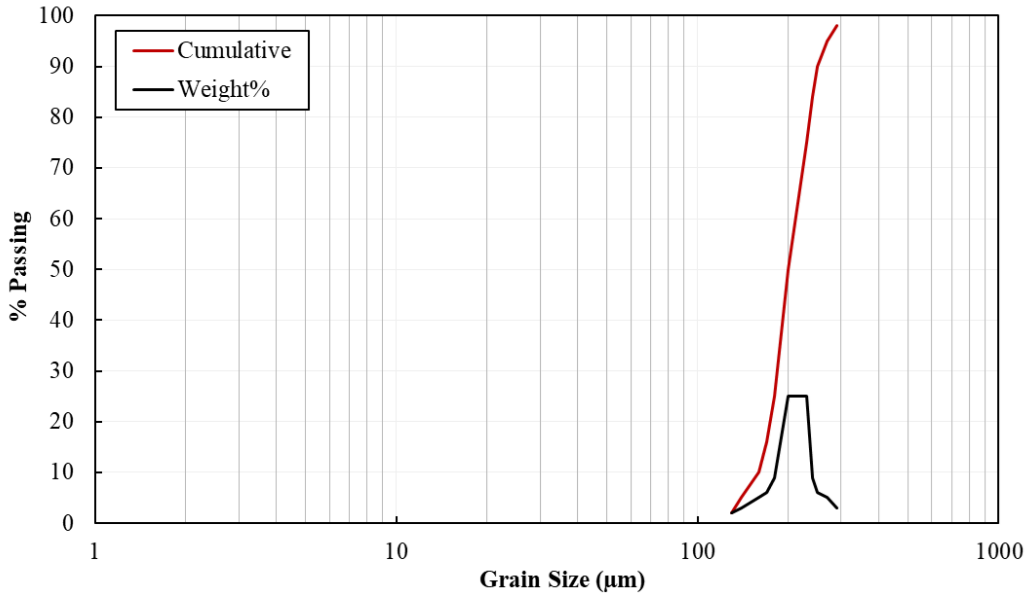


Supplementary Figure S2. Map of native sediment core locations, as well as the post-deployment sediment core location, with monitoring stations (Control North, Control South, and Olivine) given for reference.

1.2.2 Native Sediment Grain Size Distribution

The image-based technology Instagrain (Goldstein et al., 2022) was used to determine the grain size distribution of the native material. The 1-3 cm section of Core 2, located at the Olivine site

(Supplementary Figure S2), was analyzed. The material had a D_{10} of 160 µm, D_{50} of 200 µm and D_{90} of 250 µm (Supplementary Figure S3).



Supplementary Figure S3. Grain size distribution of native sediment at the field site.

1.2.3 Native Sediment Elemental Composition

The elemental composition of the native sediment was determined by Sample Fusion Inductively Coupled Plasma Mass Spectrometry (ICP-MS) at QMineral (Supplementary Table S3). The same sample set was analyzed as described in Supplementary Material Section 1.2.1 for native sediment mineralogy. Samples were mixed with a flux of lithium metaborate and lithium tetraborate and fused in an induction furnace. The melts were poured into a solution of 5% nitric acid containing an internal standard, and mixed continuously until completely dissolved. Loss on ignition (LOI) was measured on the fused samples. Measurements were performed using a Thermo Jarrell-Ash ENVIRO II ICP and at least 3 CRM standards were included per measurement batch.

Supplementary Table S3. Elemental composition of native sediment at the project site.

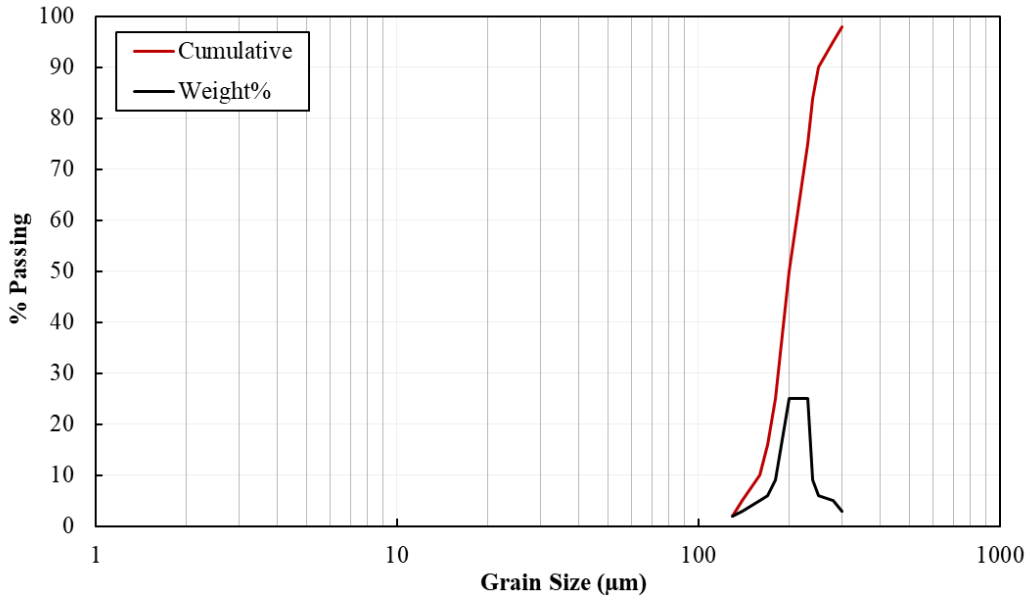
Analyte	wt% or ppm (± 1SE)	Detection Limit
SiO2	87.68 ± 0.94 %	0.01
Al2O3	4.80 ± 0.33 %	0.01
Fe2O3(T)	1.45 ± 0.08%	0.01
MnO	0.025 ± 0.001%	0.005
MgO	0.46 ± 0.03%	0.01
CaO	1.22 ± 0.16%	0.01
Na2O	1.33 ± 0.12%	0.01
K2O	1.19 ± 0.08 %	0.01

TiO2	0.570 ± 0.04%	0.001
P2O5	0.05 ± 0.004%	0.01
LOI	1.9 ± 0.21%	-
Sc	3.0 ± 0.0 ppm	1
Be	< 1 ppm	1
V	22 ± 1.3 ppm	5
Ba	291 ± 15.3 ppm	2
Sr	131 ± 10.5 ppm	2
Y	13 ± 1.5 ppm	1
Zr	837 ± 89.3 ppm	2
Cr	25 ± 2.9 ppm	20
Co	3.0 ± 0.0 ppm	1
Ni	< 20 ppm	20
Cu	30 ± 17 ppm	10
Zn	< 30 ppm	30
Ga	6.0 ± 0.4 ppm	1
Ge	1.0 ± 0.0 ppm	1
As	< 5 ppm	5
Rb	31 ± 2.2 ppm	2
Nb	8.0 ± 0.6 ppm	1
Mo	< 2 ppm	2
Ag	< 0.5 ppm	0.5
In	< 0.2 ppm	0.2
Sn	1.0 ± 0.0 ppm	1
Sb	< 0.5 ppm	0.5
Cs	0.6 ± 0.03 ppm	0.5
La	23.7 ± 4.9 ppm	0.2
Ce	50.4 ± 10.0 ppm	0.1
Pr	6.0 ± 1.1 ppm	0.05
Nd	23.3 ± 4.9 ppm	0.1

Sm	4.4 ± 0.8 ppm	0.1
Eu	0.79 ± 0.09 ppm	0.05
Gd	3.2 ± 0.6 ppm	0.1
Tb	0.5 ± 0.1 ppm	0.1
Dy	2.6 ± 0.4 ppm	0.1
Ho	0.5 ± 0.1 ppm	0.1
Er	1.6 ± 0.2 ppm	0.1
Tm	0.25 ± 0.03 ppm	0.05
Yb	1.7 ± 0.2 ppm	0.1
Lu	0.30 ± 0.04 ppm	0.01
Hf	18.6 ± 1.99 ppm	0.2
Ta	0.6 ± 0.03 ppm	0.1
W	< 1 ppm	1
Tl	0.1 ± 0.02 ppm	0.1
Pb	9.0 ± 0.92 ppm	5
Bi	< 0.4 ppm	0.4
Th	6.3 ± 1.4 ppm	0.1
U	1.6 ± 0.23 ppm	0.1

1.3 Post-Deployment Seafloor Sediment Grain Size Distribution

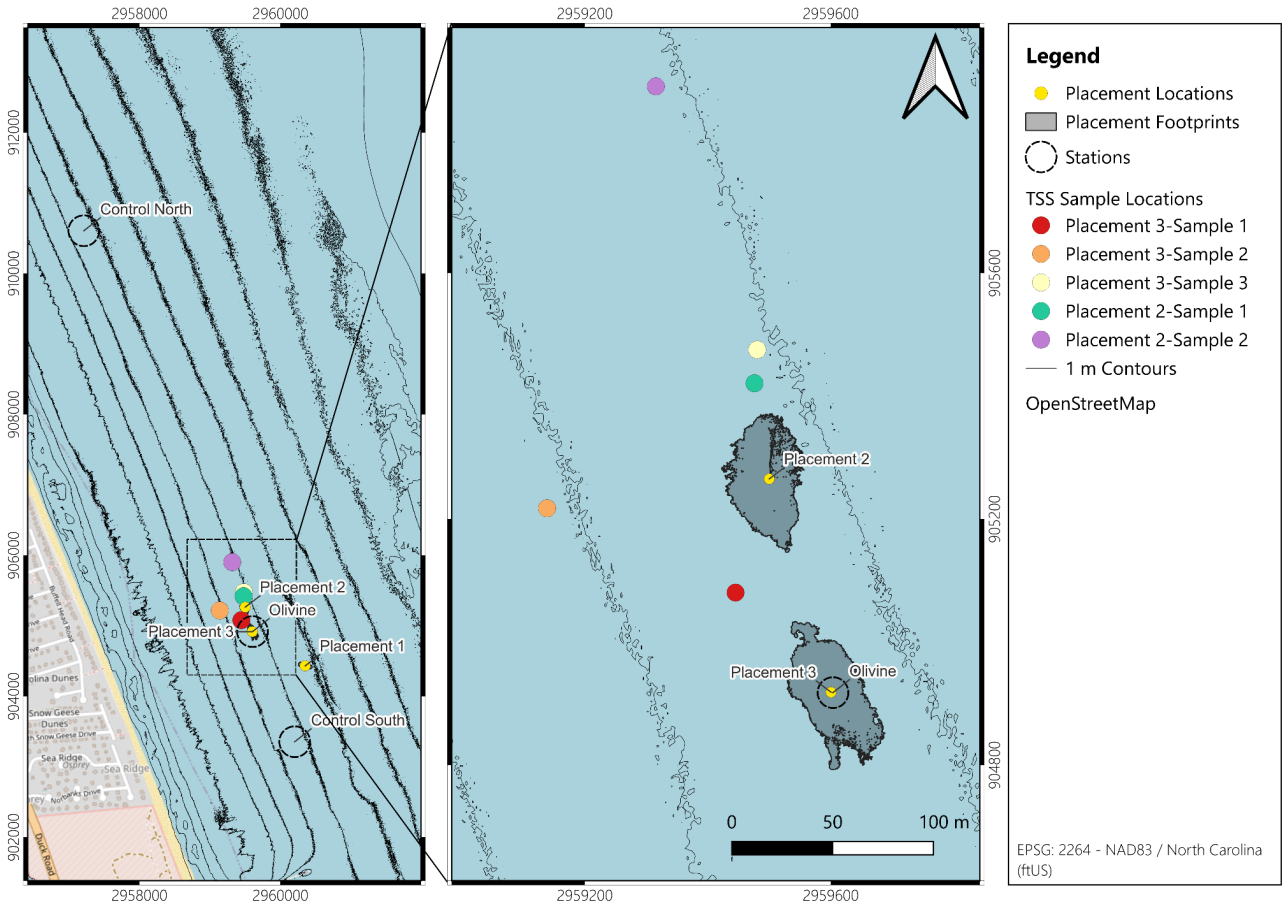
A post-deployment sediment core was collected from the Olivine Station on 8 July 2024 (Supplementary Figure S2). The core was subsampled using an incremental sediment core extruder, dried at 60°C, and the upper 1-3 cm was analysed by Instagrain. The sample had a D_{10} of 160 µm, D_{50} of 200 µm, and D_{90} of 250 µm (Supplementary Figure S4).



Supplementary Figure S4. Grain size distribution of seafloor sediment at the Olivine site post-deployment.

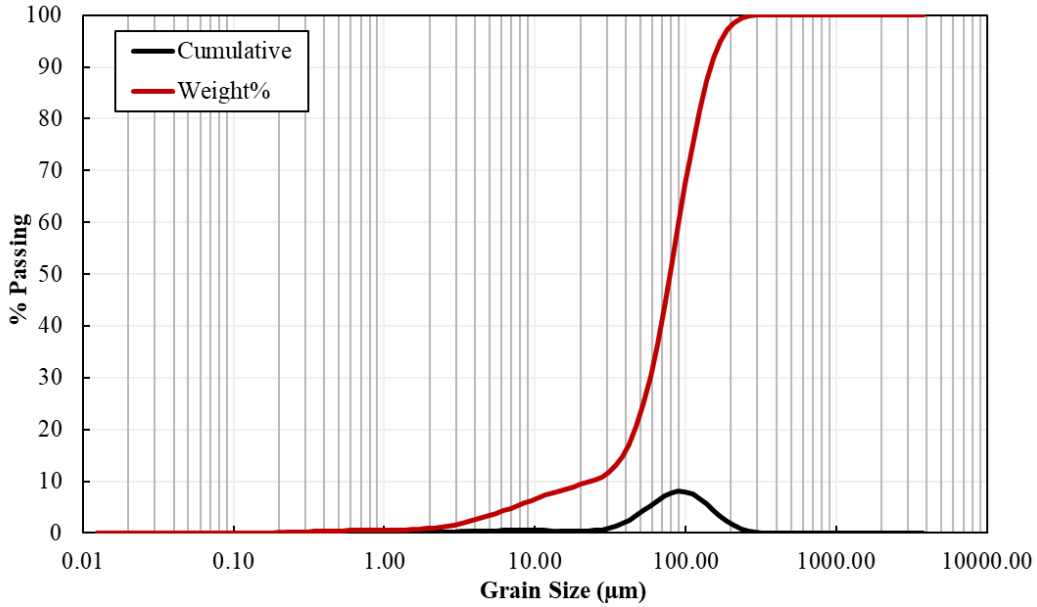
1.4 Total Suspended Sediment Mineralogy and Grain Size Distribution

Five Total Suspended Sediment (TSS) samples were collected from Placement 2 (2 samples) and Placement 3 (3 samples) and characterized for grain size distribution and mineralogy by QMineral (Leuven, Belgium) (Supplementary Figure S5). Grain size was measured by laser diffraction and mineralogy was measured by XRD using a Bruker D8 Advance with XE-T detector and Cu-Kα radiation. Material was challenging to extract from the filters and were of a small quantity, which likely influenced sample representativeness. Consequently, these samples should be considered indicative rather than definitive.



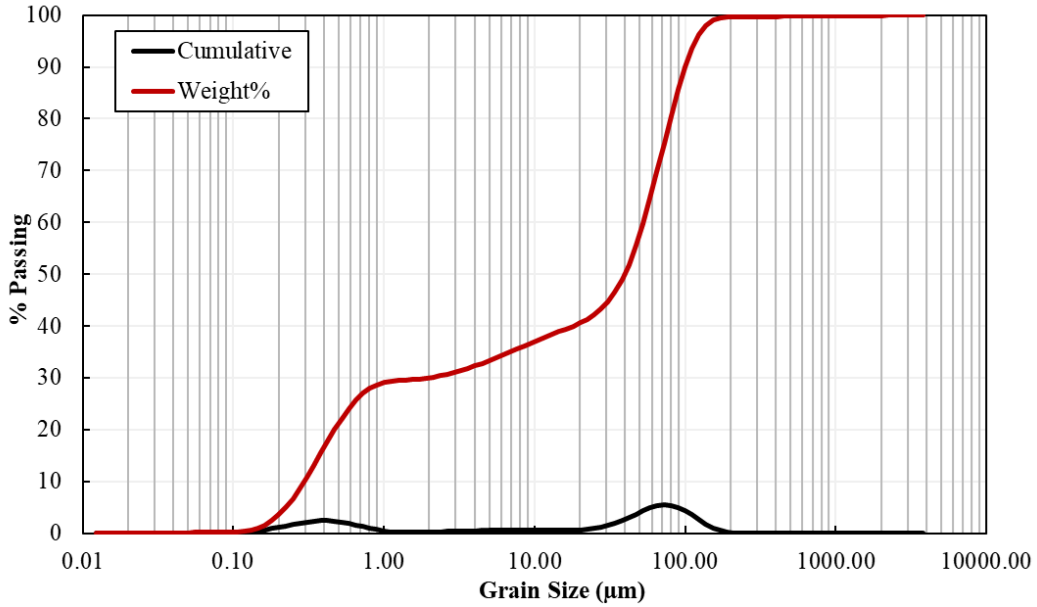
Supplementary Figure S5. Map of TSS sample locations collected during feedstock placement and then analyzed for grain size distribution and mineralogy. Monitoring stations (Control North, Control South, and Olivine) as well as the Placement footprints given for reference.

TSS Placement 3-Sample 1 was collected +18 minutes from feedstock placement at 6.40 m depth and 70 m northwest of the berm (Supplementary Figure S5). It contained 73.7 wt% forsteritic olivine, with 9.1 wt% serpentine, 6.5 wt% talc, 2.7 wt% chlorite, 1.9 wt% mica, 1.8 wt% quartz, 1.8 wt% dolomite, 1.0 wt% plagioclase and minor (< 1 wt%) contributions of K-feldspar, amphibole, and halite. It had the coarsest grain size distribution of the three TSS Placement 3 samples that were analyzed, with a D_{10} of 23 µm, D_{50} of 74 µm and D_{90} of 143 µm (Supplementary Figure S6).



Supplementary Figure S6. Grain size distribution of TSS Placement 3-Sample 1.

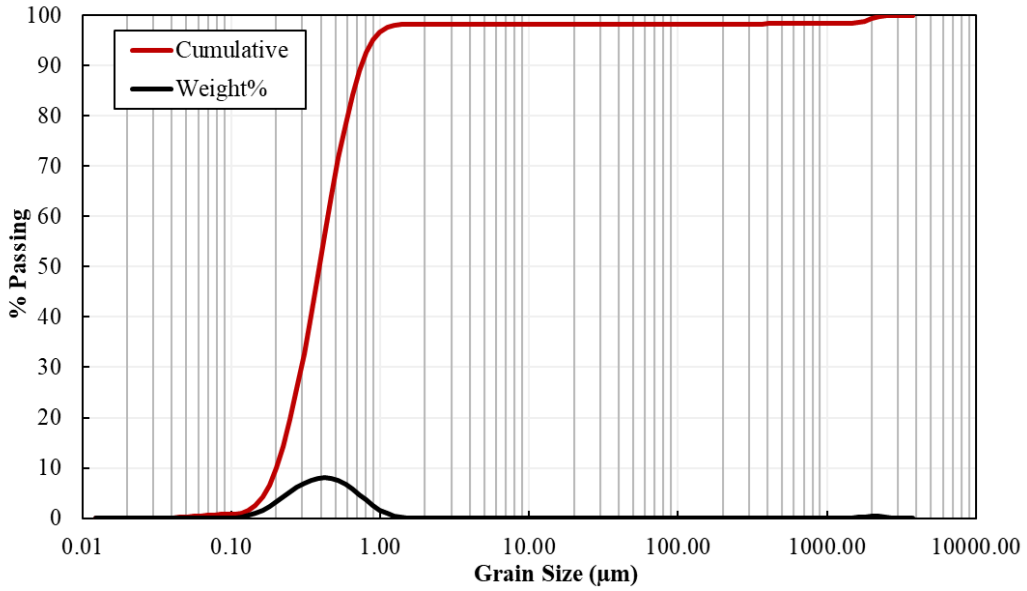
TSS Placement 3-Sample 2 was collected +23 minutes from feedstock placement at 0.91 m depth and 170 m northwest of the berm (Supplementary Figure S5). Similar to TSS Placement 3-Sample 1, the composition was predominantly olivine (67.6 wt%) with 8.7 wt% serpentine, 7.3 wt% chlorite, 5.8 wt% talc, 3.1 wt% calcite, 2.6 wt% dolomite, 2.3 wt% halite, 1.3 wt% quartz and minor (< 1 wt%) contributions of plagioclase, amphibole, and mica. The sample had a D_{50} of 41 µm and was characterised by a bimodal distribution with peaks at 72 µm (5.43%) and 0.38 µm (2.37%). It had a D_{10} of 0.29 µm and D_{90} of 90 µm (Supplementary Figure S7).



Supplementary Figure S7. Grain size distribution of TSS Placement 3-Sample 2.

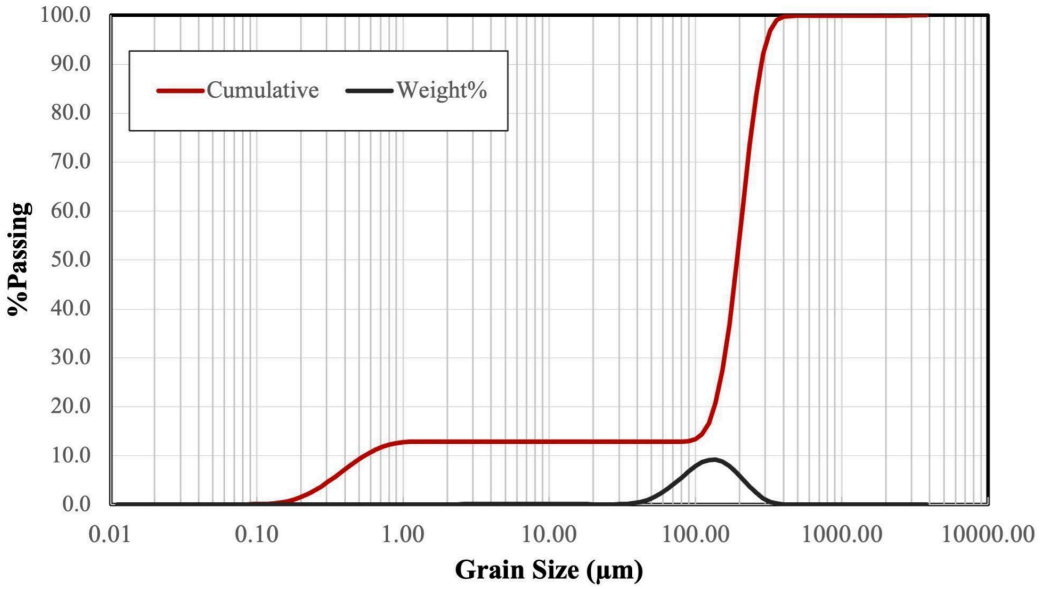
TSS Placement 3-Sample 3 was collected +32 minutes from feedstock placement at 0.91 m and 176 m northwest of the berm (Supplementary Figure S5). The sample was majority olivine (56.8 wt%) with 13.3 wt% quartz, 7.5 wt% plagioclase, 7.3 wt% talc, 4.9 wt% K-feldspar, 4.0 wt% serpentine, 4.0 wt% chlorite, 1.2 wt% dolomite and minor (< 1 wt%) contributions of amphibole,

calcite and halite. The sample had a D_{10} of 0.20 µm, D_{50} of 0.39 µm and D_{90} of 0.75 µm (Supplementary Figure S8).



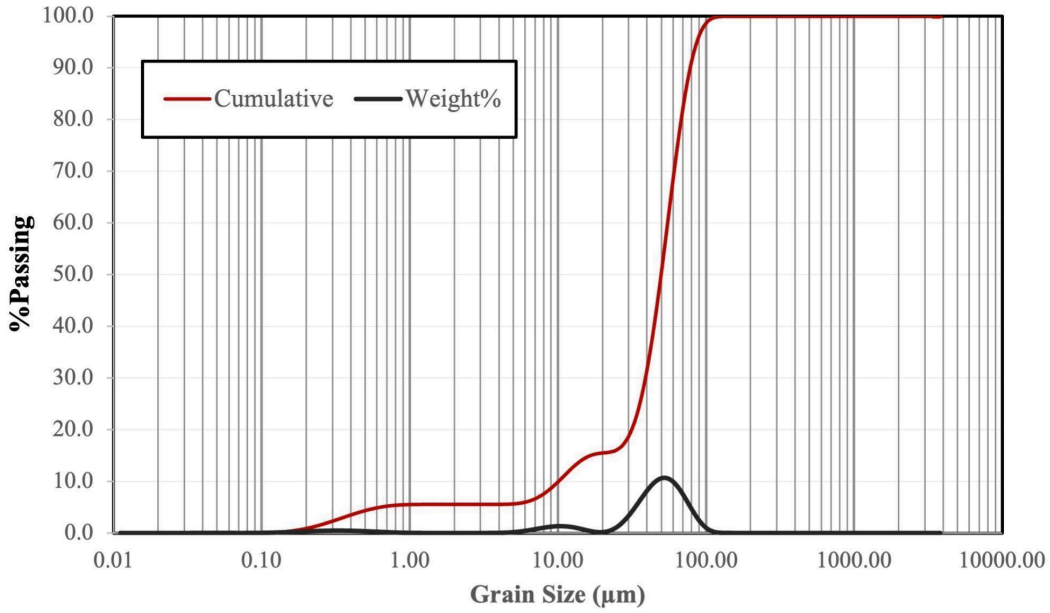
Supplementary Figure S8. Grain size distribution of TSS Placement 3-Sample 3.

TSS Placement 2-Sample 1 was collected +26 minutes from feedstock placement at 5.79 m depth and 16 m north of the berm (Supplementary Figure S5). The composition was predominantly olivine (93.6 wt%) with 1.9 wt% serpentine, 1.0 wt% chlorite, 0.1 wt% talc, 0.1 wt% calcite, 1.0 wt% dolomite, 0.3 wt% halite, 0.3 wt% quartz, 0.6 wt% plagioclase, 1.1 wt% amphibole and negligible contributions of mica. The sample had a D_{50} of 130 µm and was characterised by a singular distribution. It had a D_{10} of 67 µm and D_{90} of 226 µm (Supplementary Figure S9).



Supplementary Figure S9. Grain size distribution of TSS Placement 2-Sample 1.

TSS Placement 2-Sample 2 was collected +32 minutes from feedstock placement at 0.91 m and 172 m northwest of the berm (Supplementary Figure S5). The sample was majority quartz (40.7 wt%) and olivine (33.7 wt%), as well as 10.7 wt% talc, 9.1 wt% mica, 4.4 wt% K-feldspar, and minor (< 1 wt%) contributions of plagioclase, chlorite, calcite, and halite. The sample had a D_{10} of 10 µm, D_{50} of 50 µm and D_{90} of 78 µm (Supplementary Figure S10).



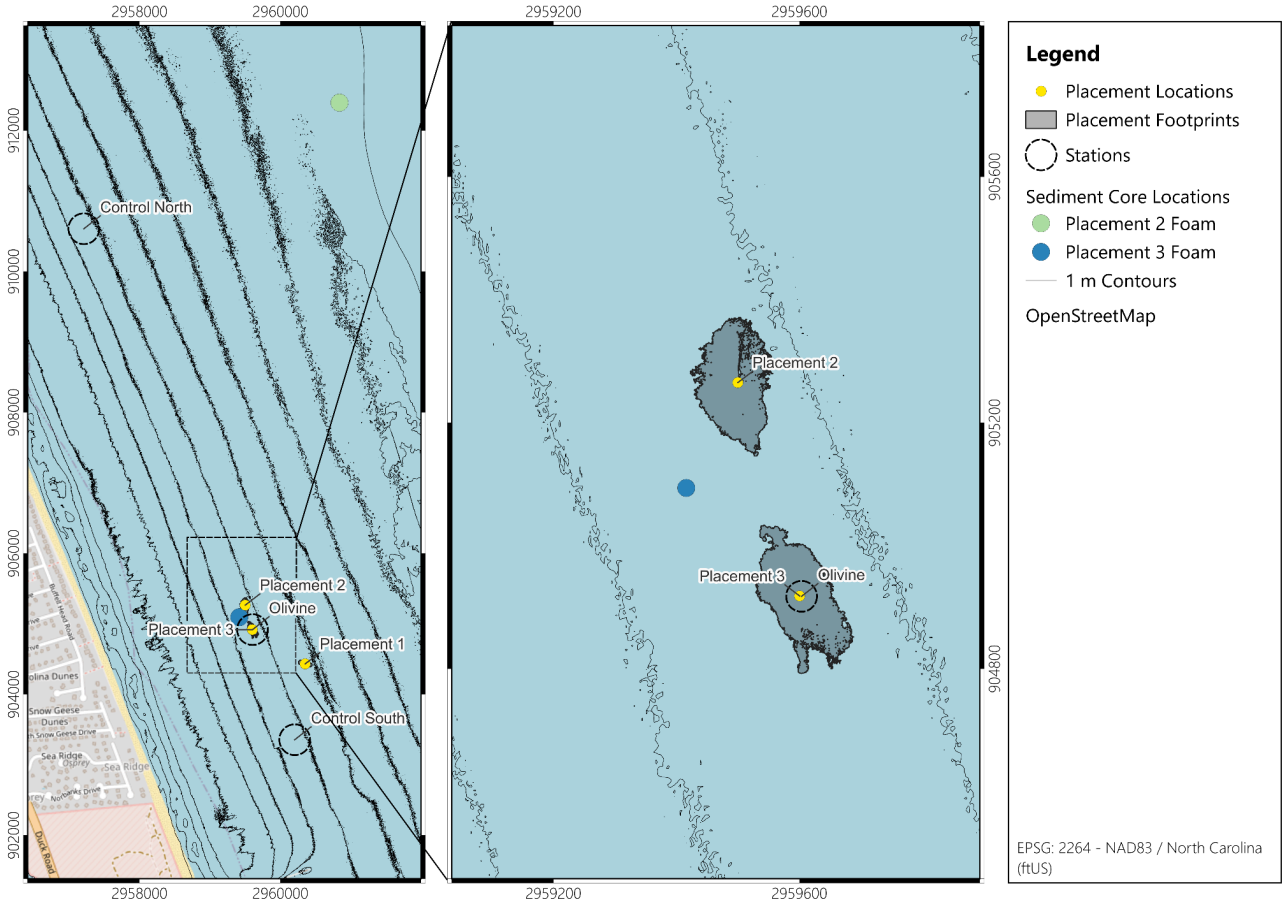
Supplementary Figure S10. Grain size distribution of TSS Placement 2-Sample 2.

1.5 Surface Foam Mineralogy and Grain Size Distribution

Surface foam (Supplementary Figure S11) samples were collected during Placement 2 and 3 (Supplementary Figure S12). Surface foam Sample 1 was collected during Placement 2 and surface foam Sample 2 was collected during Placement 3. The samples were characterized for grain size distribution and mineralogy by QMineral (Leuven, Belgium). Grain size was measured by laser diffraction and mineralogy was measured by XRD using a Bruker D8 Advance with XE-T detector and Cu-Kα radiation. Material was challenging to extract from the filters and were of a small quantity, which likely influenced sample representativeness. Consequently, these samples should be considered indicative rather than definitive.

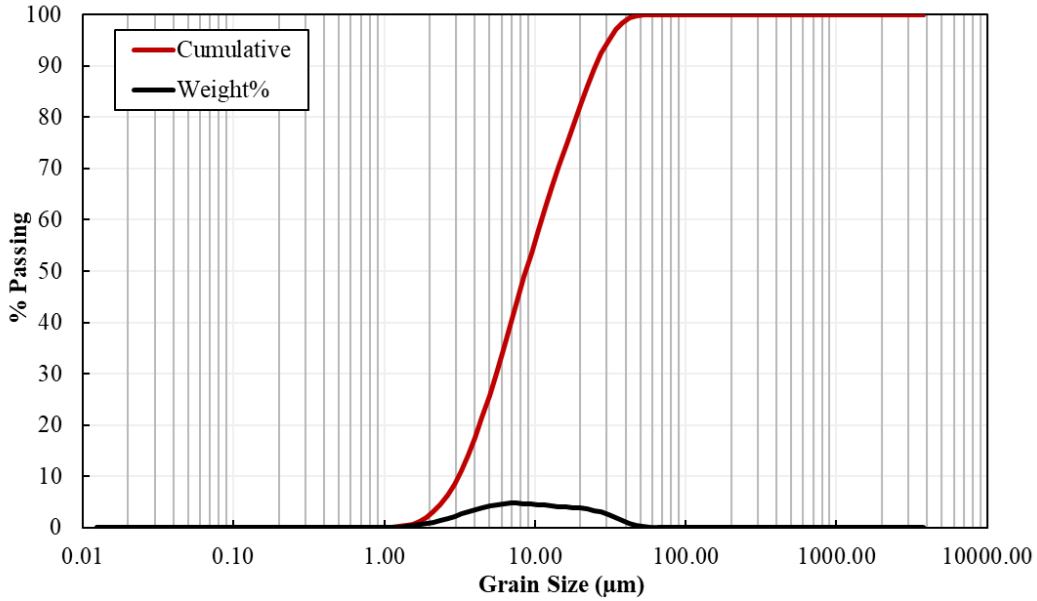


Supplementary Figure S11. Images of surface foam observed during Placement 3.



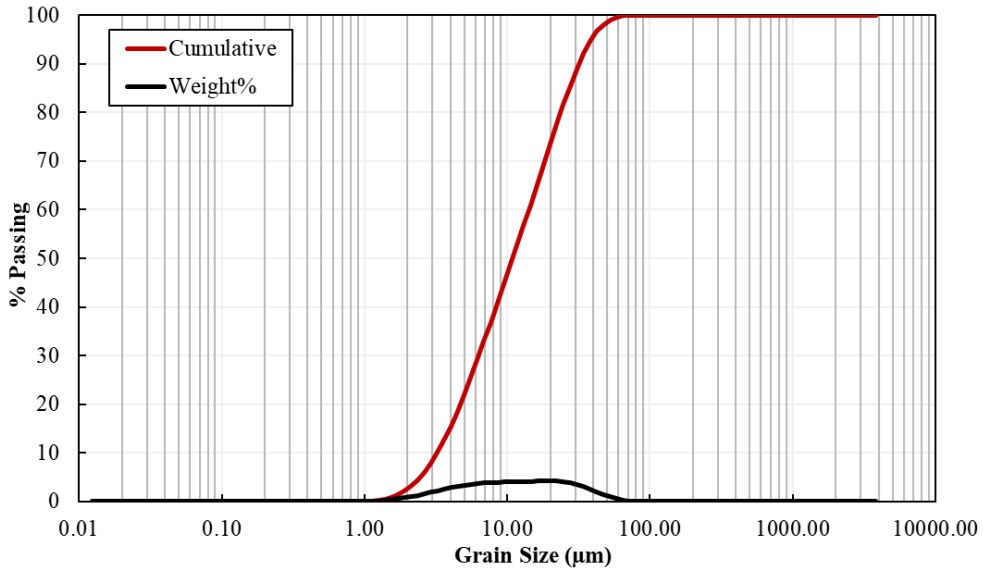
Supplementary Figure S12. Map of surface foam sample locations with placement locations and monitoring stations (Control North, Control South, and Olivine) given for reference.

Surface foam Sample 1 had a grain size distribution ranging between 1-58 µm with a D_{10} of 3 µm, D_{50} of 8 µm, and D_{90} of 25.3 µm (Supplementary Figure S13). The sample was 52.1 wt% talc, 21.6 wt% serpentine, 7.9 wt% forsteritic olivine, 7.1 wt% halite, 6.0 wt% mica, 4.0 wt% kaolinite and minor (< 1 wt%) contributions of chlorite and calcite. In sum, the sample was 84.3 wt% clays.



Supplementary Figure S13. Grain size distribution of surface foam Sample 1 collected during Placement 2.

Surface foam Sample 2 had a grain size distribution ranging between 1-72 µm with a D_{10} of 3.2 µm, D_{50} of 11 µm and D_{90} of 31.9 µm (Supplementary Figure S14). The sample was 41.8 wt% talc, 23.9 wt% forsteritic olivine, 20.9 wt% serpentine, 4.9 wt% mica, 3.9 wt% halite, 3.8 wt% kaolinite, and minor (< 1 wt%) contributions of chlorite and calcite. In sum, the sample was 71.8 wt% clays.



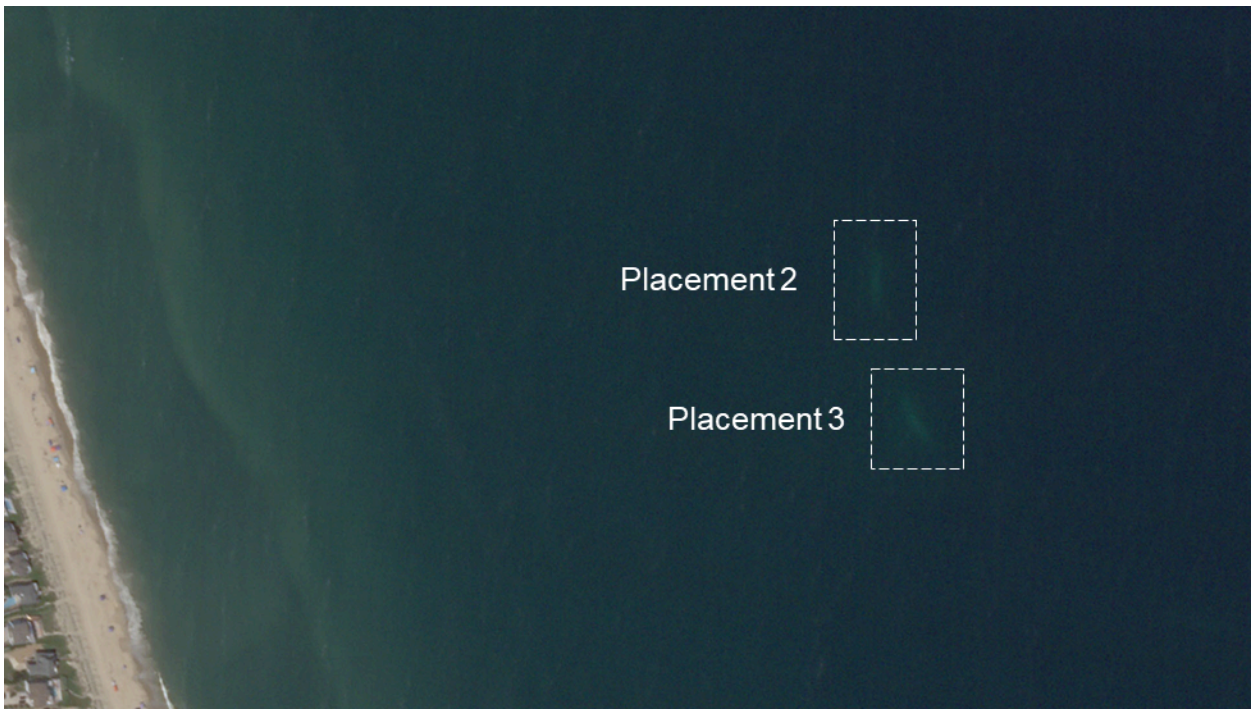
Supplementary Figure S14. Grain size distribution of surface foam Sample 2 collected during Placement 3.

1.6 Field Trial Monitoring

The monitoring program encompassed a suite of hydrodynamic geochemical, sedimentological, and ecological parameters observed pre- and post- deployment, and during each placement in both control and treatment areas.

Baseline data was collected prior to the deployment ("pre-deployment") from March to May 2024 to characterize ambient site conditions. Additional baseline data was collected in the hours before each placement ("pre-placement") and immediately after ("post-placement"). For Placement 1, pre- and post-placement monitoring occurred between 9:22-17:35 (release at 11:40), for Placement 2 between 8:00-20:00 (release at 10:35), and for Placement 3 between 9:35-19:20 (release at 13:20); the exact duration of data collection varied by sensor. Satellite imagery of the field site one day after the final feedstock placement, Placement 3, is provided in Supplementary Figure S15. Following deployment, monitoring continued ("post-deployment") on an approximately monthly cadence. The long-term monitoring program (pre/post deployment) featured three sampling stations (see below). The main manuscript reports data and results to April 2025, but the full monitoring program extends beyond this period.

The experimental design of the long-term monitoring featured three stations: Olivine (-75.747532, 36.193106; EPSG:4326 - WGS 84), Control North (-75.755012,36.208937; WGS 84), and Control South (-75.745677,36.188762; WGS 84). The Olivine station was located atop Placement 3, Control North was located 1.9 km north of the Olivine station, and Control South was located 500 m south of the Olivine station. This design was intended to isolate any impacts at the deployment site (Olivine station) from background spatial and temporal variability by comparison with control locations to the north and south of the site.



Supplementary Figure S15. Satellite imagery of the field site, taken 14 June 2024, one day after Placement 3, by Planet Labs PBC.

1.6.1 Mixed Layer Statistical Analysis

Water quality sonde measurements were taken throughout the water column. Due to the site being ~8 m deep and in an energetic coastal environment, it would be expected for the water column to remain well-mixed. To quantitatively determine if this was true, a mixed layer analysis was performed to determine if surface and bottom water could be considered as taken from the same water mass, and therefore if they could be combined for statistical analyses. Monterey & Levitus (1997) define a mixed layer as a consistent deviation in density or temperature between any given depths: density difference must be consistently greater than 0.000125 g cm^{-3} or temperature

difference must be consistently greater than 0.5 °C between depths. This site exhibited high variability in the water column over spatial and temporal timescales. Across the entire water column, a range in density was observed of up to 0.0035 g cm^{-3}, and a range in temperature up to 6 °C in the bottom water. Because these ranges, over the entire water column, are greater than the criteria above for consistent deviations, we conclude this site is well-mixed and all within the mixed layer, allowing for measurements and samples from all depths to be combined for statistical analyses.

1.6.2 Statistical Analysis of Pre- & Post-Deployment Monitoring Station Differentiation

The hypothesis that spatial variability in post-deployment water column measurements was influenced by proximity to the placement area (Olivine station) was evaluated. The study site is characterized by energetic hydrodynamic conditions which promote rapid water mass mixing and a lack of significant differences ($p > 0.05$) between olivine and control stations were reported for turbidity, pH, and oxygen percent saturation for all surveys (Supplementary Table S4). Similarly, there was no statistical difference ($p > 0.05$) in chlorophyll-a between stations for any survey except the 15 October 2024 survey. In this instance, differences between stations were reported, Control North had higher values than Olivine. This was most likely driven by a phytoplankton bloom that arrived from the neighbouring Chesapeake Bay, which is to the north of the project site. In the week prior to 15 October 2024 sampling, chlorophyll-a concentration was elevated (around 10 mg m^{-3}) at the southern mouth of the Chesapeake Bay (based on average current speeds over this period, water masses from the mouth of Chesapeake Bay need around one week to travel to the study site) (CoastWatch). Therefore the 15 October 2024 chlorophyll-a peak was most likely caused by the natural bloom event. Due to the lack of difference between water column measurements from stations, further analysis of pre- and post-deployment water column measurements treated data from the entire monitoring area together, as one site.

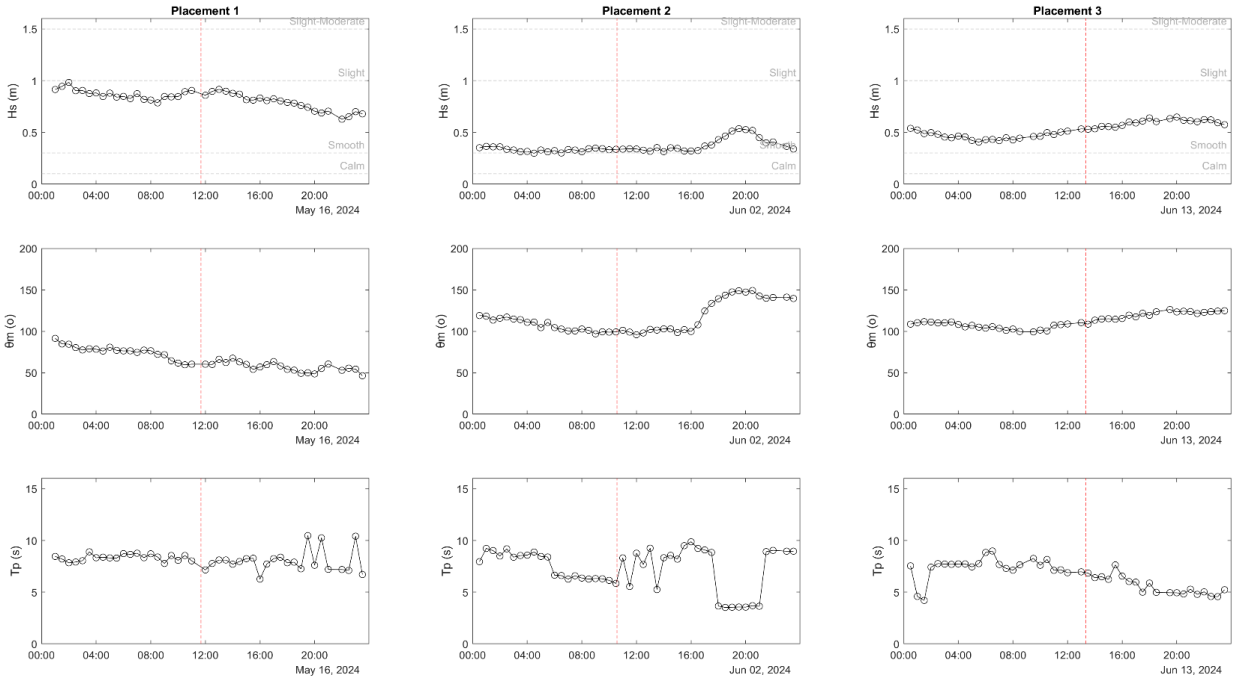
Supplementary Table S4. Results of the GLMM for sonde parameters tested among two stations and surveys. Pr values provided, with significant tests marked with bold font and asterisk * showing significance at p<0.05, ** significance at p<0.01, and *** significance at p<0.001 and the significance level conservatively reduced to $p < 0.001$ when the assumptions/diagnostics were not met (Anton et al. 2011, Cox et al 2020). Only significant results for pair-wise tests are provided.

Control North - Olivine												
	Chlorophyll-*a*; family = tweedie(link = "log")			**Oxygen % saturation;** normally distributed data			**pH;** normally distributed data			**Turbidity;** family = tweedie(link = "log")		
	df	Chisq	p	df	Chisq	p	df	Chisq	p	df	Chisq	p
Station	1	0.67	**0.414**	1	2.04	0.153	1	1.72	0.189	1	0.4822	0.4874
Time	5	254.7	**< 2.2e-16 *** **	5	11.96	**0.036 ***	4	10.93	**0.027***	5	49.4019	**1.837e-09 *** **
Station: Time	5	19.94	**0.002 ****	5	0.73	0.729	4	1.69	0.793	5	8.3099	0.14
Pair-wise			**15/10/24**									
Control South - Olivine												

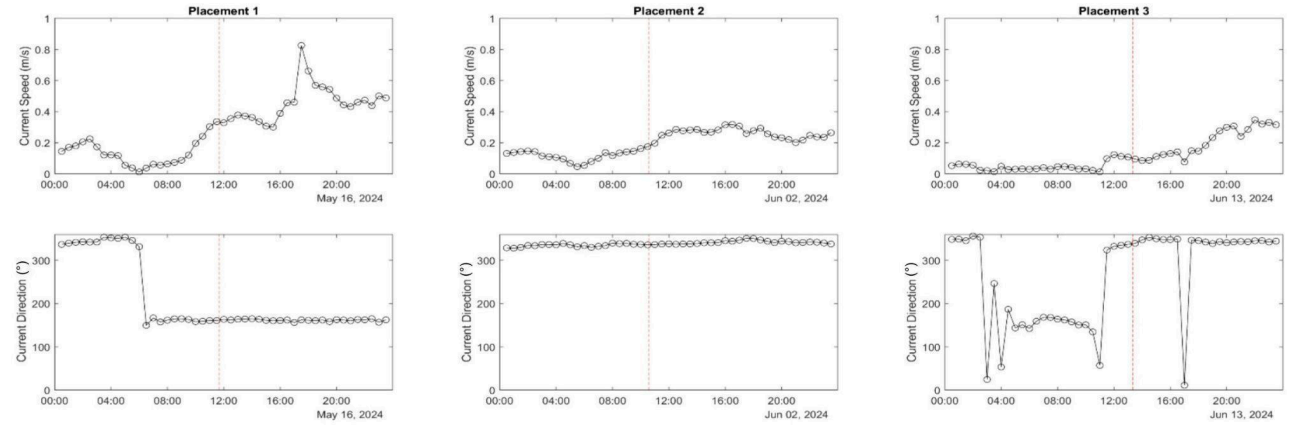
	Chlorophyll-*a*; family = tweedie(link = "log")			**Oxygen percent saturation;** family = tweedie(link = "log")			**pH;** normally distributed data			**Turbidity;** family = tweedie(link = "log")		
	df	Chisq	p	df	Chisq	p	df	Chisq	p	df	Chisq	p
Station	1	0	**0.996**	1	0.036	0.849	1	2.189	0.1390	1	0.1928	0.6606
Time	3	68.92	**7.256e-15 *****	2	1.244	0.537	5	14.03	**0.015***	3	19.418	**0.000224*****
Station: Time	3	2.28	0.515	2	0.543	0.762	5	14.05	0.0153	3	2.9369	0.4015

1.6.3 Oceanographic Conditions During Placements

Oceanographic conditions recorded during each placement are shown in Supplementary Figures S16 and S17, illustrating wave and current conditions, respectively. Measurements were sourced from U.S. Army Corps of Engineers (USACE) Field Research Facility (FRF) devices deployed off the Town of Duck. Near real-time wave conditions were recorded by a Waverider buoy located approximately 3.7 km offshore in -17.8 m of water (Station ID: 44056). Observations were recorded at 30 minute intervals. Depth-averaged current speeds and directions were derived from a bottom mounted Nortek Signature1000 Acoustic Doppler Current Profiler (ADCP) located approximately 600 m offshore at a nominal depth of -6.7 m.



Supplementary Figure S16. Wave conditions recorded during each placement, including significant wave height (Hs (m)), mean wave direction (θm (°)) and peak wave period (Tp (s)) (Station ID: 44056).



Supplementary Figure S17. Depth-averaged current conditions recorded during each placement, including current speed (m/s) and current direction (°).

1.6.4 Water Quality Monitoring

1.6.4.1 Fixed Aquatroll Array Depths

A vertical array of 3 YSI EXO2 Sondes ("fixed sonde array") was installed prior to the release of feedstock at the target coordinate, recovered for placement and re-installed on top of the placement after release. It was tethered to a floating buoy, recording data below the water surface, in the mid-water column and on the seafloor; the exact depths varied for each placement and were also influenced by the presence of the berms. The depths are shown in Supplementary Table S5.

Supplementary Table S5. Depth of the three YSI EXO2 Sondes (the 'sonde array') for each placement, pre- and post- feedstock release.

	Placement 1		**Placement 2**		**Placement 3**	
	Pre-	**Post-**	**Pre-**	**Post-**	**Pre-**	**Post-**
Surface	1.01 m	1.04 m	2.42 m	1.21 m	1.44 m	2.06 m
Middle	4.29 m	6.01 m	5.61 m	4.27 m	4.58 m	4.94 m
Bottom	6.81 m	8.27 m	6.44 m	6.55 m	-	7.29 m

1.6.4.2 AquaTROLL 500 Sonde and YSI EXO2 Sonde Parameters

Water quality parameters were measured with an AquaTROLL 500 sonde and YSI EXO2 sonde. The AquaTROLL was used through 2024 for both short- and long-term monitoring and the EXO2 through 2025 for long-term monitoring. The specifications for each parameter is given in Supplementary Table S6.

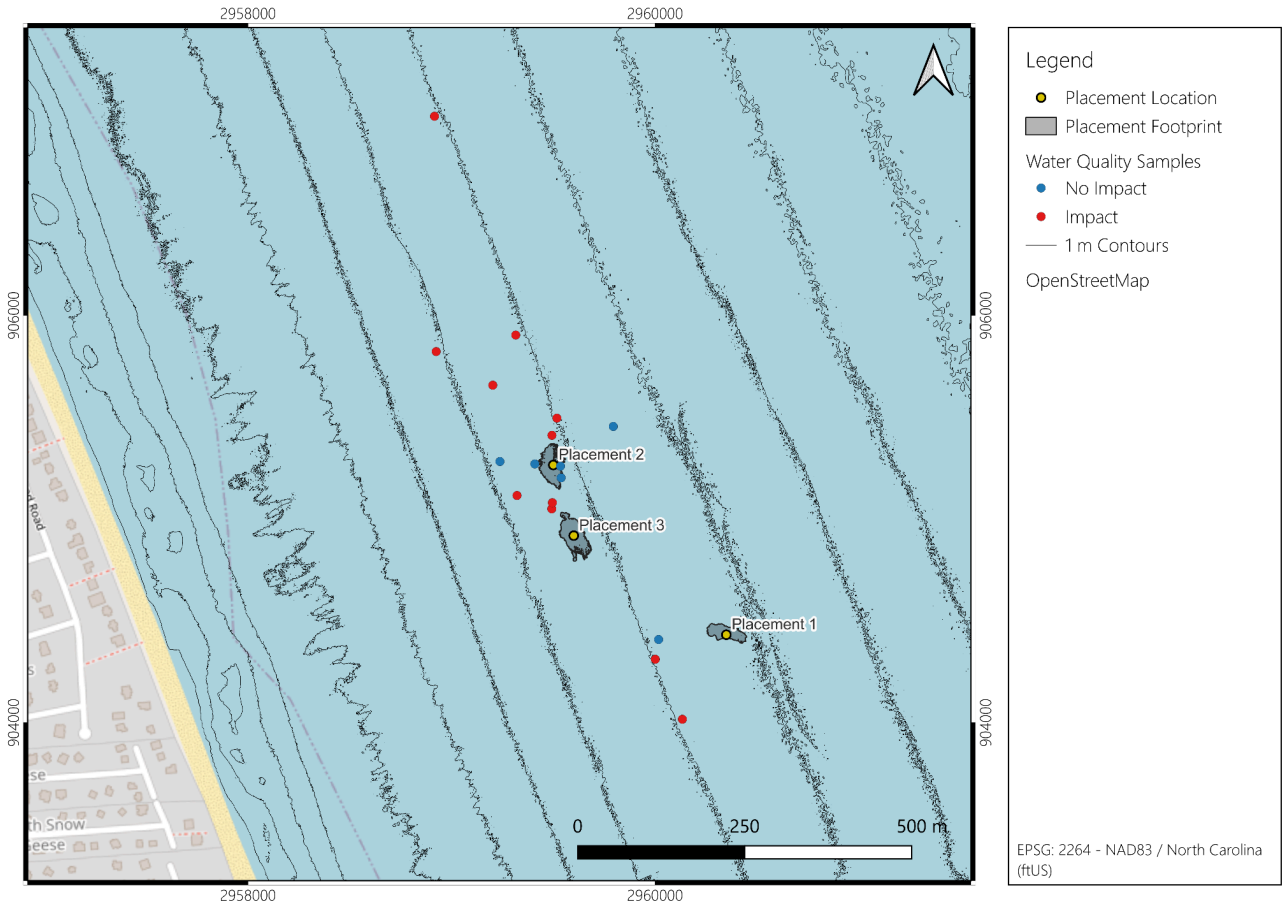
Supplementary Table S6. AquaTROLL 500 sonde and YSI EXO2 sonde specification for select parameters

Parameter	**Instrument**	**Unit**	**Accuracy**	**Precision**
Depth	AquaTROLL	m	± 0.1% full scale (FS)	0.01% FS

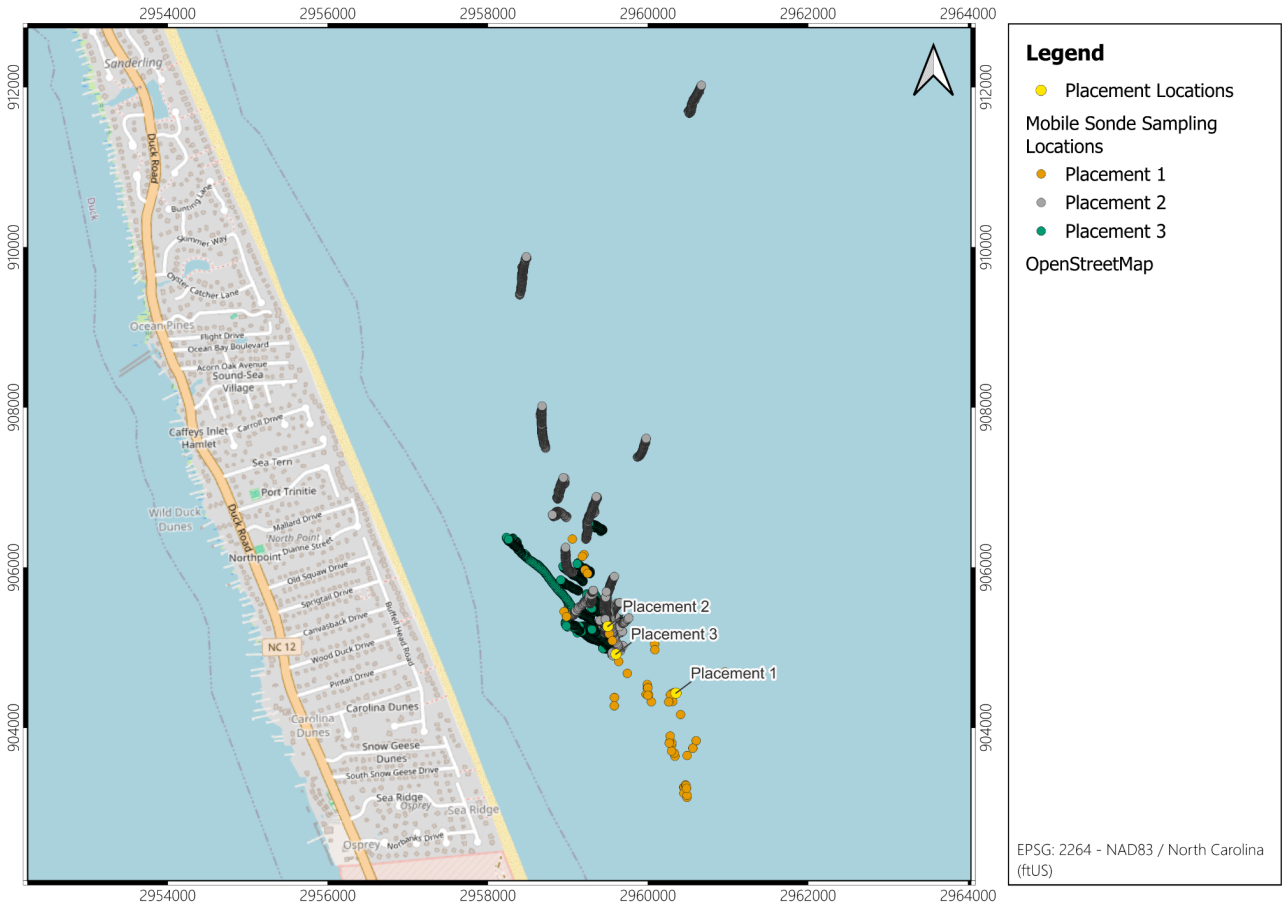
	EXO2	m	± 0.004 m	0.001
Pressure	AquaTROLL	psi	± 0.1% FS	± 0.01% FS
Turbidity	AquaTROLL	NTU	± 0.05 NTU or ± 2% of reading, whichever is greater (w.i.g.)	0.01
	EXO2	FNU	± 0.3 FNU or ±2% of reading, w.i.g.	0.01
pH	AquaTROLL	-	± 0.1 units	0.01 units
	EXO2	-	± 0.1 units	0.01 units
Dissolved oxygen	AquaTROLL	mg L^{-1}	± 0.1	0.01
	EXO2	mg L-1	± 0.1 or 1% of reading, w.i.g.	0.01
Chlorophyll-*a* fluorescence	AquaTROLL	RFU	-	0.001
	EXO2	RFU	-	0.01
Salinity	AquaTROLL	PSU	-	0.1
	EXO2	PPT	± 0.1 ppt or ± 1.0% of reading, w.i.g.	0.01
Temperature	AquaTROLL	°C	± 0.1	0.01
	EXO2	°C	± 0.2	0.001

1.6.4.3 Water Quality Sampling Locations: Placements

Discrete water column samples were collected with Niskin bottles from the water column during each placement (Supplementary Figure S18) for water quality monitoring. Four samples (1 pre-placement, 3 post-placement) were collected during Placement 1, six samples (2 pre-placement, 4 post-placement) were collected during Placement 2, and seven samples (2 pre-placement, 5 post-placement) were collected during Placement 3. The samples were later assigned to either Impact or No Impact clusters (see main text). Each placement had 2 No Impact samples, with the remainder as Impact samples. Mobile sonde casts were completed during each placement, with locations mapped in Supplementary Figure S19.



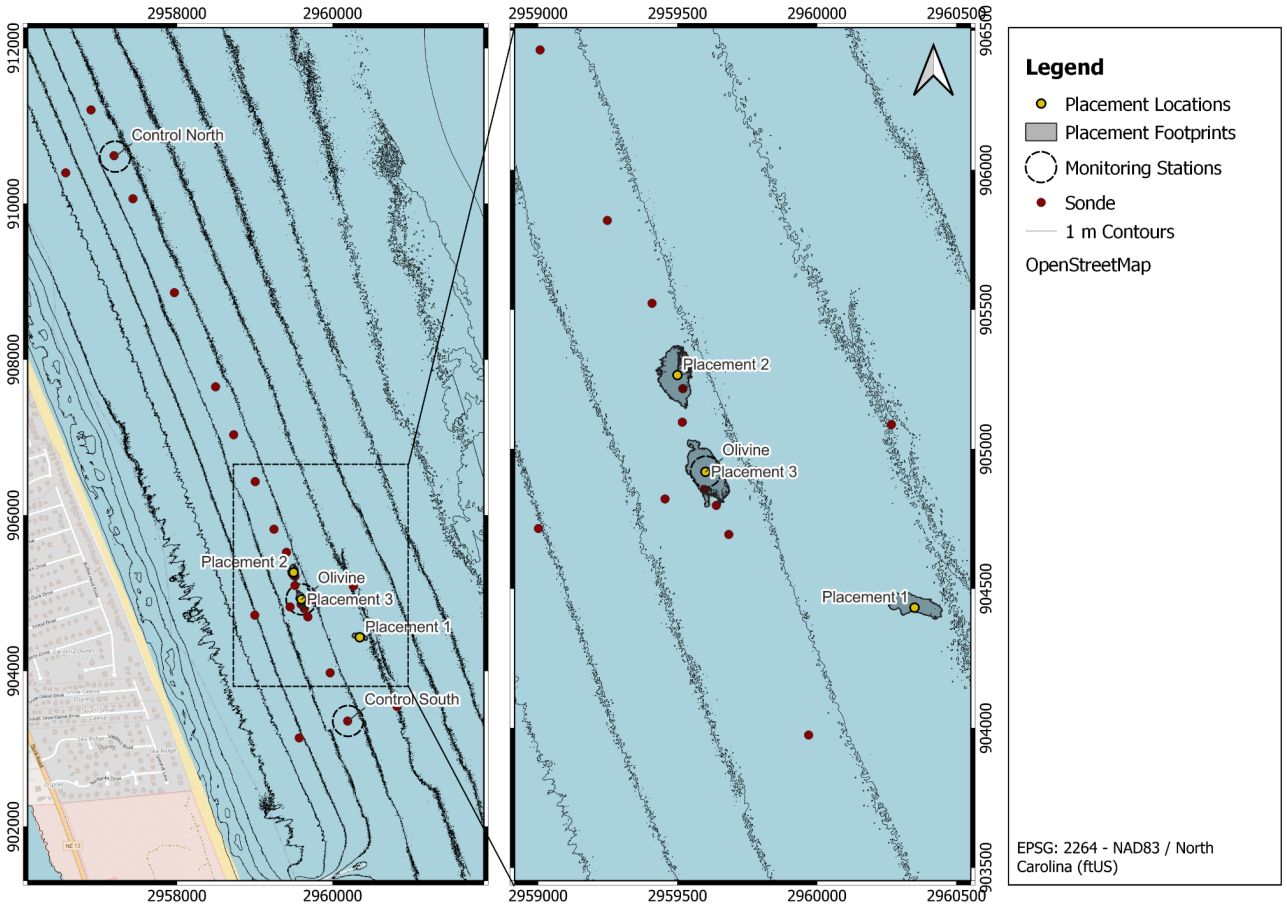
Supplementary Figure S18. Location of discrete water quality samples during placement monitoring. The samples are colored based on impact or no impact.



Supplementary Figure S19. Location of mobile sonde sampling locations during placement monitoring. The samples are colored based on the placement.

1.6.4.4 Water Quality Sampling Locations: Pre- and Post-Deployment

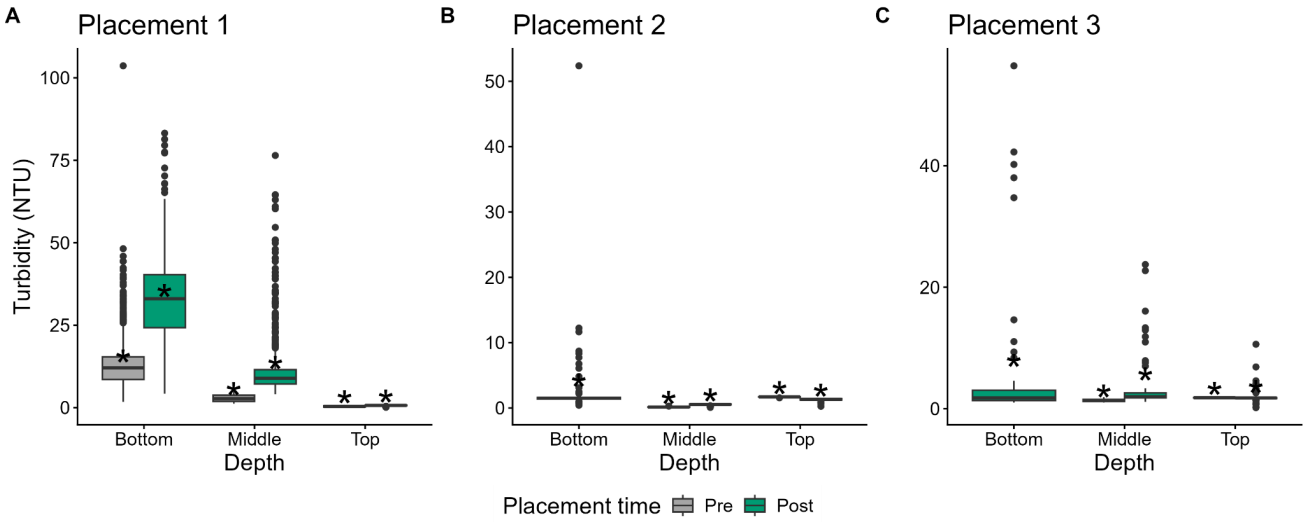
Mobile sonde surveys were conducted at and between the Olivine and Control Stations, 1-3 times monthly, capturing 3-26 water quality snapshots primarily from bottom water (~1 m above seafloor) (main text, Figure 2, 'Sonde') (Supplementary Figure S20). In addition, discrete bottom water samples were collected with 5 L Niskin bottles at the Olivine and Control Stations at an approximately monthly cadence.



Supplementary Figure S20. Location of water quality samples during pre- and post-deployment monitoring.

1.6.4.5 Detailed Turbidity Data (Fixed Sonde Array) During Placements

Supplementary Figure S21 and Supplementary Table S7 provide summaries of the turbidity (NTU) data derived from the fixed sonde array during placements.



Supplementary Figure S21. Turbidity (NTU) recorded with the fixed sonde array over each placement site at the top, middle and bottom of the water column. Mean (asterisks), median (horizontal line), 25th and 75th percentile (box), minimum and maximum value (vertical line), and outliers (dots) are presented. Note the differing y-axis scales.

Supplementary Table S7. Turbidity values pre- and post-placement, discretized by depth. Data recorded by the fixed sonde array.

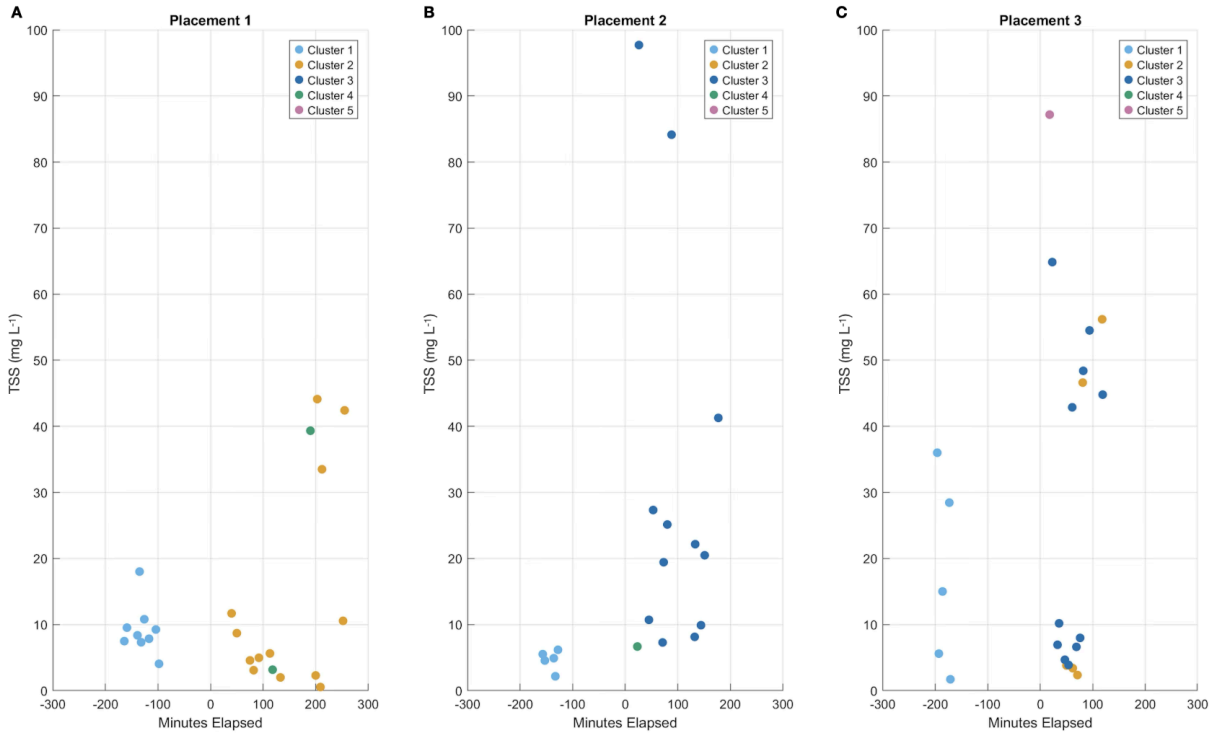
Placement	Relative Depth	Pre-Placement Turbidity (NTU) (mean ± SE)	n	Post-Placement Turbidity (NTU) (mean ± SE)	n	ART Pre-Post pair-wise p value
1	**Top**	0.38 ± 0.01	987	0.68 ± 0.00	1077	<0.0001
	Middle	2.88 ± 0.03	1136	10.80 ± 0.23	1077	<0.0001
	Bottom	12.80 ± 0.21	1136	32.70 ± 0.35	1077	<0.0001
2	**Top**	1.69 ± 0.01	43	1.28 ± 0.02	80	<0.0001
	Middle	0.14 ± 0.01	43	0.53 ± 0.01	78	<0.0001
	Bottom	-	0	2.77 ± 0.68	80	-
3	**Top**	1.80 ± 0.00	41	2.10 ± 0.22	52	<0.0001
	Middle	1.38 ± 0.03	41	4.16 ± 0.72	52	<0.0001
	Bottom	-	0	6.41 ± 1.71	52	-

1.6.4.6 Detailed Turbidity (Mobile Sonde) and TSS Data Summary During Placements

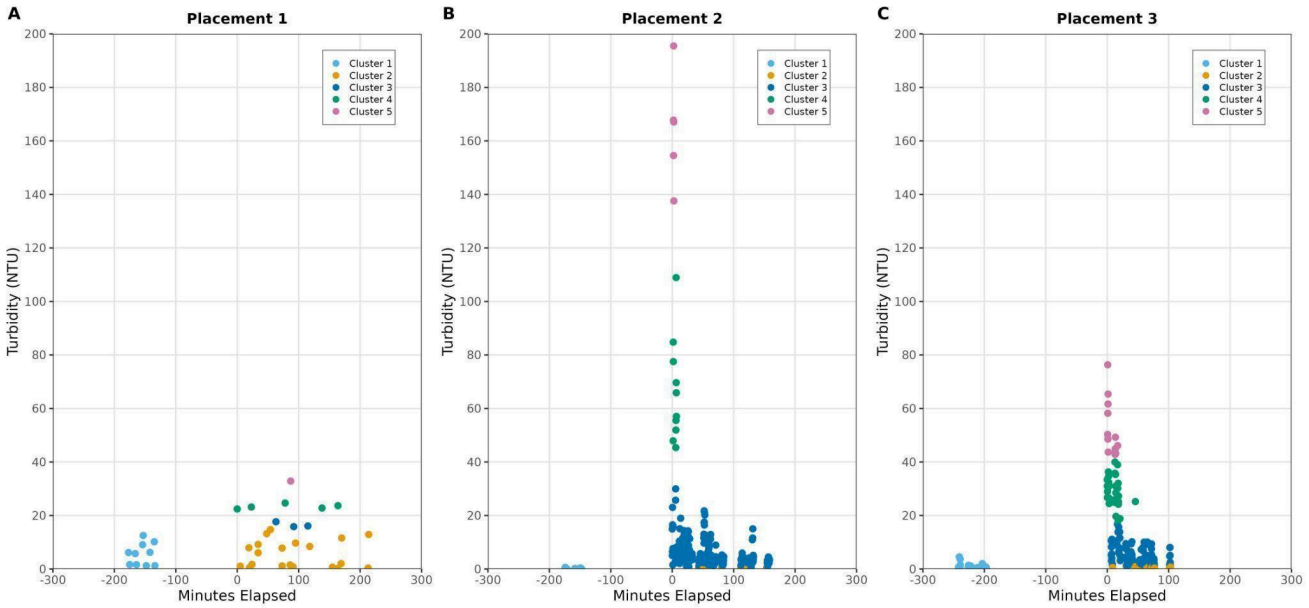
Supplementary Table S8 provides a summary of the turbidity (NTU) data derived from the mobile sonde array, and TSS (mg L^{-1}) data collected during each placement. The data is discretized by cluster. Supplementary Figure S22 provides the TSS data for each placement, grouped by cluster. Supplementary Figures S23, S24, and S25 provide the sonde turbidity, Chlorophyll-a, and oxygen saturation data, respectively, for each placement, grouped by cluster.

Supplementary Table S8. Turbidity (NTU) and TSS (mg L^{-1}) data for each placement, grouped by Cluster. Mean ± standard error (SE), number of samples (N) and results of Silhouette Scores (S) are presented.

			Cluster				
			1	**2**	**3**	**4**	**5**
Placement 1	**Turbidity (NTU)**	**mean ± SE**	5.56 ± 1.30	5.58 ± 1.61	16.53 ± 0.31	23.34 ± 0.27	32.85
		n	10	20	3	5	1
		S	-	-	0.95	0.97	1
	TSS (mg L^{-1})	**mean ± SE**	9.2 ± 1.3	13.4 ± 4.4	-	21.3 ± 18.1	-
		n	9	13	0	2	0
Placement 2	**Turbidity (NTU)**	**mean ± SE**	0.09 ± 0.02	0.09 ± 0.01	11.92 ± 2.32	70.07 ± 11.25	164.48 ± 9.49
		n	50	18	9	3	5
		S	-	-	0.99	0.73	0.9
	TSS (mg L^{-1})	**mean ± SE**	4.7 ± 0.7	-	31.1 ± 8.6	6.7	-
		n	5	0	12	1	0
Placement 3	**Turbidity (NTU)**	**mean ± SE**	0.51 ± 0.08	0.52 ± 0.03	4.70 ± 0.36	30.27 ± 0.97	57.73 ± 4.24
		n	74	35	85	13	7
		S	-	-	0.94	0.82	0.55
	TSS (mg L^{-1})	**mean ± SE**	17.4 ± 6.6	22.5 ± 11.9	26.9 ± 7.2	-	87.2
		n	5	5	11	0	1



Supplementary Figure S22. Total Suspended Sediment (TSS) for each placement, grouped by cluster.



Supplementary Figure S23. Turbidity (NTU) for each placement, grouped by cluster.

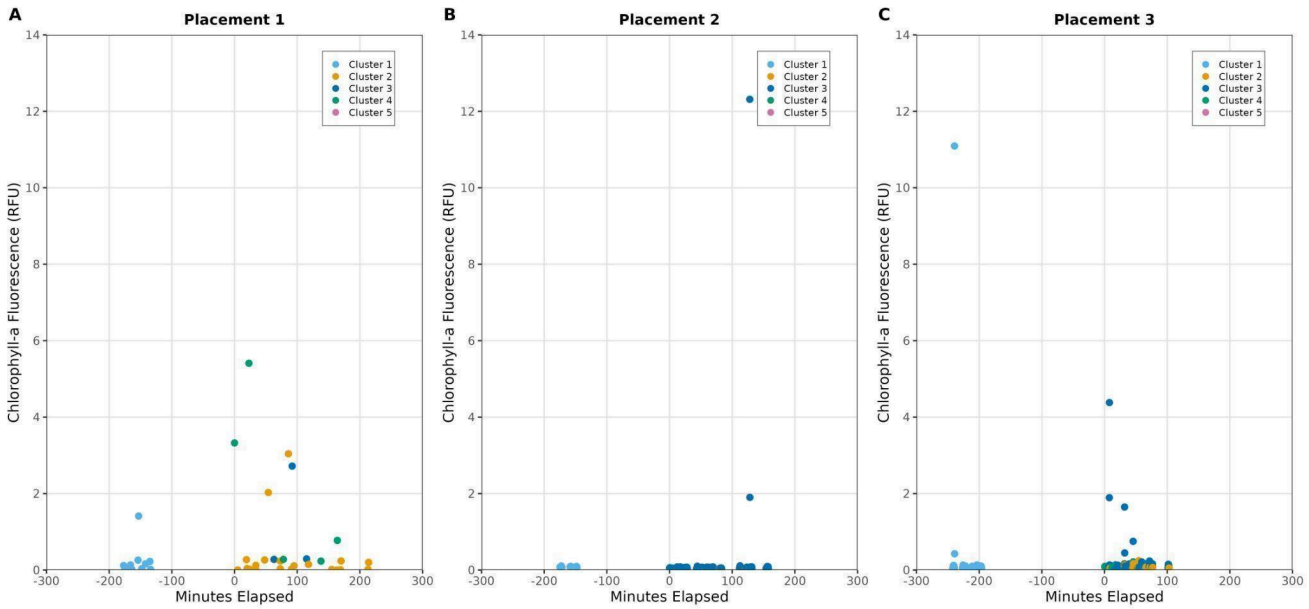
1.6.4.7 Detailed Mobile Sonde Water Quality Parameters During Placements

Statistical tests were performed to assess the significance of Chlorophyll-a and oxygen (Supplementary Table S9).

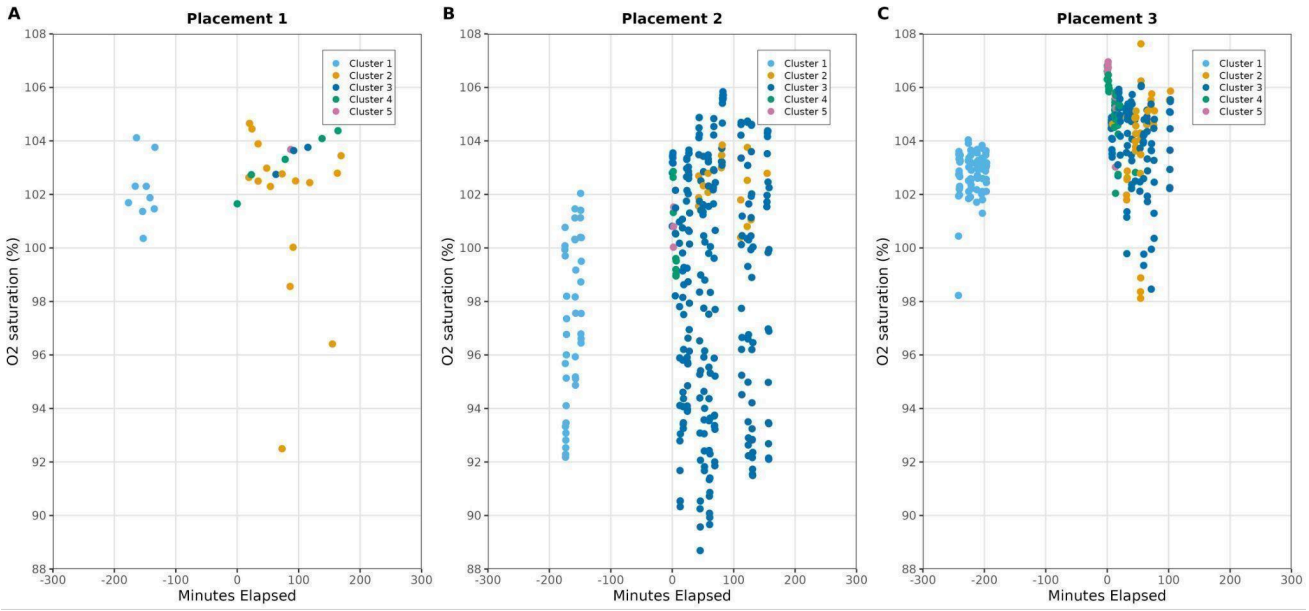
Supplementary Table S9. Results of statistical tests performed for water quality parameters run to detect short-term responses to olivine placements.

	Chlorophyll-*a*	**Oxygen**
Placement 1		

df	3	3
Chi-squared	16.701	F value - 6.443
p value	0.0008 ***	0.0025**
pair-wise	Cluster 1 ,2 ≠ Cluster 3,4	Cluster 1 ≠ Cluster 2,3,4
Placement 2		
df	4	4
Chi-squared	F value - 34.64	19.881
p value	< 2.2e-16 ***	0.0005 ***
pair-wise	Cluster 1 ≠ Cluster 2,3; Cluster 2 ≠ Cluster 3	Cluster 1 ≠ Cluster 2; Cluster 2 ≠ Cluster 3
Placement 3		
df	4	4
Chi-squared	11.806	122.26
p value	0.050 - marginally significant	< 2.22e-16 ***
pair-wise	-	Cluster 1 ≠ Cluster 2,3,4,5; Cluster 2, 3 ≠ Cluster 4,5



Supplementary Figure S24. Chlorophyll-*a* fluorescence (RFU) for each placement, grouped by cluster.



Supplementary Figure S25. Oxygen saturation (%) for each placement, grouped by cluster.

1.6.4.8 Detailed Discrete Water Chemistry During Placements

Mean values for discrete water chemistry samples to compare Baseline vs Impact clusters on placement days (Supplementary Table S10).

Supplementary Table S10. Mean ± standard error for discrete water chemistry samples for Baseline (Cluster 1) and Impact (Clusters 3-5) samples merged for all three Placements together. All parameters were measured on 5 Baseline samples and 10-11 Impact samples.

Parameter	Baseline	Impact
Sonde pH	8.01 ± 0.01	8.03 ± 0.01
DIC (µmol kg^{-1})	1935.5 ± 37.5	1963.3 ± 16.1
TA (µmol kg^{-1})	2042.75 ± 19.65	2059.46 ± 9.97
$\Omega_{aragonite}$	2.33 ± 0.10	2.50 ± 0.07
pCO_2 (µatm)	452.57 ± 13.27	436.59 ± 11.02
Cd (µmol kg^{-1})	0.0004 ± 0.0000	0.0004 ± 0.0000
Si (µmol kg^{-1})	11.8429 ± 1.0014	11.6597 ± 0.6018
Cr (µmol kg^{-1})	0.0024 ± 0.0004	0.0026 ± 0.0003
Mn (µmol kg^{-1})	0.0292 ± 0.0061	0.0458 ± 0.0076

Fe (µmol kg^{-1})	0.0361 ± 0.0133	0.0415 ± 0.0073
Co (µmol kg^{-1})	0.0005 ± 0.0000	0.0010 ± 0.0002
Ni (µmol kg^{-1})	0.0072 ± 0.0003	0.0159 ± 0.0029
Cu (µmol kg^{-1})	0.0085 ± 0.0006	0.0085 ± 0.0003
Zn (µmol kg^{-1})	0.4742 ± 0.0564	0.4298 ± 0.0524
NO_2^- (mg L^{-1})	0.0009 ± 0.0002	0.0005 ± 0.0001
NO3+NO2 (mg L^{-1})	0.0018 ± 0.0005	0.0030 ± 0.0007
NH4 (µmol kg^{-1})	1.8684 ± 0.6464	1.4140 ± 0.2836
SiO_2^- (µmol kg^{-1})	4.0758 ± 0.6837	4.5980 ± 0.4827
Mg (mmol kg^{-1})	43.8536 ± 0.7732	43.5326 ± 0.3495
Ca (mmol kg^{-1})	8.7214 ± 0.1802	8.7314 ± 0.0914

1.6.4.9 Detailed Sonde and Discrete Water Chemistry Data Pre- & Post-Deployment

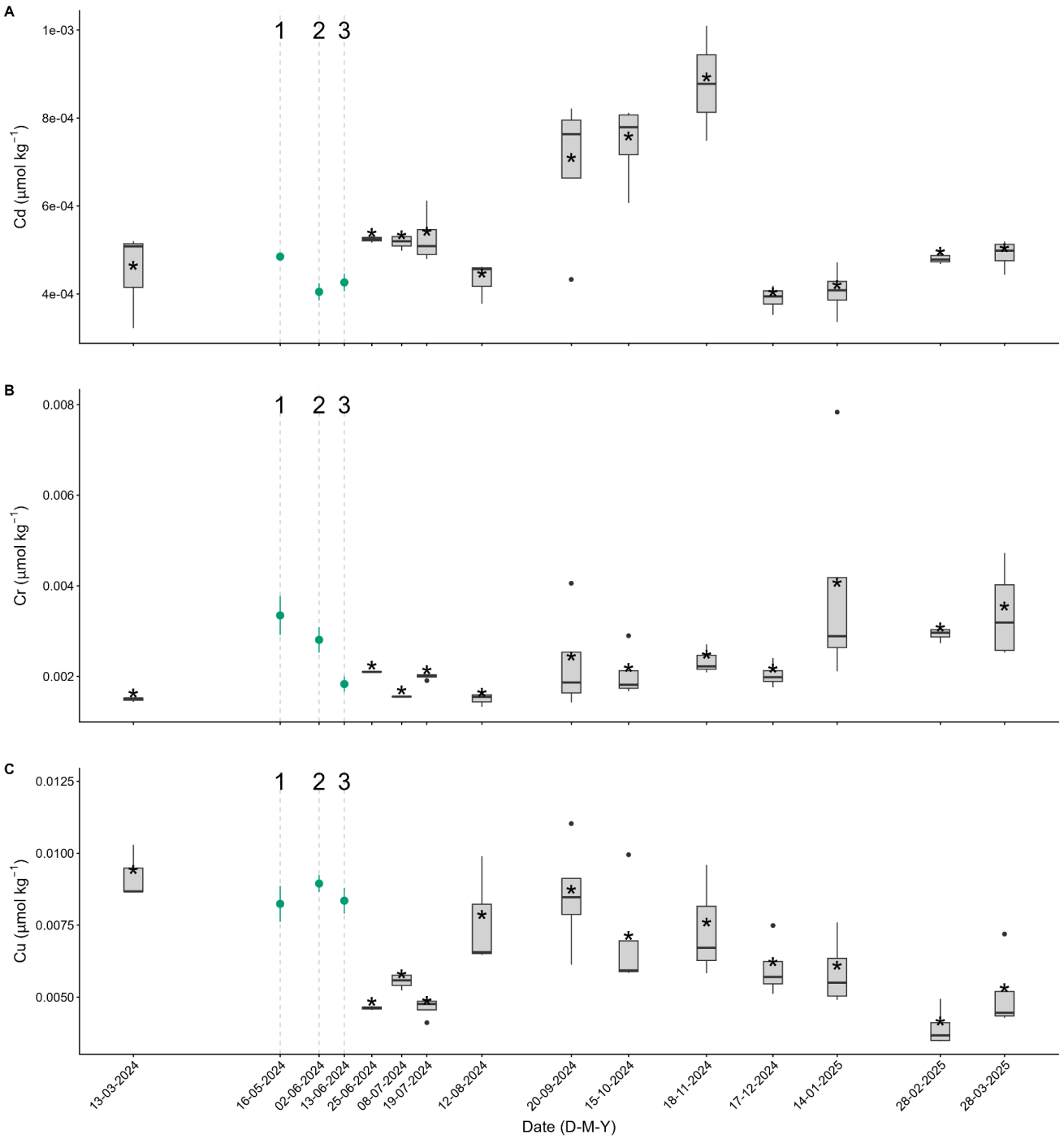
Supplementary Table S11 presents month-to-month pairs of sonde and discrete water chemistry that were significantly different from each other. Supplementary Figures S26, S27, S28, S29, and S30 present discrete parameters over the annual dataset of trace metals, major cations, carbonate chemistry, nutrients, and salinity, respectively.

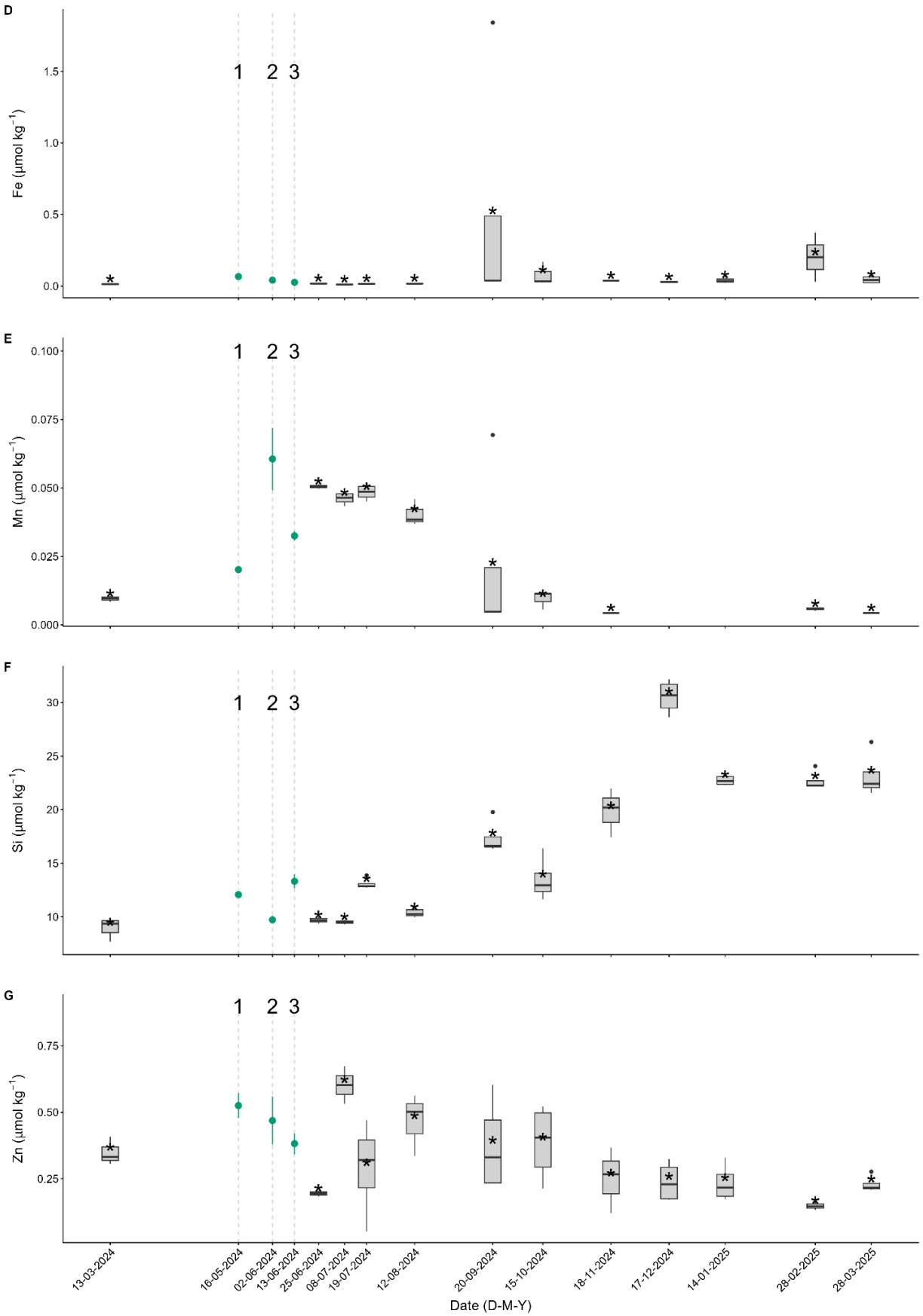
Supplementary Table S11. Statistical results of pairwise comparisons for parameters with significant differences from month-to-month for sonde and discrete samples.

	Significant difference in pairwise comparison (d/m/y)	**p value**
Sonde parameters		
Turbidity	22/08/24 - 20/09/24	0.000
	18/11/24 - 26/11/24	0.004
	14/01/25 - 27/01/25	0.000
	28/03/25 - 04/04/25	0.011
Chlorophyll-*a*	20/09/24 - 30/09/24	0.002

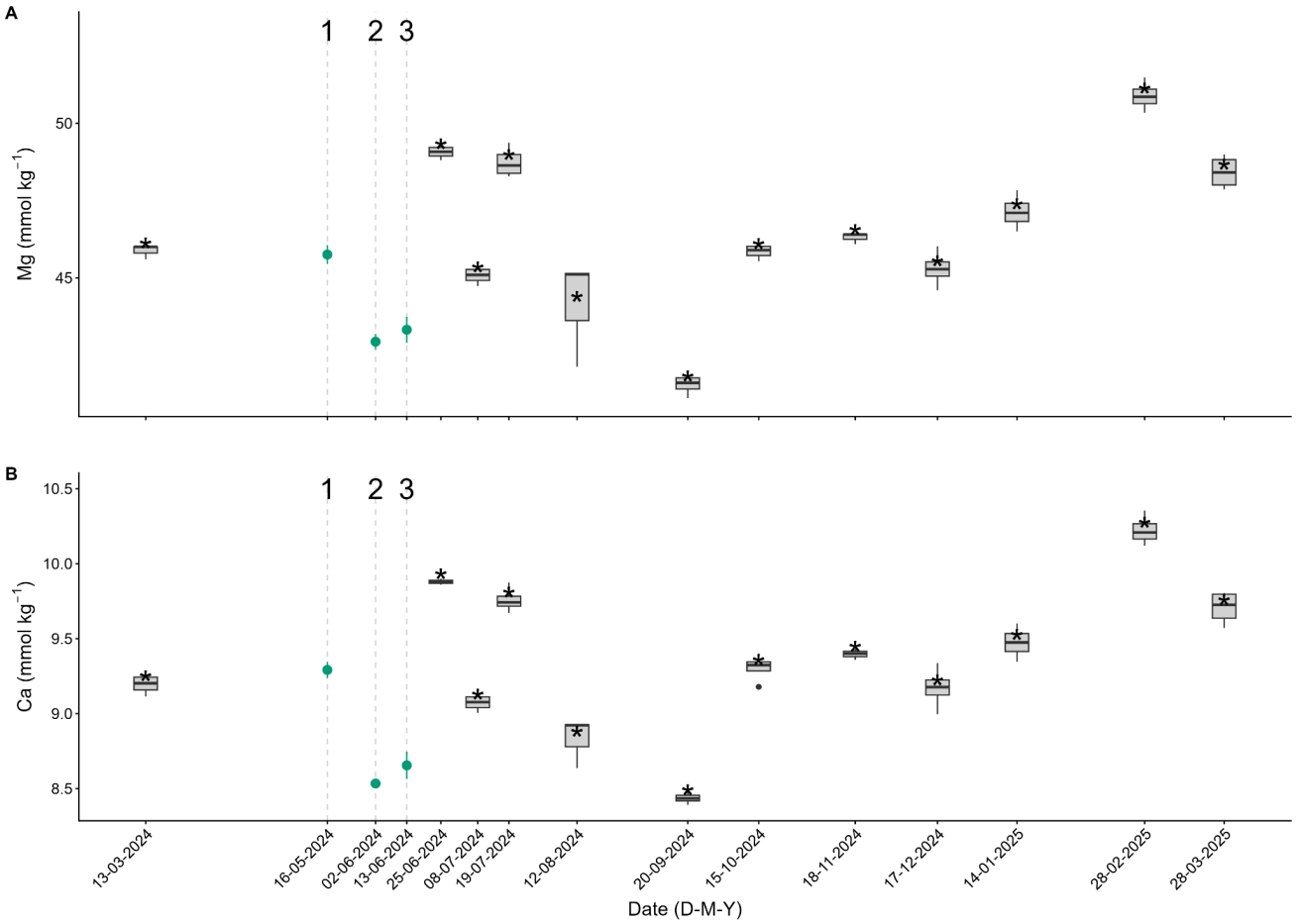
	15/10/24 - 22/10/24	0.000
	26/11/24 - 14/01/25	0.000
	14/01/25 - 27/01/25	0.000
	27/01/25 - 28/02/25	0.000
	28/03/25 - 04/04/25	0.000
Oxygen percent saturation	22/08/24 - 20/09/24	0.000
	14/01/25 - 27/01/25	0.000
	28/02/25 - 28/03/25	0.000
	28/03/25 - 04/04/25	0.000
	28/03/25 - 04/04/25	0.000
Discrete parameters		
Cd	12/08/24 - 20/09/24	0.012
	18/11/24 - 17/12/24	0.000
Mn	13/03/24 - 25/06/24	0.050
Co	19/07/24 - 12/08/24	0.020
	20/09/24 - 15/10/24	0.044
Cu	13/03/24 - 25/06/24	0.009
Si	12/08/24 - 20/09/24	0.000
	20/09/24 - 15/10/24	0.029
	15/10/24 - 18/11/24	0.000
	18/11/24 - 17/12/24	0.000
	17/12/24 - 14/01/24	0.000
Mg	13/03/24 - 25/06/24	0.000
	25/06/24 - 08/07/24	0.000
	08/07/24 - 19/07/24	0.000
	19/07/24 - 12/08/24	0.000
	12/08/24 - 20/09/24	0.000
	20/09/24 - 15/10/24	0.000
	17/12/24 - 14/01/25	0.007
	14/02/25 - 28/02/25	0.000

	28/02/25 - 28/03/25	0.000
Ca	13/03/24 - 25/06/24	0.000
	25/06/24 - 08/07/24	0.000
	07/08/24 - 19/07/24	0.000
	19/07/24 - 12/08/24	0.000
	12/08/24 - 20/09/24	0.000
	20/09/24 - 15/10/24	0.000
	17/12/24 - 14/01/25	0.005
	14/02/25 - 28/02/25	0.000
	28/02/25 - 28/03/25	0.000
NO2	17/12/24 - 14/01/25	0.001
NH4	20/09/24 - 18/11/24	0.001
SiO_2	18/11/24 - 17/12/24	0.000
	17/12/24 - 14/01/25	0.000
Alkalinity	13/03/24 - 25/06/24	0.015
	25/06/24 - 08/07/24	0.016
DIC	13/03/24 - 25/06/24	0.018
	25/06/24 - 08/07/24	0.006
Discrete pH	18/11/24 - 17/12/24	0.038
	17/12/24 - 14/01/25	0.000
Omega_arag	12/08/24 - 20/09/24	0.038
	28/02/25 - 28/03/25	0.024
pCO_2	18/11/24 - 14/01/25	0.045

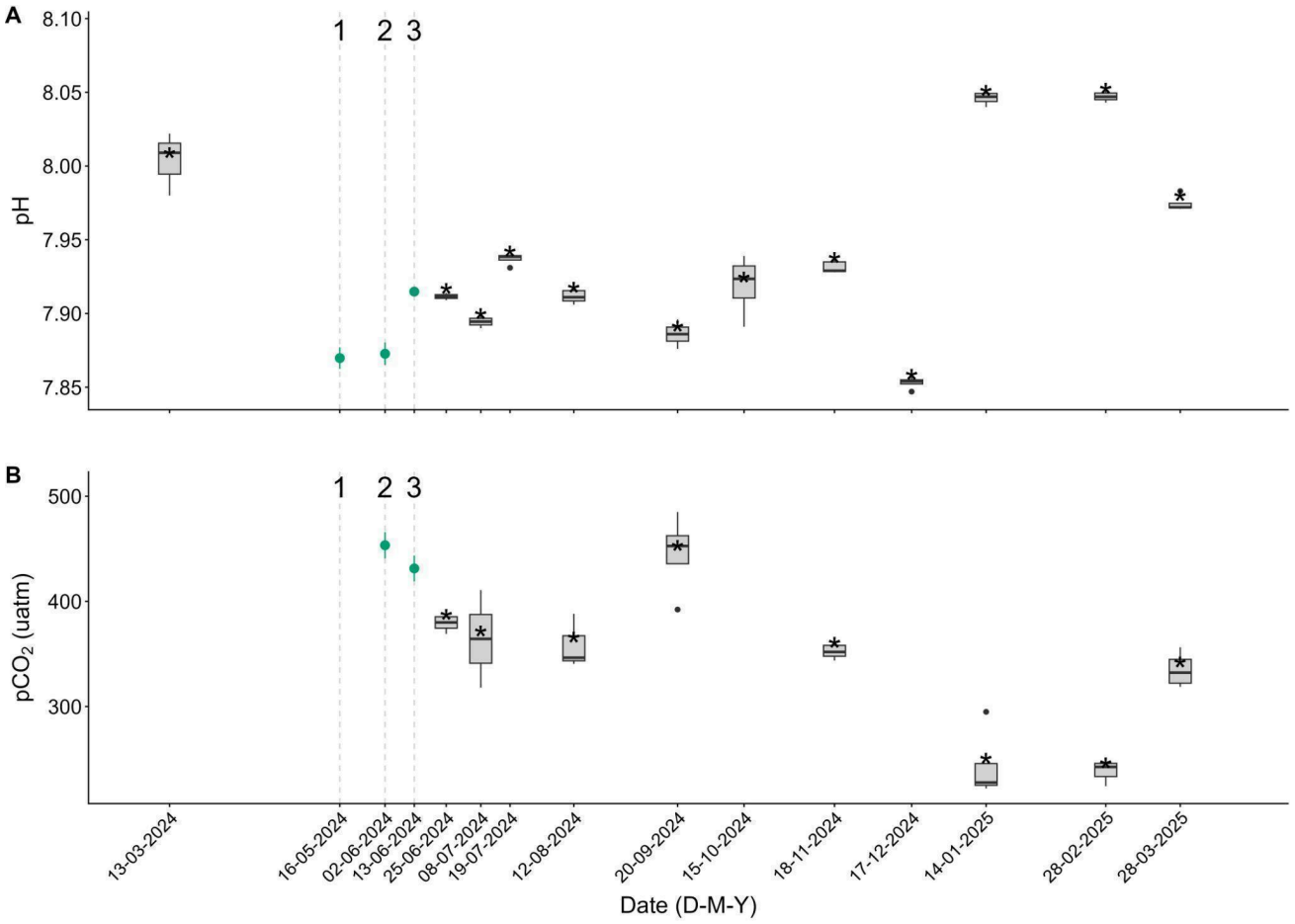

A
B
C
1
2
3
Cd (µmol kg^{-1})
Cr (µmol kg^{-1})
Cu (µmol kg^{-1})
1e-03
8e-04
6e-04
4e-04
0.008
0.006
0.004
0.002
0.0125
0.0100
0.0075
0.0050
13-03-2024
16-05-2024
02-06-2024
13-06-2024
25-06-2024
08-07-2024
19-07-2024
12-08-2024
20-09-2024
15-10-2024
18-11-2024
17-12-2024
14-01-2025
28-02-2025
28-03-2025
Date (D-M-Y)



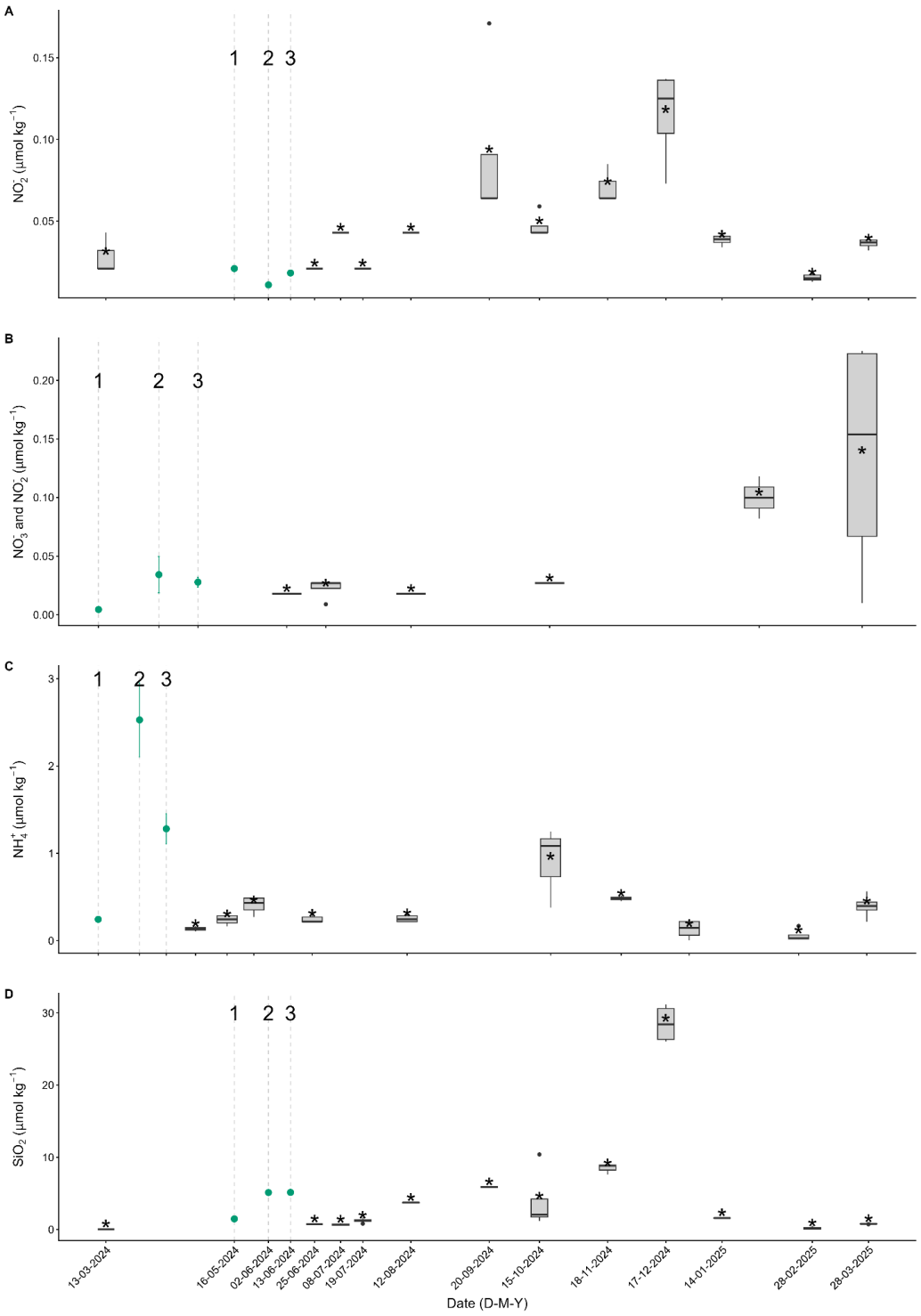
Supplementary Figure S26. Trace metals (A) Cd, (B) Cr, (C) Cu, (D) Fe, (E) Mn, (F) Si, (G) Zn measured in discrete seawater samples. Mean (asterisk), median (horizontal line), 25th and 75th percentile (box), minimum and maximum value (vertical line), and outliers (dots) are presented. The mean (green dot) derived from impact clusters for each placement day has been plotted for reference.



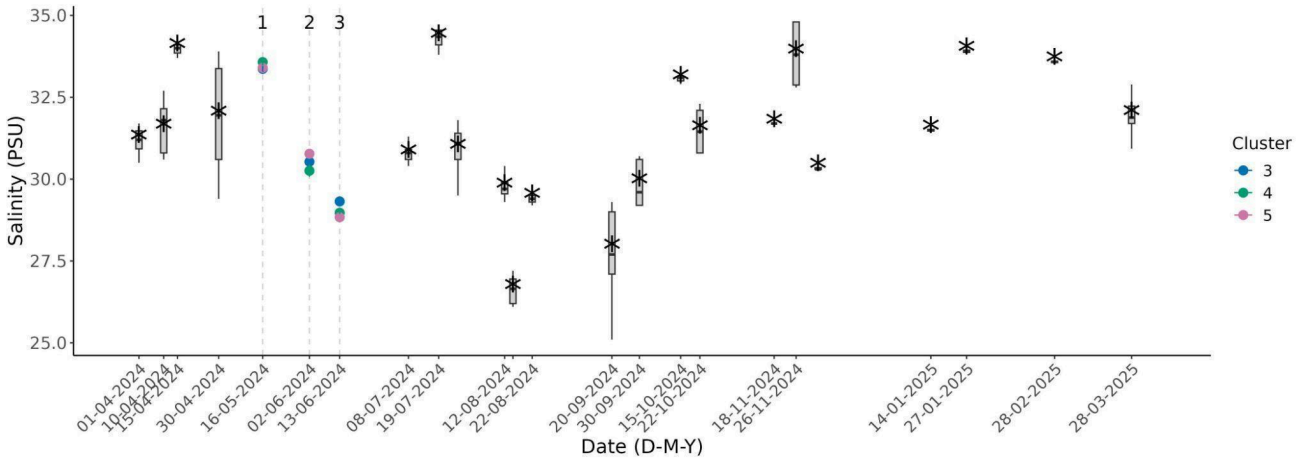
Supplementary Figure S27. Major cations (A) Mg and (B) Ca measured in discrete seawater samples. Mean (asterisk), median (horizontal line), 25th and 75th percentile (box), minimum and maximum value (vertical line), and outliers (dots) are presented. The mean (green dot) derived from impact clusters for each placement day has been plotted for reference.



Supplementary Figure S28. A) Discrete pH measured via spectrophotometer and B) calculated pCO_2 (calculated with CO2SYS using DIC and pH). Mean (asterisk), median (horizontal line), 25th and 75th percentile (box), minimum and maximum value (vertical line), and outliers (dots) are presented. The mean (green dot) derived from impact clusters for each placement day has been plotted for reference.

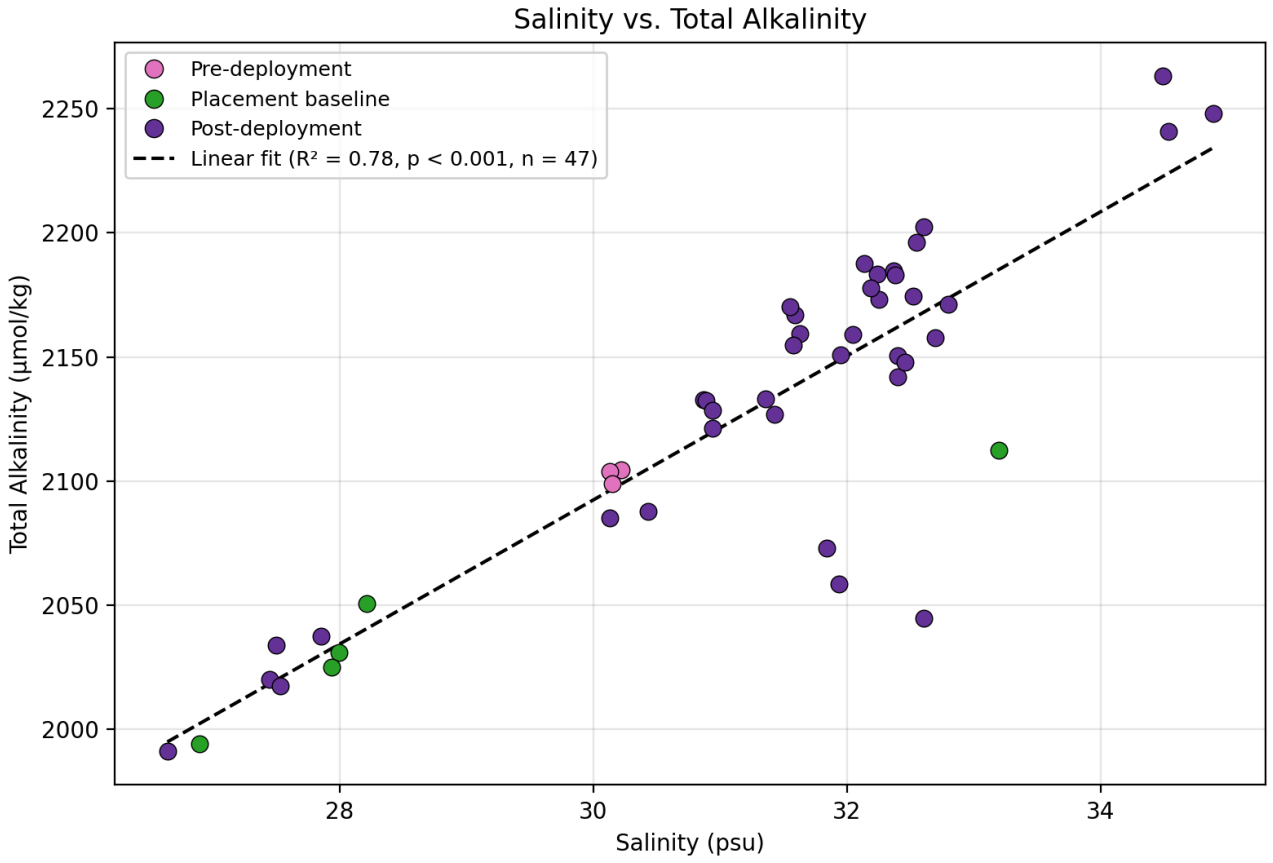


Supplementary Figure S29. Nutrients (A) NO_2^-, (B) NO_2^-+NO_3^-, (C) NH_4^+, (D) SiO_2 measured in discrete seawater samples. Mean (asterisk), median (horizontal line), 25th and 75th percentile (box), minimum and maximum value (vertical line), and outliers (dots) are presented. The mean (green dot) derived from impact clusters for each placement day has been plotted for reference.



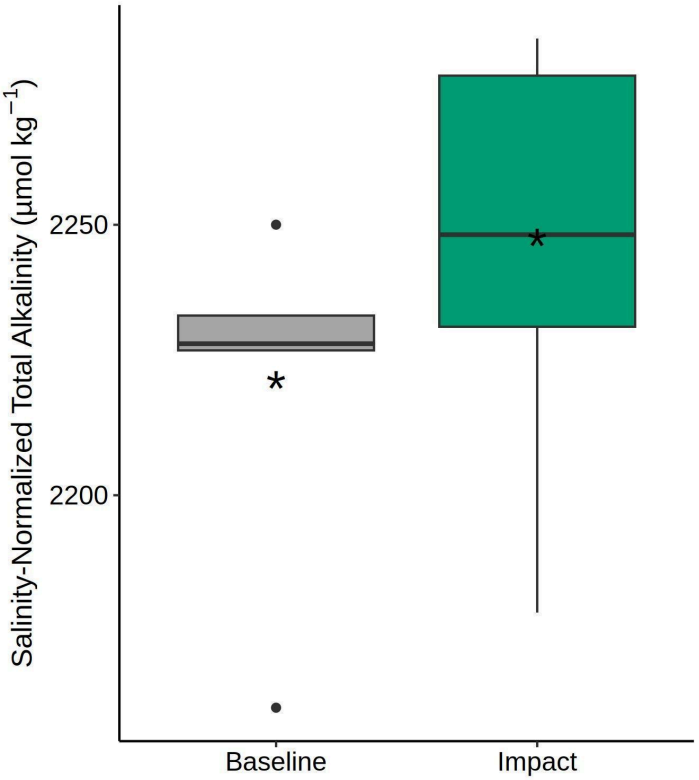
Supplementary Figure S30. Salinity measured with water quality sonde. Mean (asterisk), median (horizontal line), 25th and 75th percentile (box), minimum and maximum value (vertical line), and outliers (dots) are presented. The mean (blue, green, pink dot) derived from impact clusters for each placement day has been plotted for reference.

To account for freshwater inputs, alkalinity was normalized to a salinity of 35 psu following Friis et al. (2003). A statistically significant alkalinity-salinity relationship was derived from the annual dataset (Supplementary Figure S31). The salinity-normalized Total Alkalinity is presented in Supplementary Figures S32 and S33 for placement day Baseline vs Impact and long-term, respectively.

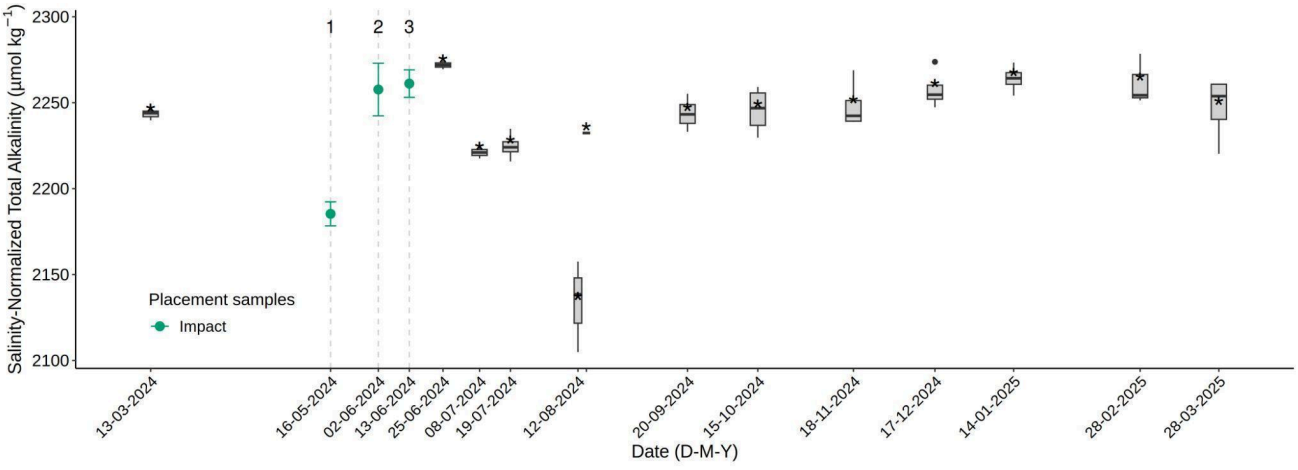


Supplementary Figure S31. Total alkalinity versus salinity for discrete samples from 13 March 2024 to 28 March 2025. Points are coloured by sampling period: pre-deployment (n=3), placement baseline

samples collected immediately before each of three placements (n=5), and post-deployment surveys (n=39). Post-placement samples were omitted due to the potential for olivine dissolution influence on alkalinity. The least-squares linear regression is plotted (TA = 29.0 × S + 1223; $R^2 = 0.78$, $p < 0.001$, n = 47).



Supplementary Figure S32. Baseline vs Impact for placement day with salinity-normalized total alkalinity. Mean (asterisk), median (horizontal line), 25th and 75th percentile (box), minimum and maximum value (vertical line), and outliers (dots) are presented.

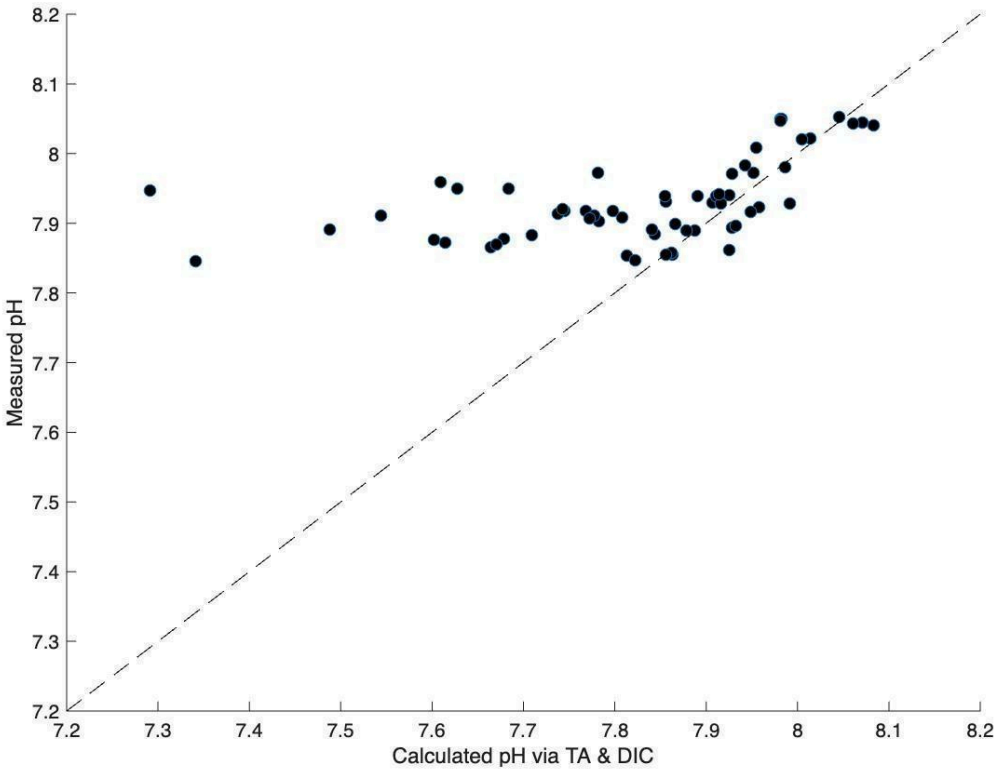


Supplementary Figure S33. Long-term salinity-normalized total alkalinity. Mean (asterisk), median (horizontal line), 25th and 75th percentile (box), minimum and maximum value (vertical line), and outliers (dots) are presented. The mean derived from impact clusters for each placement day has been plotted for reference.

1.6.4.10 Reconciliation of Discrete Sample Carbonate System

An offset was observed between measured and calculated pH, in particular in samples collected on 2 June 2024 (Placement 2) (Supplementary Figure S34), which required an in-depth analysis of sampling, analytic, and calculation methods . Many factors were evaluated to determine the cause of the offset, from correlation with all other chemical parameters, analytical methods, and potential causes of sampling artifacts (e.g., Niskin sampling error, insufficient preservation) that could lead to artificially high measured pH, low TA, high DIC, or a combination of artifacts. The data were tested against sampling technician, analytical technician, sample storage duration, etc., with no correlations present. Subsequently, the data were tested against numerous measured parameters to search for any correlation. Among the many parameters tested were trace metals (Fe, Ni, Mn), major cations (Ca, Mg, Si), nutrients (PO_4^{3-}, NH_4^+, NO_2^-+NO_3^-), water quality parameters (water temperature, ambient temperature, salinity, turbidity, dissolved oxygen), and seasonality, with no correlations present. Sonde measurements of pH over the year were around pH 8, which is consistent with the measured pH via spectrophotometric method, providing two lines of evidence that this coastal system is characterized by typical seawater pH. This follows that the calculated pH values as low as pH 7.3 must be erroneous, implying that TA or DIC, or a combination of both, are driving the erroneously low pH values. Although a definitive cause was not identified, carbonate precipitation, which would lower TA and DIC at a ratio of 2:1, is consistent with the directionality of the offset. This could have occurred within the TA or DIC sample bottles between collection and analysis if samples were not adequately filtered. The TA or DIC measurements would need to be inaccurate by up to 200 µmol/kg, orders of magnitude larger than the analytical uncertainty for each parameter. While carbonate precipitation in the sample bottles seems unlikely, it is the only process that we cannot definitely rule out, as we have ruled out other processes.

Accounting for the hypothetical change in TA and DIC needed to align the carbonate system, the conclusions are not changed in terms of the impact analysis on placement days and the long-term statistical analyses.



Supplementary Figure S34. Measured vs calculated pH of discrete water samples from March 2024 to April 2025. Dashed line represents 1:1 line.

1.6.4.11 Water Quality Guidelines

Water quality guidelines in relation to this study are presented in Supplementary Table S12.

Supplementary Table S12. Acute and chronic selected trace metals concentration in water that are not expected to pose a significant risk to the majority of species according to the US Environmental Protection Agency (US EPA) National Recommended Water Quality Criteria[25], European Union Annual Average value of Environmental Quality Standard (EU AA-EQS) and Maximum Allowable Concentration of Environmental Quality Standards for surface water (EU MAC EQS)[26], Default Guidelines Values for toxicants in marine water of Australian & New Zealand Guidelines for Fresh & Marine Water Quality that represent 99% of species protection from chronic toxicity and acute toxicity and 80% of species protection that might not protect key species from chronic and acute toxicity (DGVs ANZ)[27], and Class 1 maximum permissible values (MPV) according to CONAMA Resolution 357/2005 of Brazilian legislation. Trace metals without value are not reported as pollutants for saltwater ecosystems (US EPA), are not considered as priority substances in surface waters (EU) or DGVs (ANZ) and MPV (Brazil) are not provided.

Parameter [µg L^{-1}]	This study: Average for placement Impact clusters	This study: Average for all post-deployment surveys	US EPA Acute concs	US EPA Chronic concs	EU AA-EQS*	EU MAC-EQS**	DGVs ANZ 99% protection	DGVs ANZ 80% protection	MPV CONAMA Resolution 357/2005
Ammonium (NH_4)	0.03	0.005 ± 0.0009	-	-	-	-	500	1700	400

Nitrite (NO_2^-)	0.001	0.003 ± 0.0003	-	-	-	-	-	-	70
Cadmium (Cd)	0.05 - 0.06	0.06 ± 0.003	33	7.9	0.2	depending on water hardness between - 0.45 - 1.5	0.7	36	5
Chromium (VI) (Cr (VI))			1 100	50	-	-	0.14	85	50
Cobalt (Co)	0.02-0.07	0.02 ± 0.002	-	-	-	-	0.005	150	-
Copper (Cu)	0.52-0.58	0.39 ± 0.04	4.8	3.1	-	-	0.3	8	5
Iron (Fe)	1.7-3.4	4.64 ± 3.66	-	-	-	-	-	-	300
Nickel (Ni)	0.5-1.1	0.39 ± 0.06	74	8.2	3.1	8.2	7	560	25
Manganese (Mn)	1.2-4.1	2.32 ± 0.22	-	-	-	-	80 (the level of species protection unknown)		100
Zinc (Zn)	25.5-32.1	22.91 ± 4.02	90	81	-	-	3.3	21	90

*This parameter is the EQS expressed as an annual average value of metals concentrations measured at different times during the year that does not exceed the standard.
**This parameter is the EQS expressed as a maximum allowable concentration at any representative monitoring point.

2 CDR Model

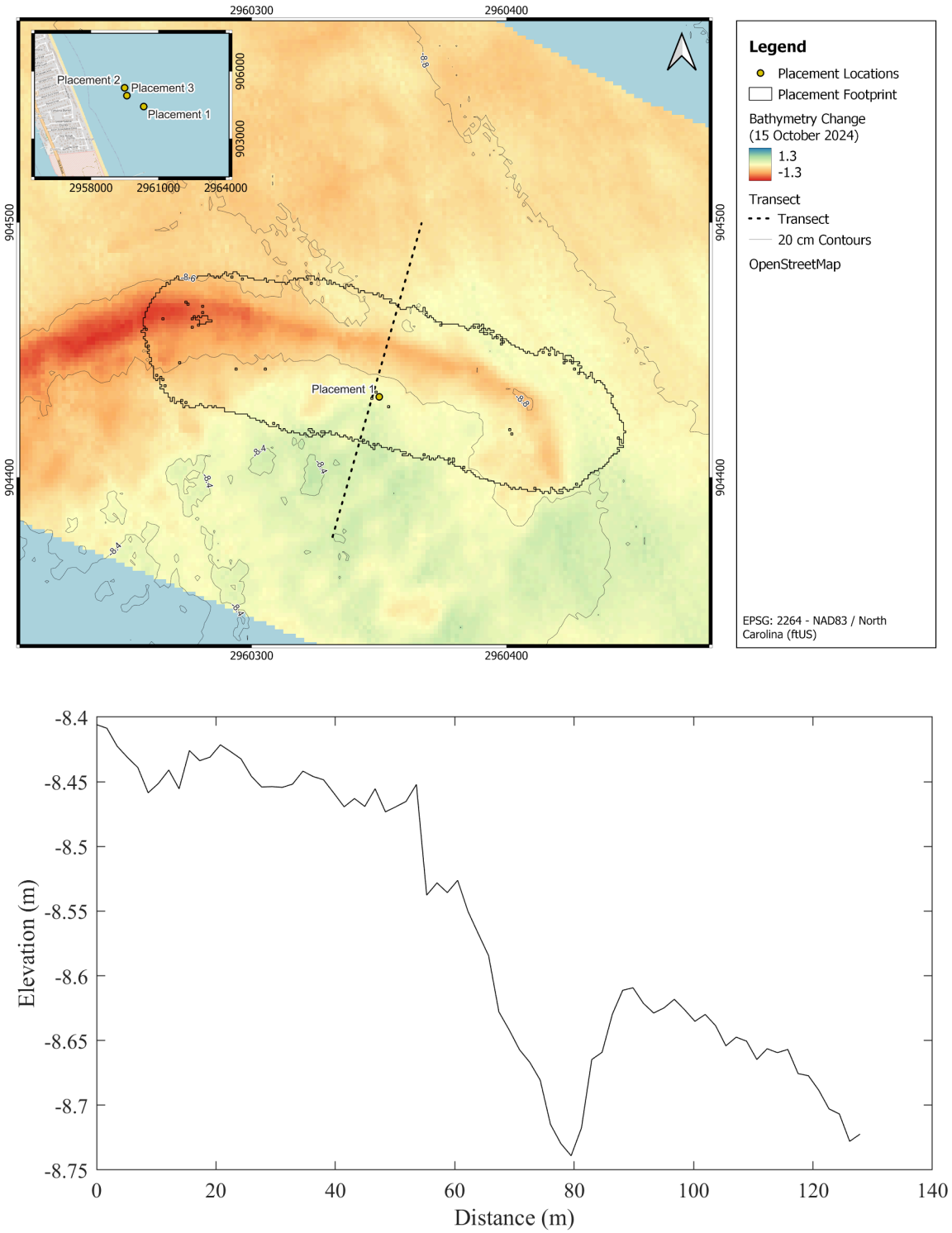
2.1 Quantification of Suspended Sediment Volume

The volume of sediment released during each placement was calculated by Vesta's coastal engineering contractor from the reduction in drone-derived stockpile volume after loading each barge. This equated to "released sediment" volumes of 1467.95 m³, 1666.73 m³ and 1781.41 m³ for Placements 1–3 (Supplementary Table S13). Following placement, sediment formed three distinct nearshore berms (main text, Figure 1), while a proportion was transported in suspension.

To estimate the proportion of material remaining on the seabed versus in suspension, pre- and post-placement bathymetric surveys were differenced to derive an initial bathymetry-derived estimate of deposited sediment volume ("deposited sediment"; Supplementary Table S13). Using this approach, 39%, 62% and 66% of the released sediment was identified as retained on the seafloor for Placements 1, 2 and 3, respectively (Supplementary Table S13). However, these deposited volumes are subject to several sources of uncertainty, including survey accuracy, compaction of the seabed beneath the berms, sediment void ratios and the potential exclusion of sediment deposited in thin layers beyond the main berm footprint. Accounting for these factors yields corrected deposited sediment volumes ("deposited sediment – corrected"; Supplementary Table S13), with the remaining fraction assumed to have been transported away from the placement site in suspension.

During Placement 1, sediment began releasing from the vessel approximately 200 m from the primary placement site. Vesta reported that 32% of the material was deposited outside of the final intended placement area. Accounting for this increases the deposited volume to 71% of the released volume for Placement 1 (Supplementary Table S13).

When sediment is released at the water surface, it generates a downward current that exerts a force on the seafloor. This process can displace underlying sediment, producing a concave profile beneath the settled material. Deposited sediment volumes derived from the pre- and post-placement bathymetry surveys assume an unchanged pre-placement seabed, meaning that feedstock within any depression would not be accounted for. Evidence for this depression is observed at Placement 1, where the berm migrated onshore and had dispersed by 15 October 2024, leaving a concave profile of approximately 10 cm at the original footprint location (Supplementary Figure S35). This feature likely reflects a combination of localized scour and/or compaction of the seabed caused by the impact of sediment falling through the water column. Applying a correction equivalent to a 10 cm layer across each placement footprint increases the deposited volumes to 78%, 72% and 76% of the released volume for Placement 1, 2 and 3 (Supplementary Table S13).



Supplementary Figure S35. Bathymetric survey over Placement 1 showing a concave seafloor profile at the placement site on the order of ~10 cm. Placement occurred on 16 May 2024, and the survey was conducted on 15 October 2024. The top plot shows the bathymetry map, while the lower plot shows the elevation profile along the transect indicated on the map.

The bathymetry surveys have a vertical accuracy of ±10 cm, which was used as a threshold to define the areal extent of each placement and isolate the berms for volume calculations. This uncertainty implies that the deposited volumes could include an additional vertical component of up to 10 cm beneath each mapped footprint. Applying this as a conservative correction increases the deposited volumes to 78% ± 9%, 72% ± 14% and 76% ± 13% of sediment released for Placements 1, 2 and 3.

Pre- and post-placement volumes are influenced by void ratios, which also affect the conversion of volume to mass. Computing sediment mass from volumetric data requires known or estimated void ratios. Typical values for sand range between 0.4 to 0.8 for compact and loosely packed material, depending on factors such as grain size, sorting, and angularity. Pre- and post-placement processes (e.g. handling, aeration, fluidization) could have either increased or decreased the void ratios. In the absence of direct measurements, a representative porosity of 40% was assumed, consistent with commonly used values for unconsolidated marine sediments in USACE guidance (USACE, 2002), corresponding to a nominal bulk density of 1.96 g cm^{-3}.

Converting the corrected deposited sediment volumes to masses yield values of 2244.53 ± 196.20 tonnes for Placement 1, 2361.46 ± 326.87 tonnes for Placement 2, and 2660.47 ± 347.27 tonnes for Placement 3 (Supplementary Table S13).

Supplementary Table S13. Metrics for each placement, derived from sediment prior to release and from bathymetric surveys.

		Placement 1	**Placement 2**	**Placement 3**	**Total**
Berm Characteristics	**Distance Offshore (m)**	832	683	670	-
	Depth (m)	-8.55	-7.65	-7.58	-
	Length (m)	60	62	80	-
	Width (m)	20	34	40	-
	Height (m)	2.2	2.09	2.37	-
	Footprint (m^2)	1000	1666	1770	4436
Released Sediment	**Volume (m^3)**	1467.95	1666.73	1781.41	4916.09
	Mass (tonnes)	2880.11	3270.12	3495.13	9645.36
Deposited Sediment	**Volume (m^3)**	579	1037	1179	2795
	Mass (tonnes)	1136.00	2034.59	2313.20	5483.79
	% of Volume Released	39%	62%	66%	57%
Deposited Sediment - Corrected	**Volume (m^3)**	1144 ± 100	1203.60 ± 166.60	1356 ± 177	3703.60 ± 443.60
	Mass (tonnes)	2244.53 ± 196.20	2361.46 ± 326.87	2660.47 ± 347.27	7266.46 ± 870.34
	% of Volume Released	78 ± 9	72 ± 14	76 ± 13	75 ± 12
Suspended Sediment	**Volume (m^3)**	323.95	463.13	425.41	1212.49
	Mass (tonnes)	635.59	908.66	834.65	2378.91
	% of Volume Released	22%	28%	24%	25%

2.2 CDR Model Setup and Validation

To mechanistically quantify the magnitude and timescale of carbon dioxide removal from the fraction of suspended feedstock released during the trial, a numerical modeling framework was developed. The model comprises two primary components: (1) a sediment transport module that determines the grain size distribution, mass, and mineralogy of material suspended in the water column and (2) a geochemical module that simulates mineral dissolution, associated alkalinity and trace metal generation, and estimates carbon removal. The two modules are offline coupled, such that outputs from the sediment transport module provide boundary conditions for the geochemical module.

2.2.1 Sediment Motion Threshold Module

The total sediment load can be partitioned into bedload and suspended load, which is parameterised here according to the Rouse number, Shields Parameter and Transport Model Parameter. Particles with sufficiently low settling velocities relative to the near-bed shear velocity are predominantly transported in suspension, whereas coarser particles with higher settling velocities are transported as bedload. The suspended fractions may undergo cycles of settling and resuspension under variable hydrodynamic conditions. A further washload fraction is defined, following Rouse (1937), as the finest fraction that is not in exchange with the seabed due to their very low settling velocities relative to turbulent mixing, and are therefore effectively maintained in suspension. This fraction is therefore assumed to have the highest potential for complete dissolution within the water column. Near-bed shear velocity varies with hydrodynamic conditions and water depth, leading to different grain size thresholds for bedload, suspended load and wash load. As these conditions vary in space and time, a fixed shear velocity is a simplification; however, a spatially and temporally varying shear velocity could not be robustly constrained over the dissolution timescales considered here.

The following describes the process-based model used to determine sediment grain mobility and suspension thresholds.

2.2.1.1 Motion Threshold Model Equations

The settling velocity of individual grains (w_s) was calculated using the formulation of Ferguson and Church (2004):

$$w_s = \frac{RgD^2}{C_1 v + \left(0.75 C_2 RgD^3\right)^{0.5}} \quad (1)$$

where R its submerged specific gravity, g the acceleration due to gravity, D is the particle diameter, v the kinematic viscosity of the fluid, C_1 and C_2 empirical constants representing viscous and turbulent drag regimes. Submerged specific gravity is given by:

$$R = \frac{\rho_s - \rho}{\rho} \quad (2)$$

where ρ_s is grain density and ρ is fluid density. Total bed shear stress (τ_0) is composed of both skin-friction (τ_{0s}) and form-drag (τ_{0f}). The total mean (τ_m) and maximum (τ_{max}) bed shear stresses were estimated following the combined wave-current formulations of Soulsby (1997):

$$\tau_m = \tau_c\left[1 + 1.2\left(\frac{\tau_w}{\tau_c+\tau_w}\right)^{3.2}\right] \quad (3)$$

$$\tau_{max} = \left[(\tau_m + \tau_w cos\phi)^2 + (\tau_w sin\phi)^2\right]^{1/2} \quad (4)$$

where τ_c and τ_w are the bed shear stresses derived from the individual wave and current components respectively. This formulation accounts for the enhancement of bed shear stress under these combined parameters beyond their individual contributions due to the non-linear interaction of these forces at the boundary layer (Soulsby, 1997). Total shear stress is related to shear velocity (u_*) through the form:

$$u_* = \left(\frac{\tau_0}{\rho}\right)^{1/2} \quad (5)$$

which was used to compute the Rouse number (Rouse, 1937), by:

$$P = \frac{w_s}{ku_*} \quad (6)$$

where k is the von Kármán constant (k=0.4). This number is used to determine how sediment is transported in a fluid and used to generate the Transport Mode Parameter (f_{sk}) of Greimann et al., (2008) to quantify the fractionation of suspended sediment (r_{sk}) and bedload transport, given by:

$$r_{sk} \approx f_{sk} = min[1, 2.5exp(-P)] \quad (7)$$

Grain entrainment from the bed is governed by skin-friction only, since form-drag generated by ripples does not act directly on a grain. Accordingly, the Shields parameter (θ) is derived from the skin-friction component of bed shear stress and represents the ratio of fluid forces acting on a grain to its submerged weight resisting motion and is given by:

$$\theta = \frac{\tau_{0s}}{g(\rho_s-\rho)D} \quad (8)$$

Grain entrainment occurs when the Shields parameter exceeds the critical Shield's number ($\theta > \theta_{cr}$) as shown in Supplementary Figure S36, which is calculated following the formulation of Soulsby and Whitehouse (1997):

$$\theta_{cr} = \frac{0.30}{1+1.2D_*} + 0.055\left[1 - exp(-0.020D_*\right]$$
(9)

where D_* is the dimensionless grain diameter given by:

$$D_* = \left[\frac{g(s-1)}{v^2}\right]^{1/3} D$$
(10)

where s is the submerged specific density of a grain given by:

$$s = \frac{\rho_s}{\rho}$$
(11)

2.2.1.2 Motion Threshold Parameterization

The values that were used to parameterise the default version of the model are given in Supplementary Table S14. Where values have been changed for model testing or scenarios, this has been specified in the subsequent sections.

Supplementary Table S14. Sediment motion threshold module parameterization

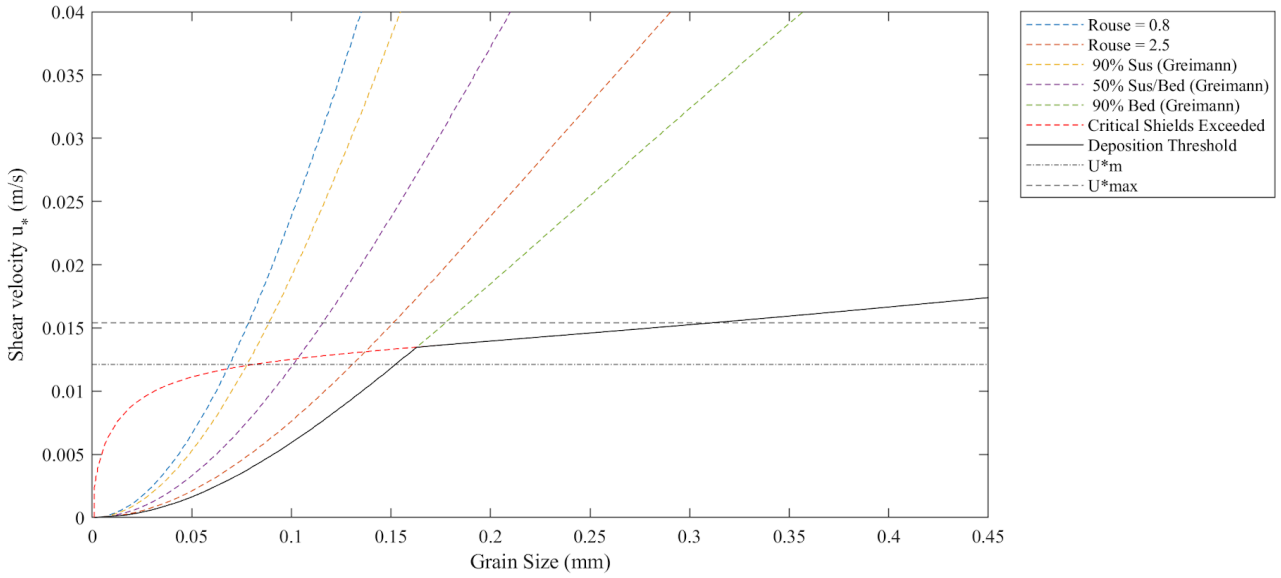
Symbol	Description	Value / Source	Units
w_s	Grain settling velocity	$\frac{RgD^2}{C_1 v+\left(0.75C_2 RgD^3\right)^{0.5}}$	m s^{-1}
R	Submerged specific gravity of a grain	$\frac{\rho_s - \rho}{\rho}$	-
g	Acceleration due to gravity	9.81	m s^{-2}
D	Particle diameter	Measured / specified from laser diffraction dataset	m
v	Kinematic viscosity of the fluid	1.0×10^{-6}	m^2 s^{-1}
C_1	Empirical constant (viscous drag regime)	24	-
C_2	Empirical constant (turbulent drag regime)	1.2	-

ρ_s	Grain density	3300	kg m^{-3}
ρ	Fluid density	1025	kg m^{-3}
τ_m	Total mean bed shear stress	0.1497	Pa
τ_{max}	Total maximum bed shear stress	0.2433	Pa
u_*_m	Mean shear velocity	$\left(\frac{\tau_m}{\rho}\right)^{1/2}$	m s^{-1}
u_*_max	Maximum shear velocity	$\left(\frac{\tau_{max}}{\rho}\right)^{1/2}$	m s^{-1}
P	Rouse number	$\frac{w_s}{ku_*}$	-
k	von Karman constant	0.4	-
f_{sk}	Transport mode parameter	$min[1, 2.5exp(-P)]$	-
r_{sk}	Fractionation of suspended sediment	f_{sk}	-
θ	Shields parameter	$\frac{\tau_{0s}}{g(\rho_s-\rho)D}$	-
θ_{cr}	Critical Shields parameter	$\frac{0.30}{1+1.2D_*} + 0.055\left[1 - exp(-0.020D_*\right]$	-
D_*	Dimensionless grain diameter	$\left[\frac{g(R-1)}{v^2}\right]^{1/3} D$	-

2.2.1.3 Motion Threshold Model Testing

Two sediment thresholds were required for the CDR scenarios defined herein; a mode-based grain size threshold dividing suspended transport from bedload, and a threshold for washload. The Transport Mode Parameter (Equation 7) was used to determine a threshold grain size for suspended transport, where the fraction of material in suspension under given shear velocities was equal to a user-defined value that represents a dominant suspension regime; herein defined as 50% suspended load meaning that all grains smaller than this threshold are dominantly in the suspension regime (Supplementary Figure S36). The washload threshold is defined by the Rouse number, with a typical value of 0.8. The max shear velocity is used to determine motion, and the mean shear velocity is used to determine the transport mode of a given grain size.

The D_{50} of all three TSS samples align with the dominant suspended transport regime predicted by the model (74 µm, 41 µm, 0.39 µm). The D_{50} of the seafloor sediment sample (200 µm) fell within the bedload and 'in-motion' regime. While this sample clearly represents bedload material, it is not possible to ascertain that it was 'in-motion', as predicted by the model. However, this is likely the case given it was collected from the upper 1-3 cm of the sediment surface. These observations demonstrate the model's ability to predict the dominant transport mode of different grain sizes according to the shear velocity.



Supplementary Figure S36. Thresholds for grain motion according to the grain size and shear velocity. Rouse numbers and the Transport mode parameter (Greimann et al., 2008) are calculated to determine the mode of transport.

2.2.1.4 Mass and Mineralogy of Sediment in Motion

The mass of released feedstock and the grain size distribution of the bulk feedstock was used to determine the total mass of feedstock in each grain size bin. For each run of the suspended sediment CDR model, the mass and grain size distribution of sediment was subsequently determined by the grain size threshold which was determined by the sediment motion module. Feedstock mineralogy was analyzed by XRD on selected grain size bins and revealed that the forsterite component of the 0-45 µm fraction (56.1 wt% forsterite) was substantially lower than the bulk feedstock (88.6 wt% forsterite); the bulk feedstock was also indistinguishable from the other measured grain size fractions (46-63 µm, 63-150 µm, and 150-250 µm). As such, the mass of suspended feedstock was converted to mass of suspended olivine for the geochemical module, evaluated in 1 µm grain size increments, based on the proportion of olivine in each grain size bin

(i.e., 56.1 wt% for grains 45 μm or less, or otherwise 88.6 wt%). While XRD results from TSS samples collected during placements should be taken as qualitative, they are broadly consistent with the finding that finer grain size distributions have lower forsterite content than the bulk feedstock, while coarser grain size distributions have higher forsterite content than the bulk feedstock.

2.2.2 Geochemical Module

The olivine dissolution equation used herein is from Rimstidt et al. (2012):

$$Rate = 10^{(4.07 - (0.256 * pH) - (3465 / (temp + 273.15)))} \quad (12)$$

Where *rate* is the dissolution rate of forsterite (mol forsterite dissolved / m^2 forsterite geometric surface area / s), *pH* is on the total scale, and *temp is in °C.*

A shrinking core model was incorporated through the following:

$$Forsterite_{remaining} = (4 * \pi / (3 * V_{molar})) * (r_0 - (rate * V_{molar} * time))^3 \quad (13)$$

Where $forsterite_{remaining}$ is in (mol), V_{molar} is the molar volume of forsterite (m^3 mol^{-1}), *rate* is the dissolution rate (mol forsterite dissolved / m^2 forsterite surface area / s), and *time* is in (s).

Olivine dissolution was evaluated through the following:

$$Forsterite_{dissolved} = forsterite_{initial} - forsterite_{remaining} \quad (14)$$

Where all terms are in (mol).

The forsterite grain radii are updated after every time step to account for continuous dissolution. Resolution of time steps is dependent on application of the model to optimize computational efficiency.

2.2.2.1 Set Up: Model Evaluation and In-situ Olivine Dissolution Rates

The geochemical module was evaluated by comparing measured Ni and Co concentrations with modeled Ni and Co concentrations based on predicted olivine dissolution rates. As this is a short-term application of the geochemical module, olivine dissolution was evaluated every minute. Modeled metal concentrations were calculated through the following:

$$[X]_{model} = forsterite_{dissolved} * X_{feedstock} / reservoir \quad (15)$$

Where $[X]_{model}$ is in (mol kg^{-1}), $forsterite_{dissolved}$ is in (mol), $X_{feedstock}$ is the metal (Ni or Co) wt% as a fraction of the feedstock (Ni = 2810 ppm; Co = 119 ppm), and *reservoir* is the mass of the water column above the placement footprint in (kg).

Measured metal concentrations was calculated through the following:

$$[X]_{measured} = [X]_{sample} - [X]_{background} \quad (16)$$

Where $[X]_{sample}$ is the metal concentration of the sample being modeled and $[X]_{background}$ is the average of two pre-placement samples. All terms are in (mol kg^{-1}).

2.2.2.2 Set Up: Sensitivity Analysis and CDR Potential

The geochemical module was used to evaluate the sensitivity of varying parameters to olivine dissolution and CDR potential. As this is a long-term application of the geochemical module,

olivine dissolution was evaluated every day. Olivine dissolution is converted to carbon dioxide removed through the following:

$$CDR = forsterite_{dissolved} * TA_{production} * efficiency * CO_{2\ molar\ mass} \quad (17)$$

Where *CDR* is in (g), $TA_{production}$ is the stoichiometric factor of Total Alkalinity production from olivine dissolution (4 mol TA: 1 mol olivine), *efficiency* is the air-sea gas exchange efficiency factor of 70.5%, the annual long-term efficiency near the site location (Zhou et al., 2025)., and $CO_{2\ molar\ mass}$ is the molar mass of CO_2: 44.01 g mol^{-1}.

2.3 Model Evaluation and In-Situ Olivine Dissolution Rates

The model was used to predict changes to water column chemistry (Ni, Co, alkalinity) that would result from olivine dissolution during placements such that they could be compared to measured water column values. We focus on two trace metals present in olivine which we observed in higher concentrations than background during the placements: Ni and Co (Figure 4). Due to very low background concentrations, Ni and Co may serve as tracers for olivine dissolution. We validate the model using four discrete seawater samples, collected in the medium- to high- impact clusters (Clusters 4 and 5), from Placements 2 and 3 (2 samples from each placement). Samples from medium and high impact clusters were selected to ensure they represent the plume of released feedstock. Samples from Placement 1 were not used because no samples were collected in medium or high impact clusters.

The observed increase in water column trace metal concentrations could have resulted from both olivine dissolution in the water column prior to sample collection (termed “in-situ dissolution”), as well as additional dissolution within the Niskin bottle during the delay between sample collection and filtration (termed “ex-situ dissolution”). As such, the geochemical module was configured to simulate both of these components, the sum of which provided the total modeled trace metal signal expected from olivine dissolution. The model setup leverages the shrinking core model (Equation 13) to quantify dissolution of a given mass of material with a defined grain size distribution in a user-defined volume of seawater.

The in-situ dissolution period spans the time between feedstock placement and Niskin bottle collection. Simulations were conducted for samples collected 20-35 minutes post-placement, during which the entire olivine mass and grain size distribution from each placement were allowed to dissolve over the elapsed time. The volume of seawater considered was defined by the seafloor footprint of the settled material and the average overlying water column depth above the berm (Supplementary Table S13). While simplistic, we considered this a closed system for the purpose of this in-situ application as this results in the most conservative estimate for dissolution. Because the material was released from the sea surface, this component of the model represents the initial descent through the water column as well as partial settling to the seafloor. Allowing the full mass of olivine and grain size distribution to dissolve likely overestimates water column dissolution, but provides a useful upper bound on modeled trace metal concentrations.

The ex-situ dissolution period represents the interval between Niskin bottle collection and subsequent sample filtration, approximately three hours later, during which continued dissolution of suspended material contained in the Niskin bottle may have occurred. In this phase, the dissolving mass was constrained using total suspended solids (TSS) measurements collected shortly before the Niskin samples, and the associated grain size distribution was derived from the

same TSS filters. This resulted in a finer-grained sediment fraction relative to the in-situ period (i.e., only suspended material).

For four samples between Placements 2 and 3, the modeled Ni concentrations were 3-7 times lower, and modeled Co concentrations 4-9 times lower than observed in the field (Supplementary Table S15). The modeled concentrations are almost entirely driven by in-situ dissolution in the water column prior to sample collection, whereas ex situ dissolution within the Niskin bottle post-collection was negligible (<0.05 nmol kg^{-1} Ni, <0.002 nmol kg^{-1} Co). This difference in parameterization between the in situ and ex situ modeled dissolution is physically justified by the setup of each stage. The in-situ approach accounts for the entire placement material as it falls through the water column during settling, whereas the ex-situ approach is constrained solely to the suspended fraction trapped within the Niskin bottle between collection and filtration. Although the in situ dissolution approach used the entire mass of placed olivine, rather than partitioning between suspended and bedload fractions, this simplification inherently leads to an overestimation of the suspended sediment concentration in the water column, yet the model nevertheless underpredicted trace metal concentrations observed in the field. Lastly, these modeled dissolution rates predict alkalinity generation up to 8 μmol kg^{-1}. While this concentration is higher than our analytical uncertainty, it is significantly lower than the natural variability observed on the placement days, hence modeled signals do not predict a measurable increase in alkalinity.

Supplementary Table S15. Geochemical module validation results comparing measured and modeled trace metal concentrations.

Sample	Measured concentrations (nmol kg^{-1})	Modeled concentrations (nmol kg^{-1})
Placement 2 28 min post-placement	Ni: 27.9 Co: 1.53	Ni: 4.04 Co: 0.171
Placement 2 35 min post-placement	Ni: 14.5 Co: 0.858	Ni: 5.04 Co: 0.213
Placement 3 20 min post-placement	Ni: 20.7 Co: 1.17	Ni: 3.73 Co: 0.158
Placement 3 28 min post-placement	Ni: 18.0 Co: 1.02	Ni: 5.25 Co: 0.222

2.4 Sensitivity Analysis and CDR Potential Model Runs

The model was run to evaluate the sensitivity of carbon dioxide removal (CDR) potential to key environmental and physical parameters relevant to this field trial, and other field trials using solid feedstock. A suite of scenarios was constructed (main text), with a default case assuming that the entire suspended olivine load remains in the nearshore surface ocean and dissolves completely under conditions representative of the project site. These conditions include coastal seawater temperature and pH, with future changes

prescribed following the IPCC SSP5–8.5 scenario, corresponding to a +3.7 °C increase in sea surface temperature and a −0.44 unit decrease in pH by 2100 (Fox-Kemper et al., 2021). The model applies a representative, site-specific shear velocity derived from wave conditions at Duck, NC during Placement 3. While shear velocity varies with factors such as local hydrodynamic conditions and water depth, this fixed value is used for the default scenario with no offshore transport or particle subduction included. This effectively assumes that suspended material remains within the surface coastal environment over the full simulation period. The influence of shear velocity on model outcomes is explored, using the 10th and 90th percentile values at the field site recorded throughout 2024 to represent plausible upper and lower bounds; this does not attempt to capture changes associated with transport to different locations, but rather to broadly assess the sensitivity of CDR potential to variations in shear velocity.

The model is implemented with the literature-based dissolution rate formulation of Rimstidt et al. (2012), which we consider a reasonable and conservative representation of dissolution over decadal timescales given the current data available for these longer timescales. This choice is supported by laboratory studies (e.g., Fuhr et al., 2022) showing that elevated initial dissolution rates can exceed middle to end of experiment rates by up to an order of magnitude, suggesting that short-term discrepancies may not persist over longer durations. Model outputs track the cumulative mass of olivine dissolved, which is converted to alkalinity production using a 4:1 alkalinity-to-olivine stoichiometric relationship. To estimate potential CDR, alkalinity production is further scaled by an air-sea gas exchange efficiency factor of 70.5%, the annual long-term efficiency near the site location (Zhou et al., 2025).

To assess the influence of future climate uncertainties, the uncertainty projections from the SSP5-8.5 multi-model ensemble were propagated through the dissolution model, allowing evaluation of how variability in temperature and pH trajectories impacts CDR outcomes. Simulations were run continuously for 200 years. Our analysis focused on two key time horizons: 20 years, corresponding to typical carbon crediting periods (Michaelowa et al., 2019), and the full dissolution timeline.

2.4.1 Scenario 1

Scenario 1 represents the default scenario used for the CDR modeling. Starting temperature and pH represent the annual mean values from 2020-2025 (omitting 2024 due to temperature sensor malfunctions during half the year) in Duck, NC: 15.8 °C, 8.04 pH units. Temperature increases and pH decreases at SSP5-8.5 "business as usual" rates: 0.049 °C y^{-1}, -0.0059 pH units y^{-1} (Fox-Kemper et al., 2021). The settling velocity was calculated according to the method of Ferguson and Church (2004; Equation 1), in quiescent conditions with a constant water depth. Placement 3 hydrodynamics conditions were used to compute bed shear stress, with a significant wave height of 0.59 m, mean wave direction of 120°, peak wave period of 5.6 s, current speed of 0.21 m s^{-1} and mean current direction of 329°. These conditions are similar to the mean hydrodynamics conditions from the period of April 2024 to April 2025 (main text). Bed shear stress was used to calculate mean shear velocity (0.014 m s^{-1}) and the maximum shear velocity (0.018 m s^{-1}). Using the model described here, the grain size threshold for suspension-dominated transport was calculated at 111 μm. Additional analyses regarding climate projection (SSP5-8.5)

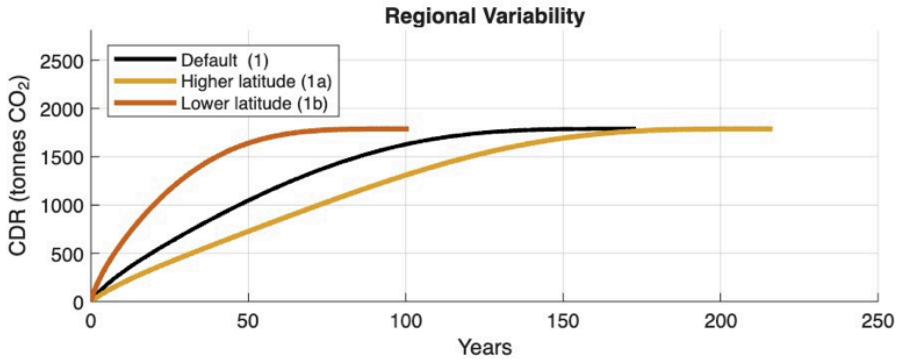
uncertainty resulted in only a <0.8% difference in CDR within 20 years, thus implying that this uncertainty does not meaningfully impact CDR potential on these timescales.

Scenario 1a represents the scenario in which a deployment is conducted in a cooler region. Starting temperatures were chosen as an annual mean representative of the US Northeast coastline (e.g., Maine): 9.8 °C, 8.04 pH units. Temperature was increased and pH was decreased at faster rates according to the region (Bopp et al., 2013): 0.053 °C y^{-1}, -0.0067 pH units y^{-1}.

Scenario 1b represents the scenario in which a deployment is conducted in a warmer region. Starting temperatures were chosen as an annual mean representative of the US Southeast coastline (e.g., Florida): 26.6 °C, 8.04 pH units. Temperature was increased and pH was decreased at slower rates according to the region (Bopp et al., 2013): 0.033 °C y^{-1}, -0.0053 pH units y^{-1}.

Scenarios 1a and 1b did not update other model parameters that can also vary by region, such as air-sea gas exchange efficiency which is impacted by seawater temperature, local hydrodynamics, etc. (Zhou et al., 2025).

One key conclusion that emerged from the sensitivity analysis is that future rates of ocean warming and acidification are much less impactful to CDR rates and total dissolution times than the initial geochemical conditions of the deployment site. This is best illustrated by the latitudinal scenarios (Scenarios 1a and 1b): despite higher latitudes experiencing faster rates of future warming and acidification than lower latitudes (Bopp et al., 2013), a warmer low latitude deployment yielded 194% more CDR in the first 20 years, and a 53% reduction in total dissolution time, as compared to deployment in a cooler high latitude (Supplementary Figure S37). Because the majority of dissolution occurs within the first few decades, the model is relatively insensitive to the varying slopes of IPCC SSP5-8.5 projections and future warming and acidification rates. This suggests that the immediate geochemical environment at the deployment site is more relevant to climate mitigation timescales than the eventual conditions of water masses into which the material may migrate.



Supplementary Figure S37. Latitudinal scenarios exploring temperature and pH, including initial conditions and rates of change.

2.4.2 Scenario 2

Scenario 2 represents how water mass sinking and subduction into the deep ocean affects CDR potential. The suspended sediment was modeled to become entrained in the Gulf Stream off Duck, NC and transited to the North Atlantic using current speed and volume representative of Gulf Stream transport (Heiderich and Todd, 2020). The model assumes that during transit the surface water gradually sinks (> 100 m) and is ultimately subducted into the deep ocean. As such, alkalinity generation that results in air-sea gas exchange and CDR is turned off in the model when

the water mass reaches the North Atlantic. The default temperature, pH, and their rates of change, as per Scenario 1 were used. The grain size thresholds were computed using Placement 3 hydrodynamic conditions, as per Scenario 1, with the suspension-dominated threshold calculated at 111 μm.

2.4.3 Scenario 3

Scenario 3 represents conditions where the washload fraction remains suspended in the water column, and the grains fully dissolve. The default temperature, pH, and their rates of change, as per Scenario 1 were used. The grain size thresholds were computed using Placement 3 hydrodynamic conditions, as per Scenario 1, with the suspension-dominated threshold calculated at 111 μm and the washload threshold at 76 μm. The remaining setup aligns with the default conditions of Scenario 1.

2.4.4 Scenario 4

Scenario 4 demonstrates how spatial and temporal variability in shear velocity affects grain suspension and carbon removal potential. The default temperature, pH, and their rates of change, as per Scenario 1 were used.

Scenario 4a specifically explores a decrease in shear velocity from the default setup on Scenario 1. Hydrodynamics conditions throughout 2024 were used to compute the shear velocity derived from each record at the study site. The 10th percentile mean shear velocity (0.0024 m s^{-1}) and the maximum shear velocity (0.0031 m s^{-1}). Using the model described here, the grain size threshold for suspension-dominated transport was calculated at 42 μm.

Scenario 4b specifically explores an increase in shear velocity from the default setup on Scenario 1. Hydrodynamics conditions throughout 2024 were used to compute the shear velocity derived from each record at the study site. The 90th percentile mean shear velocity (0.0207 m s^{-1}) and the maximum shear velocity (0.0268 m s^{-1}). Using the model described here, the grain size threshold for suspension-dominated transport was calculated at 138 μm.

3 References

Antón, A., Cebrian, J., Heck, K.L., Duarte, C.M., Sheehan, K.L., Miller, M.-E.C., et al. (2011). Decoupled effects (positive to negative) of nutrient enrichment on ecosystem services. *Ecol. Appl.* 21, 991–1009. doi: 10.1890/09-0841.1

ANZG (2018). *Toxicant Default Guideline Values for Aquatic Ecosystem Protection. Australian and New Zealand Guidelines for Fresh and Marine Water Quality*. Canberra: Australian and New Zealand Governments and Australian state and territory governments.

Bertagni, M.B., and Porporato, A. (2022). The carbon-capture efficiency of natural water alkalinization: implications for enhanced weathering. *Sci. Total Environ.* 838:156524. doi: 10.1016/j.scitotenv.2022.156524

Bopp, L., Resplandy, L., Orr, J.C., Doney, S.C., Dunne, J.P., Gehlen, M., et al. (2013). Multiple stressors of ocean ecosystems in the 21st century: projections with CMIP5 models. *Biogeosciences* 10, 6225–6245.

CoastWatch (2025). Chesapeake and Delaware Bays satellite data. Available at: https://eastcoast.coastwatch.noaa.gov/region_cd.php#dmv (Accessed November 18, 2025).

Cox, K., McKeown, N., Vanden Broeck, A., Van Breusegem, A., Cammaerts, R., and Thomaes, A. (2020). Genetic structure of recently fragmented suburban populations of European stag beetle. *Ecol. Evol.* 10, 12290–12306. doi: 10.1002/ece3.6858

European Commission (2013). Directive 2013/39/EU of the European Parliament and of the Council of 12 August 2013 amending Directives 2000/60/EC and 2008/105/EC as regards priority substances in the field of water policy. *Official Journal of the European Union* L226, 1–17.

Ferguson, R.I., and Church, M. (2004). A simple universal equation for grain settling velocity. *J. Sediment. Res.* 74, 933–937.

Fox-Kemper, B., Hewitt, H.T., Xiao, C., Aðalgeirsdóttir, G., Drijfhout, S.S., Edwards, T.L., et al. (2021). "Ocean, cryosphere and sea level change," in *Climate Change 2021: The Physical Science Basis. Contribution of Working Group I to the Sixth Assessment Report of the Intergovernmental Panel on Climate Change*, eds. V. Masson-Delmotte, P. Zhai, A. Pirani, S.L. Connors, C. Péan, et al. (Cambridge, United Kingdom and New York, NY, USA: Cambridge University Press), 1211–1362. doi: 10.1017/9781009157896.011

Friis, K., Kortzinger, A., and Wallace, D. W. R. (2003). The salinity normalization of marine inorganic carbon chemistry data. *Geophys. Res. Lett.* 30:2.

Fuhr, M., Geilert, S., Schmidt, M., Liebetrau, V., Vogt, C., Ledwig, B., et al. (2022). Kinetics of olivine weathering in seawater: an experimental study. *Front. Clim.* 4:831587.

Gilson Co. (2024). An expert guide to selecting a sample splitter. Available at: https://www.globalgilson.com/blog/an-expert-guide-to-selecting-a-sample-splitter

Goldstein, E.B., Stasiewicz, J., Mieras, R., and Mohanty, S. (2022). Instagrain: a camera for instant sediment grain size measurements. Zenodo. doi: 10.5281/zenodo.7041151

Greimann, B., Lai, Y., and Huang, J. (2008). Two-dimensional total sediment load model equations. *J. Hydraul. Eng.* 134, 1142–1146.

Heiderich, J., and Todd, R.E. (2020). Along-stream evolution of Gulf Stream volume transport. *J. Phys. Oceanogr.* 50, 2251–2270. doi: 10.1175/JPO-D-19-0303.1

Michaelowa, A., Shishlov, I., Hoch, S., Bofill, P., and Espelage, A. (2019). *Overview and Comparison of Existing Carbon Crediting Schemes*. Helsinki: Nordic Environment Finance Corporation (NEFCO).

Monterey, G., and Levitus, S. (1997). *Seasonal Variability of Mixed Layer Depth for the World Ocean*. NOAA Atlas NESDIS 14. Washington, DC: U.S. Government Printing Office.

Rimstidt, J.D., Brantley, S.L., and Olsen, A.A. (2012). Systematic review of forsterite dissolution rate data. *Geochim. Cosmochim. Acta* 99, 159–178.

Rouse, H. (1937). Modern conceptions of the mechanics of fluid turbulence. *Trans. Am. Soc. Civ. Eng.* 102, 463–541.

Soulsby, R.L. (1997). *Dynamics of Marine Sands*. London: Thomas Telford.

Soulsby, R.L., and Whitehouse, R.J. (1997). "Threshold of sediment motion in coastal environments," in *Pacific Coasts and Ports '97: Proceedings of the 13th Australasian Coastal and Ocean Engineering Conference and the 6th Australasian Port and Harbour Conference*, Vol. 1 (pp. 145–150). Christchurch, NZ: Centre for Advanced Engineering, University of Canterbury.

U.S. Army Corps of Engineers (USACE) (2002). *Coastal Engineering Manual*. Engineer Manual 1110-2-1100, Part III, Chapter 1: Coastal sediment properties. Washington, DC: U.S. Army Corps of Engineers.

U.S. Environmental Protection Agency (USEPA) (2024). *National Recommended Water Quality Criteria*. Available at: https://www.epa.gov/wqc/national-recommended-water-quality-criteria-tables

Zhou, M., Tyka, M.D., Ho, D.T., Yankovsky, E., Bachman, S., Nicholas, T., et al. (2025). Mapping the global variation in the efficiency of ocean alkalinity enhancement for carbon dioxide removal. *Nat. Clim. Chang.* 15, 59–65.